Table of Contents

List of Figures

xvi

List of Tables

Nomenclature

Symbol	Description	Units (SI)
A_j	Frequency factor for reaction j	m^3/s
A_p	Particle surface area	cm^2 or m^2
a	Width of waveguide	m
B	Magnetic field	T
b	Height of waveguide	m
C	Concentration	mol/m^3
c_0	Speed of light in a vacuum	m/s
c_k	Molar concentration of species k	mol/m^3
$C_{p,i}$	Heat capacity of species k	$J/(kg \cdot K)$
D_{AB}	Binary diffusion coefficient	m^2/s
D_c	Column diameter	m or cm

$\mathbf{D}_e$	Electron diffusivity	m^2/s
D_i	Inlet diameter	m or cm
$\mathbf{D}_\varepsilon$	Electron energy diffusivity	m^2/s
D_k^T	Thermal diffusion coefficient	$kg/(m \cdot s)$
d_p	Particle diameter	m or mm
$\mathbf{E}$	Electric field	V/m
$\overline{E}$	Average electron energy	eV
E_{ave}	Average kinetic energy	eV
E_j	Activation energy for reaction j	kJ/mol
E_{mp}	Maximum electron energy	eV
E_y	Electric field in y-direction	V/m
E_z	Electric field in z-direction	V/m
e	Electron charge	C

$\mathbf{F}$	Volume force vector	N/m^3
$\mathbf{F}_D$	Drag force	N
$\mathbf{F}_{ext}$	External forces	N
$\mathbf{F}_g$	Gravitational force	N
f	Frequency	Hz
f_c	Cut-off frequency	Hz
f_r	Resonant frequency	Hz
$\mathbf{g}$	Gravitational vector	m/s^2
H	Bed height	m or cm
H_j	Enthalpy of reaction	J/mol
H_m	Maximum spoutable bed depth	m
H_{TOT}	Total system enthalpy	MJ/kg
H_z	Magnetic field in z-direction	T

h	Planck's constant	$(m^2 \cdot kg)/s$
h_i	Molar enthalpy	J/mol
h_p	Heat transfer coefficient	$W/(m^2 \cdot K)$
$\mathbf{I}$	Identity Matrix	Unitless
I	Ionisation energy	J
j	Electric current density	A/m^2
$\mathbf{j}_j$	Diffusive flux of species k	$mol/(m^2 \cdot s)$
$\mathbf{J}$	Flux density	$1/(m^2 \cdot s)$
k	Boltzmann's constant	$m^2 \cdot kg/(s^{-2} \cdot K^{-1})$
k_0	Wave number of free space	1/m
k_c	Cut-off wavenumber	cm^{-1}
$k_{f,j}$	Rate coefficient of forward reaction	mol/s
k_i	Ionisation rate coefficient	1/s

$k_{r,j}$	Rate coefficient of reverse reaction	mol/s
k_j	Rate coefficient for reaction j	m^3/s
k_T	Thermal conductivity	W/(m·K)
l	Length	m or cm
M	Average molecular weight	kg/mol
M_k	Molecular weight of species k	kg/mol
$\dot{M}_{TOT}$	Total mass flow rate	kg/s
MW_{SiC}	Molecular weight of SiC	g/mol
m_e	Electron mass	kg
m_p	Particle mass	kg
N	Avogadro's constant	1/mol
N_n	Neutral species number density	1/m^3
n_e	Electron number density	1/m^3

n_ε	Electron energy density	eV/m^3
n_i	Ion number density	1/m^3
n_k	Number density of species k	1/m^3
p	Pressure	Pa
P	Electric polarisation vector	C/m^2
P_{10}^{TE}	Power associated with TE$_{10}$ mode	W
P_c	Dissipated power	W/m
P_f	Forwarded power	W
P_r	Reflected power	W
Q	Quality factor	Unitless
Q_h	Heat source for gas heating	W
Q_j	Heat source of reaction	J/(m^3·s)
q	Electron charge	C

R	Universal gas constant	$(m^3 \cdot Pa)/(K \cdot mol)$
R_e	Electron source term	$1/(m^3 \cdot s)$
R_ε	Electron energy loss	$eV/(m^3 \cdot s)$
R_k	Rate expression for species k	$kg/(m^3 \cdot s)$
R_s	Surface resistance	Ohm
r_j	Reaction rate of reaction j	$mol/(m^3 \cdot s)$
S_j	Entropy of reaction	$J/(mol \cdot K)$
s_i	Molar entropy	$J/(mol \cdot K)$
$\dot{s}_k$	Molar production rate	mol/s
T	Temperature	K
T_{amb}	Ambient temperature	K
T_e	Electron temperature	eV
T_g	Gas temperature	K

T_i	Ion temperature	eV
T_p	Particle temperature	K
t	Time	s
U_{ms}	Minimum spouting velocity	m/s
$\mathbf{u}$	Gas velocity vector	m/s
V	Cell volume	m^3
V_p	Electric potential	V
v_{kj}	Stoichiometric matrix	Unitless
v_{kj}^f	Stoichiometric matrix for forward reaction	Unitless
v_{kj}^r	Stoichiometric matrix for reverse reaction	Unitless
$\mathbf{v}^T$	Thermal drift velocity	m/s
$\mathbf{v_p}$	Particle velocity vector	m/s
W	Work function	eV

x_j	Mole fraction of target species for reaction j	Unitless
y_k	Mole fraction of species k	Unitless
Z_k	Charge of species k	C
Z_v	Number of valence electrons in atom	Unitless
α_c	Attenuation coefficient	Np/m
β	Propagation exponent	Unitless
β_j	Arrhenius temperature exponent	Unitless
$\Delta\varepsilon$	Energy transferred to electron	eV
$\Delta\varepsilon_j$	Energy loss from reaction j	eV
ΔP_s	Frictional pressure drop	kPa
δ	Skin depth	cm
ε	Energy	eV

$\bar{\varepsilon}$	Mean electron energy	eV
ϵ_0	Permittivity of a vacuum	F/m
ε_d	Walls emissivity	Unitless
ε_r	Relative permittivity	F/m
ϵ_v	Kinetic energy of valence electron	eV
η	Impedance	Ohm
η_0	Impedance of a vacuum	Ohm
γ	Energy fraction transferred	Unitless
γ_e	Electron multiplication coefficient	Unitless
γ_k	Sticking coefficient of species k	Unitless
λ_{mfp}	Mean free path	m
μ_e	Electron mobility	$m^2/(V{\cdot}s)$
μ_ε	Electron energy mobility	$m^2/(V{\cdot}s)$

μ_k	Dynamic viscosity of species k	Ns/m^2
μ_r	Relative permeability	H/m
μ_0	Permeability of a vacuum	H/m
ρ	Density	kg/m^3
ρ_c	Space charge density	C/m^3
ρ_f	Fluid density	kg/m^3
ρ_s	Solid density	kg/m^3
σ	Characteristic length of Lennard-Jones/ Stockmayer potential	Å
σ_0	Geometric atomic cross-section	cm^2
σ_i	Ionisation cross-section	cm^2
σ_j	Collision cross section	m^2
σ_c	Electrical conductivity	S/m
τ	Viscous stress tensor	Pa

υ	Collision frequency	1/s
Ω	Collision integral	Unitless
ω	Angular frequency	rad/s
ω_c	Critical frequency	Hz
ω_k	Mass fraction of species k	Unitless

Acronyms and Abbreviations

ANOVA	Analysis of Variance
BDF	Backward Differentiation Formula
BET	Brunauer–Emmett–Teller Analysis
CCD	Central Composite Design
CCP	Capacitively Coupled Plasma
CPU	Central Processing Unit
CVD	Chemical Vapour Deposition
DBD	Dielectric Barrier Discharge
DC	Direct Current
DoE	Design of Experiments
EDX	Energy-dispersive X-ray Spectroscopy
EEDF	Electron Energy Distribution Function
FCC	Face-centred Cubic
FTIR	Fourier Transform Infrared Spectroscopy
HTGR	High Temperature Gas-cooled Reactor
HTR	High-temperature Reactor
IAEA	International Atomic Energy Agency

ICP	Inductively Coupled Plasma
LOCA	Loss-of-coolant Accidents
LTE	Local Thermal Equilibrium
LWR	Light Water Reactor
MTS	Methyltrichlorosilane (CH_3SiCl_3)
MW	Microwave
MW-PECVD	Microwave Plasma-enabled Chemical Vapour Deposition
NECSA	South African Nuclear Energy Corporation
ODE	Ordinary Differential Equation
PDE	Partial Differential Equation
PECVD	Plasma-enabled Chemical Vapour Deposition
PBMR	Pebble Bed Modular Reactor
PIC	Particle-in-cell
PLD	Pulsed-laser Deposition
RSM	Response Surface Methodology
RF	Radio-frequency
SEM	Scanning Electron Microscopy
SiC	Silicon Carbide

SSD	Silicon Drift Detector
TE	Transverse Electric
TEM	Transmission Electron Microscopy
	or Transverse Electromagnetic
TM	Transverse Magnetic
TGA	Thermogravimetric Analysis
TRISO	Tri-isotropic
XPS	X-ray Photoelectron Spectroscopy
XRD	X-ray Diffraction

CHAPTER I:
INTRODUCTION

1 Introduction

1.1 Background

The physical and mechanical properties of silicon carbide (SiC) favour its application in high power and high frequency electronics as well as high temperature technologies [1, 2]. The material is receiving increased consideration for use as a nuclear ceramic due to its excellent mechanical properties, and dimensional stability under irradiation. The low neutron-absorption cross-section (25 % that of zirconium-based alloys) invokes classification as a proposed replacement material for zirconium alloy-based fuel cladding in light water reactors [3]. The high-temperature mechanical performance of silicon carbide (SiC) is an important factor contributing towards its use as a fission product barrier in tri-isotropic (TRISO) fuel, shown in Figure 1.1, and its consideration as a host material for high level radioactive waste immobilisation [4].
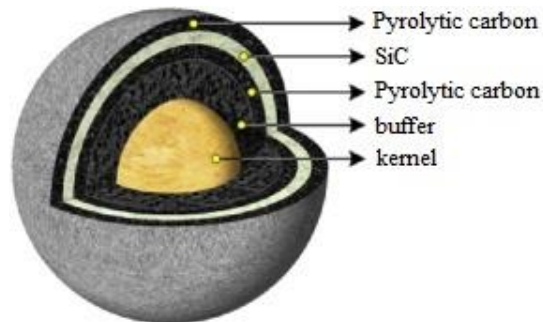
Figure 1.1: Layer composition of TRISO fuel particles [4].

The current standard method for TRISO fuel fabrication involves chemical vapour deposition (CVD) in a fluidised bed furnace [5]. The synthesis reaction is shown in Equation (1.1) and has been extensively reported in the literature [6-8].

$$CH_3SiCl_3(l) \rightarrow SiC(s) + 3HCl(g) \tag{1.1}$$
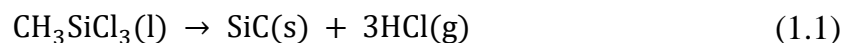
Many different manufacturing methods for the creation of SiC particles and layers have been reported, including carbothermic reduction [9], pulsed-laser deposition (PLD) [10, 11], sol-gel preceramic polymers [12], and microwave heating [13, 14]. Additionally, numerous plasma-enabled chemical vapour deposition (PECVD) techniques have been reported for the deposition of SiC [15], including inductive radio-frequency (RF) [16-18], direct-current (DC) thermal [19], low-pressure microwave plasmas [20] and microwave plasma-enabled chemical vapour deposition (MW-PECVD) [21, 22]. Among these techniques, MW-PECVD has produced promising results [20-24], and provides economic advantages such as decreased energy requirements and reduced equipment footprints [25]. Microwave plasmas have also been used for the synthesis of other materials such as Si [26], MoS_2 and WS_2 [27], WO_3 [28] and Zn and ZnO [29]. In combination with this plasma technique, fluidised -and spouted bed reactors have also produced promising results for deposited coatings on particles [30, 31] due to the added advantage of high mass- and heat-transfer rates, and high bulk temperatures [32].

1.2   Problem Statement

Next generation high-temperature reactor (HTR) designs require operating temperatures of over 1 000 °C, emphasising the importance of obtaining detailed knowledge of the SiC deposition parameters and consequently the layer properties [33]. The current standard method for TRISO fuel fabrication entails high-temperature CVD inside a fluidised bed furnace [5]. This proven technique provides stable and consistent results but demands a high-energy input in order to deliver the temperatures required for MTS decomposition, yielding crystalline SiC. Very few studies have investigated the possible advantages of SiC layer growth in a MW-PECVD spouted bed reactor, compared to traditional synthesis methods.

1.3 Objective

In this study, a microwave plasma-enabled spouted bed reactor was used for the *in situ* synthesis and deposition of SiC layers onto alumina spheres in order to investigate MW-PECVD as a viable alternative deposition technique for high quality SiC layers.

1.4 Experimental Scope

MTS was used as precursor, due to its advantageous carbon-to-silicon ration of 1:1, and argon served as both plasma- and carrier gas. The effect of hydrogen-to-MTS molar ratio (H_2:MTS) was investigated, as well as the effect of reactor pressure and enthalpy on the deposited layer characteristics. A bed size of 50 pebbles was used per experimental run, and a 3D central-composite experimental design was followed.

1.5 Thesis Overview

Chapters 2, 3 and 4 summarise the relevant literature. Chapter 2 introduces some relevant elementary plasma physics, attempting to elucidate the key plasma terms and jargon for the reader. The chapter also highlights some design considerations for microwave components and reactor designs. Chapter 3 is a brief introduction to silicon carbide, highlighting its history, material properties and synthesis methods. The decomposition kinetics of MTS are also briefly discussed. Chapter 4 concludes the literature with a brief introduction to spouted bed design and applications, as well as the current literature on MW-PECVD spouted bed reactors.

The experimental setup, method, design and characterisation equipment are described in Chapter 5. The results and discussion are reported in Chapter 6 which includes experimental measurements, such as mass-deposition rates, and statistical analyses. This includes the ANOVA analysis and surface contour plots, layer and morphology characterisation, as well as elemental and crystallographic analyses. Chapter 7 presents a

2D model representative of the physical setup and attempts to simulate the conditions present during an experimental run using a conventional finite-elements software package. The final conclusions and recommendations are reported in Chapter 8, summarising the key findings of this experimental study, as well as the necessary work to be undertaken in future investigations.

CHAPTER II:
PLASMA & MICROWAVE TECHNOLOGY

2 Plasma & Microwave Technology

2.1 Introduction

The goal of this chapter is to familiarise the reader with the relevant aspects of plasma- and microwave technologies, as well as introduce the core methods and mathematical descriptions needed for microwave plasma modelling. Some key terms and definitions are first described in Section 2.2, followed by the most common plasma-chemical reactions described in Section 2.3, which are expanded upon in Appendix A. A brief overview of various plasma sources is given in Section 2.4, followed by a brief introduction into the core concepts of microwave components and design in Section 2.5. The overall modelling and simulation method for plasmas is described briefly in Section 2.6, followed by a more specific description of microwave plasma modelling in Section 2.7. The domain equations are expanded upon in Appendix C. Plasma diagnostics are discussed in Section 2.8.

2.2 Plasma Definitions & Terms

As temperature increases, states of matter "decompose" to less structured, more chaotic systems. A solid lattice changes to less tightly-bound liquid movements, which further changes to unbound gas molecules, governed by collisions. The gas phase further changes to a collection of charged ions and neutral particles which behave differently from their atomically neutral counterparts. The latter is known as the plasma state and it is often pointed out that over 95 % of the visible universe is in the plasma state. In physics and engineering, a plasma must conform to three main conditions [34]:

- Quasi-neutrality ($n_i \simeq n_e$);
- ionisation of the gas ($A \rightarrow A^+ + e$); and
- exhibition of collective behaviour i.e. the motions depend on both local -and remote conditions.

2.2.1 Plasma Temperatures

A gas in thermal equilibrium contains particles of all velocities (u), and follows a typical Maxwell-Boltzmann distribution, described by Equation (2.1) and shown visually in Figure 2.1.

$$f(u) = A \exp\left(-\frac{\frac{1}{2}mu^2}{kT}\right) \tag{2.1}$$

Here, k is Boltzmann's constant, m is mass, T is a parameter based on the mean kinetic energy of the particles indicated by $\bar{E}$ in Figure 2.1, and A is a constant related to number density, n, given by:

$$A = n\left(\frac{m}{2\pi kT}\right)^{\frac{3}{2}} \tag{2.2}$$

In Figure 2.1, E_{mp} is the maximum electron energy and $\bar{E}$ is the average electron energy [35].
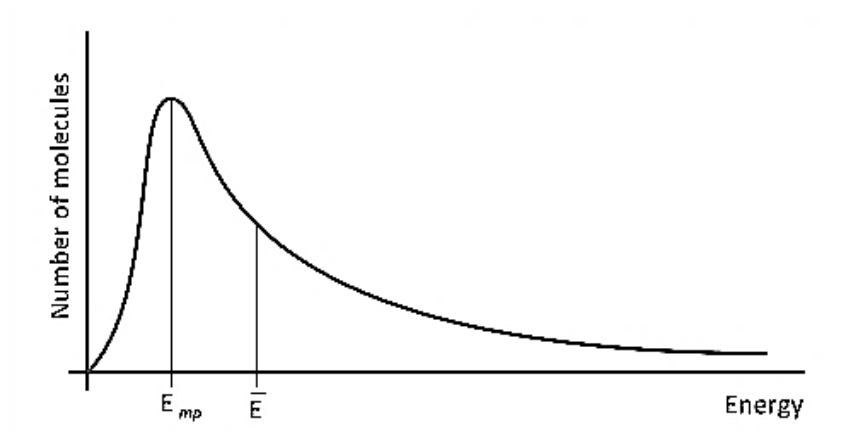
Figure 2.1: Typical shape of a Maxwell-Boltzmann distribution function.

The width of this distribution is characterised by a constant value for T in Equation (2.1), and this is what *temperature* refers to in plasma physics (Figure 2.2). Plasmas can have different *temperatures* for different species, e.g. electron temperature, ion temperature, neutral particle temperatures, each described by a Maxwell-Boltzmann distribution.
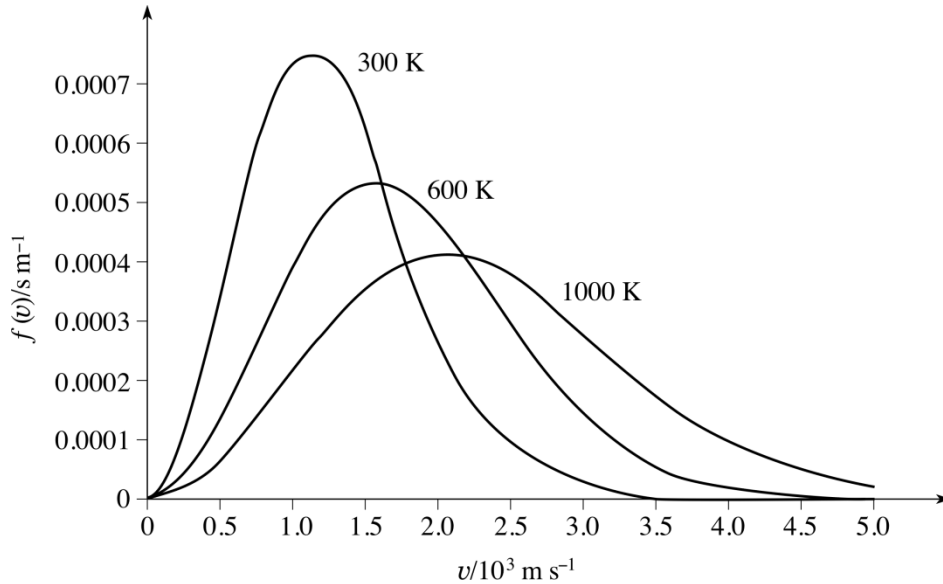
Figure 2.2: Maxwell-Boltzmann distributions at different constant temperatures [36].

In three dimensions, the average kinetic energy of particles is given by Equation (2.3).

$$E_{ave} = \frac{3}{2}kT_e \tag{2.3}$$

It is customary in plasma physics to give temperatures in terms of energy units, usually electron volts (eV), where:

$$1 \text{ eV} = 11\,600 \text{ K} = 1.6 \times 10^{19} \text{ Joules}$$

The properties of a plasma vary with electron density and temperature. These parameters change, based on the type of energy supply and the amount of energy transferred to the plasma. A plasma is considered to be in local thermodynamic equilibrium (LTE) when the electron temperatures are close to the heavier particle temperatures. LTE also requires chemical reactions to be governed by collisions only and not by radiative processes, that collision phenomena have to be micro-reversible, and that diffusion time must be sufficient for particles to reach equilibrium [37]. LTE requires higher collisional exchanges, higher densities and higher pressures, and hence requires higher power delivered to the plasma [37].

Numerous plasmas exist far from thermodynamic equilibrium (non-thermal), however, and are characterised by multiple temperatures related to different plasma particles. This can also be described as a departure from the Boltzmann-distribution patterns for the density of excited atoms. It is, however, the electron temperature in particular that often differs significantly from that of heavier particles [37]. Non-thermal plasmas are usually generated at low pressures and low power levels. Thermal plasmas are usually characterised by higher electron densities, whereas non-thermal plasmas are more selective (lower electron densities). These characteristics affect the engineering aspects and application areas of these two types of plasmas.

2.3   Plasma-Chemical Reactions

Reaction rates are affected by reaction cross-sections, probabilities and electron energy-distribution functions. The reaction rate is a result of integration of the reaction cross-section over the relevant distribution function [35]. The most relevant elementary plasma-chemical reactions are discussed here.

2.3.1 Ionisation Processes

Ionisation is a key process in plasma chemistry and entails the conversion of neutral atoms or molecules into electrons and positive ions. In electronegative gases with high electron affinity (e.g. O_2, Cl_2, SF_6, UF_6), negative ions are also formed. Ionisation processes are subdivided into five different groups, and are briefly described in Appendix A. Electrons are the first to gain energy from electric fields due to their low mass, and transmit the energy to other components through collisions. This energy is used for ionisation, excitation and dissociation processes. Rates are therefore dependent on the number of electrons with adequate energy to initiate a reaction. This is described by means of the electron energy-distribution function (EEDF) which is the probability density for an electron to have a particular energy, ϵ [35]. The EEDF strongly depends on the electric field strength (and hence electron temperature) as well as gas composition in the plasma.

The average electron energy can be determined by Equation (2.3). In most plasmas, E_{ave} varies between 1 eV and 5 eV. Ion energies can also be described by an energy-distribution function, and at low pressures they are often similar to the Maxwellian distribution function above, with ion temperature, T_i, close to the gas temperature, T_g [35].

2.3.2 Elastic & Inelastic Collisions

Elementary processes can generally be divided into two categories: Elastic and inelastic. During elastic collisions the internal energies do not change, the kinetic energy is conserved, and it results in only geometric scattering & redistribution of kinetic energy. Inelastic collisions, however, change kinetic energy into internal energy. These processes can be described by six collision parameters, reported in Appendix B.

2.3.3 Coulomb Collisions

Electron-electron, electron-ion and ion-ion scattering processes are all classified as coulomb collisions. Energy transfer between these particles during elastic collisions is only possible in the form of kinetic energy. The fraction, γ, of energy transferred from particle A to particle B is given by:

$$\gamma = \frac{2m_A m_B}{(m_A + m_B)^2} \tag{2.4}$$

For electron collisions with heavy particles, $m_A \ll m_B$ and therefore the fraction of energy transferred is very small ($\gamma \sim 10^{-4}$). Therefore only electron-electron impacts allow for significant energy transfer [35].

2.4 Plasma Sources

Excitation frequencies influence the behaviour of the electrons and ions in a plasma, and the different plasma sources can be classified according to the excitation mode [37]:

- Direct current (DC) discharges;
- radio frequency (RF) discharges; and
- microwave discharges.

Figure 2.3 illustrates the occurrence of some plasma sources with varying frequency.

Electrons & ions follow oscillations of electric field

Only electrons follow oscillations of electric field. Ions only affected by average temporal values of local field.

Similar behaviour as previous regime.

1 kHz   10 kHz   100 kHz   1 MHz   10 MHz   100 MHz   1 GHz   10 GHz

Direct current/low frequency   Radio frequency   Microwave
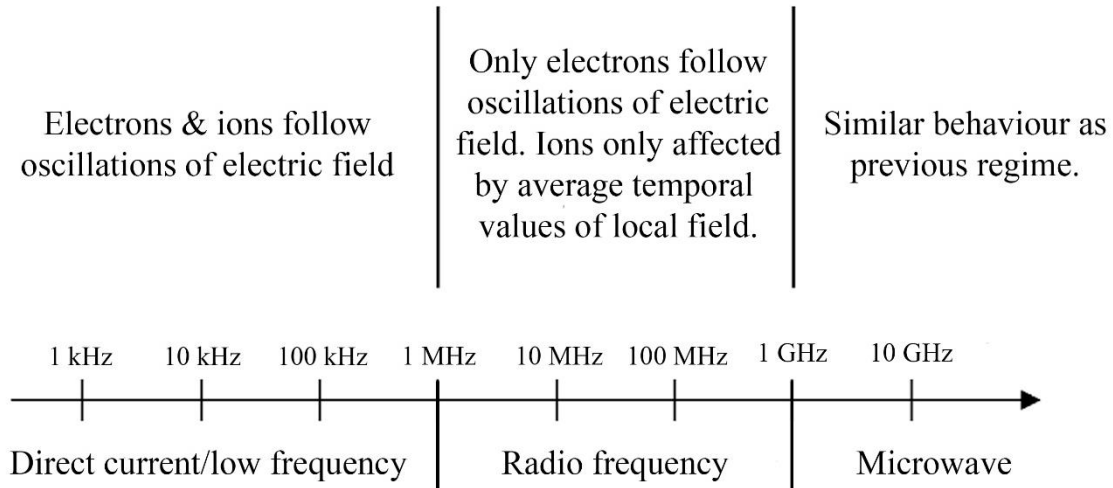
Figure 2.3: Electron and ion behaviour with frequency range, adapted from [37].

2.4.1 DC Discharges

Plasma in DC discharges are generally created in closed discharge vessels using interior electrodes. Numerous types of discharges can be obtained by varying the applied voltage and discharge current [38, 39]. Different types of DC discharges are categorised in Figure 2.4.

The pulsed mode DC discharges have the advantages of higher operating power, additional performance control and more homogeneous film deposition [39]. The pulsed power supply, however, is more complex in design and affects reproducibility of the process [37].
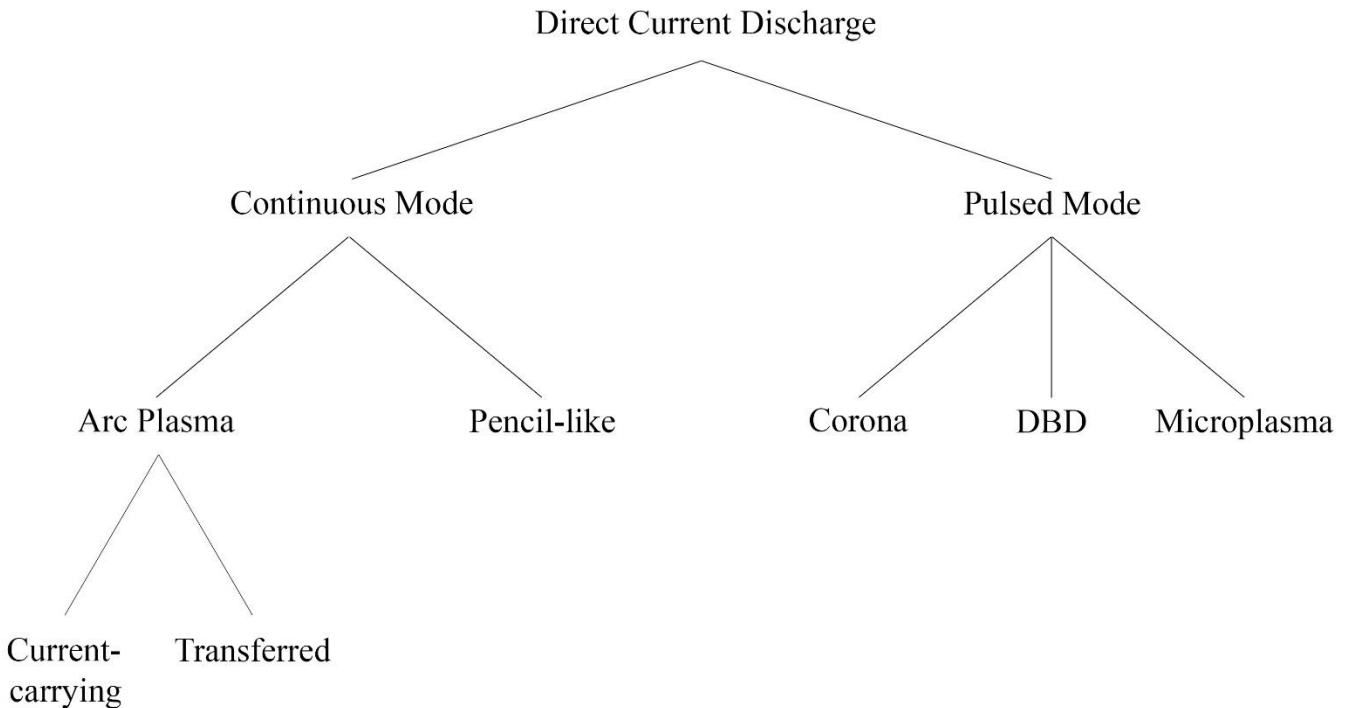
Figure 2.4: Classification of DC plasmas.

2.4.2 RF Discharges

Plasmas can be generated at high power levels using RF discharges. Despite the higher cost, different types of RF discharges are gaining increasing popularity due to the absence of direct contact between the plasma and electrode(s). Many of these discharge systems are electrodeless and therefore electrode-related problems are not a major concern [40]. The RF electric field interactions with the plasma can be either inductive or capacitive. The inductively coupled plasma (ICP) is excited and maintained using a coil in close proximity to a gas stream. High-frequency electric current is passed through the coil, where a magnetic field is induced along the axis of the discharge tube. The resulting electric field accelerates the electrons and thus maintains the plasma [37]. Alternatively, capacitively coupled plasmas (CCPs) generate higher values for the electric fields than ICPs do. As in a capacitor, the electric field is now the primary effect. These higher electric field values

15

make it possible to generate non-LTE plasmas that are used in material treatment such as electronics [40].

2.4.3   Microwave Discharges

Microwave systems are electrodeless, and the same principle applies to all variations. Microwaves are guided along the system, through some form of metallic waveguide, and transmit energy directly to the plasma gas electrons. Whereas RF discharges operate with wavelengths of approximately 22 m, microwave plasmas are sustained by electromagnetic waves in the centimeter range, which is comparable to the size of the physical system [37]. This form of plasma generation will be discussed further in the following sections.

2.5   Microwave Components & Design

Transmission lines, such as waveguides, and their corresponding cavities represent significant aspects in many practical radio-frequency systems. In this section the fundamentals of waveguide design will be introduced, as well as their electromagnetic field propagation characteristics. Also, the significance in varying geometries (rectangular and cylindrical) will be discussed and compared, and ultimately the design and characteristics of their corresponding cavities. This process includes discussions of cut-off frequencies, attenuation constants and quality factors used to describe cavities.

2.5.1   Transverse Electromagnetic Modes

Electromagnetic field configurations are known as *modes*. Analysing these fields within any region is dependent upon solving the Maxwell field equations in a coordinate system appropriate to the region. For any particular problem various field configurations, or solutions, exist that satisfy the wave equations, Maxwell's equations, and the boundary conditions [41]. In several regions of practical importance, such as waveguides, the dimensions and field excitation only allow for a single mode capable of propagation [42]. As a result, the electromagnetic field at most points in space is characterized by the

amplitudes of this one dominant mode type. The three general modes are Transverse Electromagnetic (TEM), Transverse Electric (TE) and Transverse Magnetic (TM). In the TEM mode both the electric and magnetic fields are perpendicular to the direction of propagation, however no TEM solutions exist for hollow rectangular waveguides [43]. TE modes are characterized by the conditions:

$$E_z = 0 \qquad\qquad (2.5a)$$

$$H_z \neq 0 \qquad\qquad (2.5b)$$

Here, E_z and H_z are the electric and magnetic fields in the z-direction (see Figure 2.5) [44]. In contrast, TM modes are characterised by:

$$E_z \neq 0 \qquad\qquad (2.6a)$$

$$H_z = 0 \qquad\qquad (2.6b)$$

2.5.2 Rectangular Waveguides

Waveguides are used to transfer electromagnetic power efficiently from one point in space to another. Typical guiding structures are shown in Figure 2.5. The choice of guide structure is usually a function of:

- The operating frequency;
- the power transfer load; and
- the percentage of transmission losses that can be tolerated [44].
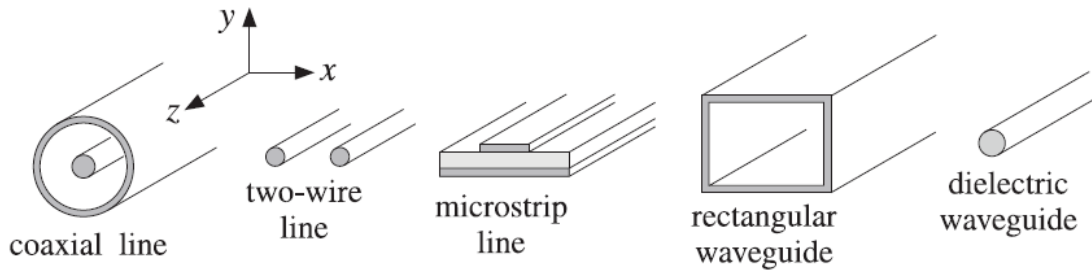
Figure 2.5: Various waveguide structures [44].

Consider a rectangular cross section waveguide with dimensions a and b, illustrated in Figure 2.6.
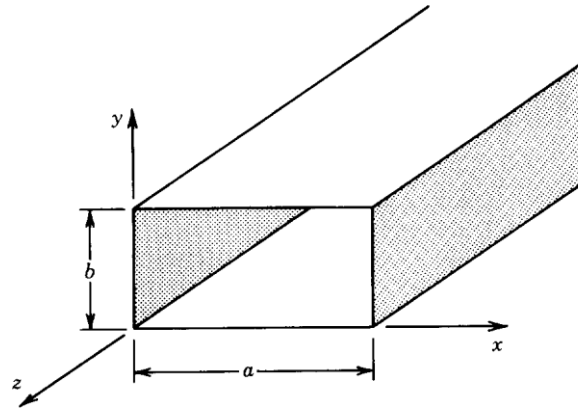
Figure 2.6: Cross section of a typical rectangular waveguide [41].

For the rectangular waveguides, the TE mode expressions are a function of cut-off wave number, k_c.

$$k_c = \omega_c\sqrt{\mu\epsilon} = 2\pi f_c\sqrt{\mu\epsilon} = \sqrt{\left(\frac{m\pi}{a}\right)^2 + \left(\frac{n\pi}{b}\right)^2} \quad m, n = 0,1,2 \text{ ....} \quad (2.7a)$$

or

$$f_c = \frac{1}{2\pi\sqrt{\mu\epsilon}} \sqrt{\left(\frac{m\pi}{a}\right)^2 + \left(\frac{n\pi}{b}\right)^2} \quad m, n = 0,1,2, \dots \tag{2.7b}$$

Here, ω_c is the critical plasma frequency, μ is permeability, ϵ is permittivity, f_c is the cut-off frequency, and m, n are indices that only allow for discrete solutions for k_c due to the physical boundaries of the waveguide walls. From Equation (2.7) it is evident that for $m = n = 0$ the value of k_c becomes 0, and is therefore a trivial solution [45]. It also implies that no TEM mode can propagate through a hollow metallic waveguide.

The values of f_c for different combinations of m and n but fixed values of ϵ, μ, a and b determine the cut-off frequencies and the order of existence of different modes above f_c. Table 2.1 shows the TE mode cut-off frequencies for various combinations of m and n for a rectangular waveguide with cross-sectional dimensions $a = 86$ mm and $b = 43$ mm. The values of ϵ and μ were taken for air.

Table 2.1: TE$_{mn}$ cut-off frequencies.

m	n	f_c (GHz)
1	**0**	**1.74**
2	0	3.49
0	1	3.49
1	1	3.90

19

At a frequency of 2.45 GHz, only the TE$_{10}$ mode can propagate and is called the *dominant* mode [45]. Using a similar method it can be shown that for rectangular waveguides, TM propagation modes are also possible, however TE modes are always dominant [41].

2.5.3 Power

The fields propagating through the waveguide have a corresponding power associated with them [41], given by:

$$P_{10}^{TE} = |A_{mn}|^2 \frac{\beta^2}{2\eta\epsilon^2} \left(\frac{a}{\epsilon_{0m}}\right)\left(\frac{b}{\epsilon_{0n}}\right) \sqrt{1 - \left(\frac{f_c}{f}\right)^2} \qquad (2.8)$$

where P_{10}^{TE} is the power associated with a TE$_{10}$ mode, β is the propagation exponent, η is the impedance, and A_{mn} is a constant given by:

$$|E_y|_{max,air} = \frac{|A_{mn}|}{\epsilon_0}\frac{\pi}{a} = 3 \times 10^6 \text{ (V/m)} \qquad (2.9)$$

and ϵ_{0q} is given by:

$$\epsilon_{0q} = \begin{cases} 1 & \text{if } q = 0 \\ 2 & \text{if } q \neq 0 \end{cases} \qquad (2.10)$$

For an air-filled rectangular waveguide with $a = 86$ mm and $b = 43$ mm, the maximum power that can be transmitted at 2.45 GHz in the waveguide before air breakdown occurs is determined by:

$$P_{10}^{TE} = |A_{10}|^2 \frac{(\beta_c)_{10}^2}{2\eta_0 \epsilon_0^2} \left(\frac{a}{\epsilon_{00}}\right)\left(\frac{b}{\epsilon_{01}}\right)\sqrt{1 - \left[\frac{(f_c)_{10}}{f}\right]^2} \tag{2.11}$$

where

$$(\beta_c)_{10} = \frac{\pi}{a} \tag{2.12}$$

For a wave propagating in air, and assuming a perfect dielectric ($\eta_0 = 377$ and $\epsilon_0 = 8.854 \times 10^{-12}$), the maximum power that can be transmitted is:

$$P_{10}^{TE} = 15.5 \times 10^3 \text{ kW}$$

2.5.4 Attenuation

Many good conductors exist, such as metals, although attenuation always occurs due to ohmic losses in the waveguides. This is accounted for by the addition of an attenuation coefficient, α_c. To determine the ohmic losses associated with the conducting walls is a complicated task, but is approximated using a perturbational method, the derivation of which can be found elsewhere [41]. For a TE mode, the attenuation coefficient is given by:

$$(\alpha_c)_{mn} = \frac{2R_s}{b\eta\sqrt{1 - \left(\frac{f_c}{f}\right)^2}} \left\{ \left(1 + \frac{b}{a}\right)\left(\frac{f_c}{f}\right)^2 + \frac{b}{a}\left[\frac{\epsilon_{0n}}{2} - \left(\frac{f_c}{f}\right)^2\right]\frac{m^2 ab + (na)^2}{(mb)^2 + (na)^2} \right\} \tag{2.13}$$

where R_s is the surface resistance of the waveguide walls, given by:

$$R_s = \frac{1}{\sigma_c \delta} \tag{2.14}$$

where σ_c is the electrical conductivity, and δ is the skin depth of the waveguide walls operating at frequency f, and is given by:

$$\delta = \frac{1}{\sqrt{\pi f \mu \sigma_c}} \tag{2.15}$$

Using Equation (2.13) for a TE_{10}-mode wave travelling through an aluminium waveguide with dimensions $a = 86$ mm and $b = 43$ mm, the final attenuation coefficient is:

$$\alpha_c = 2.87 \times 10^{-3} \text{ Np/m}$$

The total dissipated power per unit length can then be described by:

$$P_c = 2\alpha_c z P_0 e^{-2\alpha_c z} \tag{2.16}$$

where P_0 is the power at some reference point ($z = 0$) and z is the distance from the reference point. Assuming $P_0 = 1\ 000$ W and taking $z = 1$ m, the dissipated power is determined to be:

$$P_c = 5.71 \text{ W/m}$$

This is a total power dissipation of 0.57 % over the length of the waveguide (assuming a length of 1 m), an almost negligible effect compared to the total forwarded power. For much longer waveguides ($z > 10$ m), however, the power dissipation becomes increasingly relevant, and should be considered during the design procedure.

22

In the case of a lossy dielectric material filling the waveguide, an additional attenuation coefficient is introduced, α_d. If the waveguide is only filled with air, however, this coefficient is assumed to be negligible [41].

2.5.5 Resonant Cavities

The microwave resonator functions in the same way as a resonant circuit, where stored energy is transferred between an inductor and a capacitor which store magnetic and electric energy, respectively. A microwave resonator cavity only stores this energy spatially while exchanging electric and magnetic energy [46]. Microwave cavities can also be constructed from closed-off sections of waveguides and coupling to the cavity resonator occurs through a small aperture, or a small probe or loop [47]. These resonators are described in terms of their quality factor, Q, given by

$$Q = 2\pi f_r \frac{\text{stored energy}}{\text{dissipated power}} \tag{2.17}$$

which is proportional to volume and inversely proportional to surface. Typical Q factors range in the order of 5 000 to 10 000 [41].

2.6 Modelling & Simulation of Plasma Processes

Plasma processes contain a mixture of fluid mechanics, reaction engineering, physical kinetics, heat transfer, mass transfer, and electromagnetic theory. This complex interaction of various physical processes greatly increases the difficulty in accurately modelling such a rigorous system. Computer simulations have greatly decreased the time needed to produce relevant results and have become an important tool to understand the effects and consequences of multiphysics interactions.

Two simulation methods are generally used for plasma processes, namely particle-in-cell (PIC) and fluid simulations. A brief comparison of the two methods is shown in Table 2.2.

Table 2.2: Comparison of two main plasma simulation methods.

Particle-in-cell (PIC)	Fluid simulation
Accurate	Suitable for high-pressure plasmas
Time consuming	Non-local effects not important
Tracks particle trajectories	Uses drift-diffusion approximation
Resolves space-and time dependant velocity distribution functions without prior assumptions	Faster than PIC simulations
Commonly used to study low-temperature plasmas	Uses macroscopic properties (e.g. density, mean velocity)
	Solves moments of Boltzmann equation

Physical parameters are difficult to measure in experiments, but can be obtained in simulations more easily. Despite the progress in recent decades with regard to plasma simulations, computational limitations still require approximations. Most plasma chemical systems today are simulated using fluid modelling software (e.g. COMSOL® Multiphysics).

2.7   Microwave Plasma Modelling

Microwave-assisted plasmas rely on the photo-ionisation mechanism (Appendix A) where seed electrons are generated through the collision of energetic photons (2.45 GHz) with neutral atoms. Collisions with the seed electrons subsequently result in other ionisation and/or dissociation processes. Microwave generators, particularly magnetrons operating in the GHz frequency range and with power supplies operating between 1 kW and 2 kW, are able to maintain LTE microwave discharges from low to atmospheric pressures [35]. Various possibilities exist through which the electromagnetic energy in the discharges can be coupled with the plasma, the most typical of which is through waveguides. Plasma is ignited and maintained inside a tube, usually quartz, that passes perpendicular through the rectangular waveguide and is transparent to electromagnetic waves. Any interaction between the propagating wave and the plasma results in both dissipation and reflection of the wave. Roughly half of the incident microwave power is dissipated in the plasma, one quarter is transmitted, and another quarter is reflected. To increase the coupling effectiveness, the transmitted wave can be reflected backwards, resulting in the formation of a standing wave [40].

A microwave plasma is mathematically described through the complex interactions of drift diffusion (electron transport), heavy species transport, electrostatics and electromagnetic wave equations. The high-frequency electric fields and their associated losses are computed via a complex plasma conductivity, and the absorption of electromagnetic waves is realised through a complex electrical conductivity. The diffusion and velocity vectors of the gasses (usually argon and hydrogen) and their accompanying dynamic viscosities, are additionally calculated via a computational flow dynamic interface, described by fluid flow equations. Heating of the gas is calculated through the Boltzmann EEDF and the heat equations. Dependent variables include the electric field components, electric potential,

electron density, and electron energy density. The domain equations for the various aspects of microwave plasma modelling are described in Appendix C.

2.8 Plasma Diagnostics

Various diagnostic techniques exist for the characterization of plasma systems. Most are determined by electron and gas temperatures and tend to be quite complex measuring processes. Some general ones are discussed briefly in the following sections.

2.8.1 Spectroscopy

Spectral diagnostics are based on measuring the intensity of spectral lines of emission -and absorption spectra as well as the continuous spectrum. Spectral emission lines can be used for the determination of the temperature profile via Boltzmann plots. The Boltzmann method allows for the calculation of plasma temperatures and pressures if calibrated emission coefficients of the spectral lines are available, which is not always the case [48]. Emissivity spectra can be obtained by Abel inversion of intensity spectra measured from a thin plasma slice perpendicular to the plasma axis. From measured emissivity spectra, spatial and temporal distributions of plasma temperature and number densities of plasma species (atoms, ions, and electrons) can be obtained [49].

Species concentration at the periphery of a plasma object can be determined from absorption lines. Absorption lines are obtained in a background of a continuous spectrum and are characterised by the total absorption value [50]. The continuous spectrum of low-temperature plasmas forms due to recombination of the electron and ion and the deceleration of the electron in the ion field. Plasma and electron temperatures can be determined from this method and do not require that LTE exists in the plasma [50].

Other diagnostic techniques include determination of the velocity-distribution type of excited particles from spectral measurements [50], measurement of gas temperature from

Doppler broadening of spectral lines [50], and determining the electron concentration from the Stark broadening of the spectral lines [50].

2.8.2   Probe Measurements

The electric probe is a small metallic electrode placed in the plasma and used to determine its characteristics. It usually measures the volt–ampere (*V-I*) characteristics of the system. The system normally includes a measuring probe, a reference electrode and a voltage source. This method for plasma diagnostics, however, faces a number of difficulties which restrict the advantages of the method associated with its apparent simplicity [50]. Measurements become complicated when the mean free path, λ_{mfp}, of charged particles is smaller or equal to the characteristic probe size. In this case, the electric probe starts to disturb the examined plasma significantly in the vicinity and this affects the concentration of charged particles in this region [50].

Also, in the presence of chemical reactions, when dielectric or other coatings grow on the probe surface or when the dimensions of the probe decrease as a result of etching its surface layers, deviations can occur from the normal operating regime of the probe [50].

2.8.3   Thermocouple

For non-equilibrium plasmas at low pressures, the thermocouple is often used to determine the gas temperature as well as thermal effects of the recombination and deactivation reactions on the surface [50]. Two design variants of the thermal probe include:

- A thermocouple coated (or not) with a dielectric screen, and temperature is determined through the measured value of electromagnetic frequencies; and
- a thin wire with two lead-outs, and temperature is determined by the change of electrical resistance of the wire.

2.8.4 Langmuir Probes

The Langmuir probe (Figure 2.7) is used for low-temperature plasmas to measure the plasma density, electron temperature and the plasma potential. The design consists of a bare wire or metal disk, which is inserted into a plasma and electrically biased with respect to a reference electrode to collect electron and/or positive ion currents. The probe is used to obtain the *V-I* characteristics of the probe-plasma system [51].
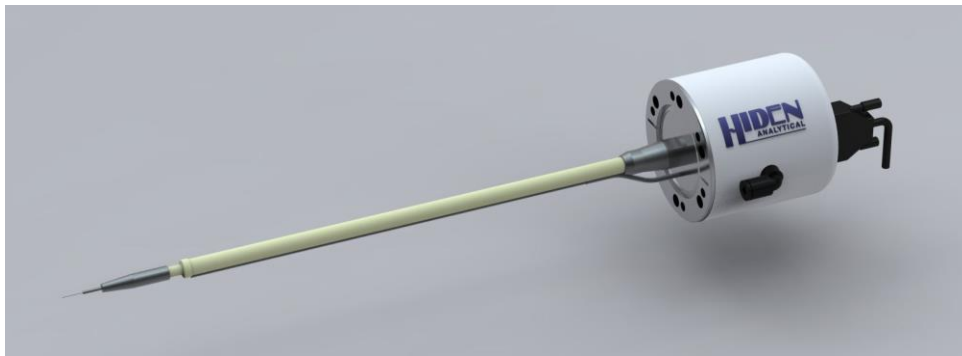
Figure 2.7: Langmuir probe from ESPion.

2.8.5 Enthalpy Probes

The enthalpy probe is a device introduced into the gas flow in order to measure the specific enthalpy, temperature and composition of plasma. The methods of measurement and the design of the enthalpy probes are greatly varied [50]. The tube can also act as a pitot tube for velocity measurements. Figure 2.8 shows a comparison of the different temperature regimes where various plasma diagnostic techniques are more appropriate.
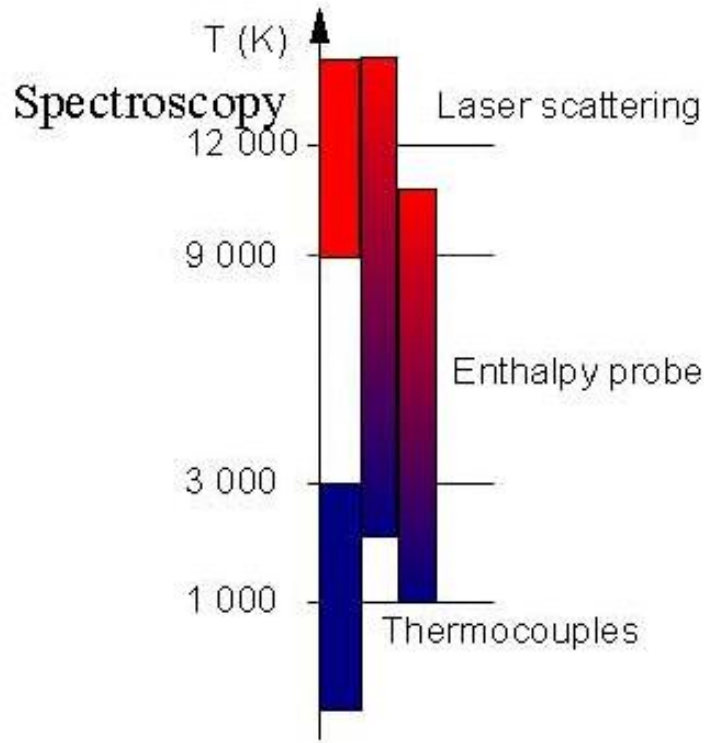
Figure 2.8: Measuring regimes of various plasma diagnostic techniques.

2.9 Summary

Microwave plasma systems are described via complex interactions between photons, electrons and heavier particles such as ions and neutral atoms/molecules. Knowledge of some introductory plasma definitions and terms is therefore important for understanding and predicting microwave plasma behaviour. In this chapter, the fundamental concepts of plasma- and microwave physics and terminologies were discussed, including key definitions, the fluid description of a plasma, and the numerous plasma-chemical reactions governed through electron impacts. Microwave-assisted plasmas rely on the photo-ionisation mechanism where seed electrons are generated through the collision of energetic photons with neutral atoms. Collisions with the seed electrons subsequently result in other ionisation and/or dissociation processes. Knowledge of microwave components design is crucial to allow for optimal "coupling" of the microwaves (i.e. photons) with the plasma

BESTPFE.COM
List of research project topics and materials

system to ensure that seed electrons are continuously produced in sufficient numbers. This includes the design aspects of rectangular waveguides, along with their dominant propagation modes and cut-off frequencies. Various diagnostic techniques exist for the characterization of plasma systems. Most are determined by electron and gas temperatures, and tend to be quite complex measuring processes.

Modelling of plasma systems is simplified using fluid-simulation methods, as opposed to PIC-simulation methods which require more processing power. Even when applying the fluid-simulation method, modelling of a microwave plasma is a complex task and requires powerful modelling software, such as COMSOL® Multiphysics. A microwave plasma can then be described mathematically through the complex interactions of drift diffusion (electron transport), heavy species transport, electrostatics and electromagnetic wave equations. The diffusion and velocity vectors of the gasses (usually argon and hydrogen) and their accompanying dynamic viscosities, are additionally calculated via a computational flow dynamic interface, described by fluid flow equations. Heating of the gas is calculated through the Boltzmann EEDF and the heat equations.

CHAPTER III:
SILICON CARBIDE:
PROPERTIES, SYNTHESIS AND DEPOSITION

3 Silicon Carbide: Properties, Synthesis & Deposition

3.1 Introduction

In this chapter, the material properties and characteristics of SiC are presented, along with various synthesis methods currently being investigated. A short history of SiC's discovery is given in Section 3.2, followed by a brief discussion of its various crystalline forms and their accompanying defects in Section 3.3 and Section 3.4, respectively. The large-scale production methods of SiC are discussed in Section 3.5, followed by some of SiC's physical properties in Section 3.6. The thermal decomposition of an organic precursor (MTS) to form SiC is discussed in Section 3.7, and special note is made of microwave synthesis of SiC in Section 3.8 to distinguish it from microwave plasma-assisted synthesis. Some plasma-assisted synthesis methods are accordingly discussed in Section 3.9, and the chapter concludes with a short introduction into the nuclear properties of SiC in Section 3.10.

3.2 History

Jöns Jacob Berzelius, best known for the discovery of silicon (Si), was most likely the first person to synthesize silicon carbide (SiC) in 1824, when he published a paper hypothesising a chemical bond between silicon (Si) and carbon (C) in one of the samples he produced [2]. Edward Goodrich Acheson would later discover a crystalline product characterised by high hardness, refractability and infusibility by mixing coke and silica in a furnace. Acheson called this product "carborundum" and gave it the correct formula, SiC [2]. By the end of the century, Henri Moissan found natural SiC in the Canyon Diablo meteorite in Arizona, USA, giving rise to the mineral name for silicon carbide: moissanite [52]. Around the same time, Acheson patented a method for making carborundum on an industrial scale, now called the Acheson process.

In 1955, a different crystal growth method was discovered by J.A. Lely, similar to that of the Acheson process. With this method, the crystal purity and properties could, to some extent, be controlled, leading to renewed interest in SiC and its applications [2].

3.3 Crystalline forms

A brief summary of the numerous SiC crystalline forms and layer defects was previously reported elsewhere [53] by the author of this document, however a brief summary is still presented here.

Silicon carbide has presented an endless array of stacking sequences with face-centred cubic (FCC) and hexagonal being the most common [54]. In 1944, N.W. Thibault proposed that cubic forms of silicon carbide be named beta-SiC (β-SiC), and that the hexagonal varieties that occur be grouped as alpha-SiC (α-SiC). Some objections to this nomenclature arose due to its failure to conform to phase diagram practice. The nomenclature, however, has proved quite convenient and is still used today [55].

A more specific nomenclature describing the crystalline structures is given in the form XY, where X is the number of layers before the sequence repeats itself, and Y describes the structure of the crystal, with C for cubic, H for hexagonal, and R for rhombohedral. An example is presented in Figure 3.1, with the only cubic SiC polytype as 3C-SiC, which has the stacking sequence ABCABC… [2].
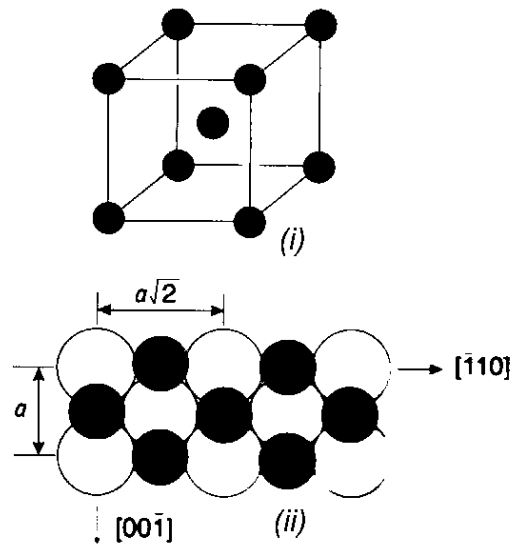
Figure 3.1: i) BCC unit cell and ii) stacking sequence [56].

The simplest hexagonal structure that can be built is 2H, shown in Figure 3.2, which has a stacking sequence of ABAB…
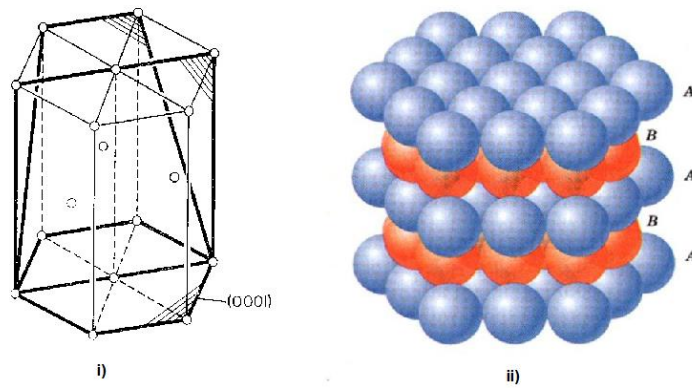
Figure 3.2: i) Hexagonal unit cell and ii) stacking sequence [56].

3.4 SiC Layer Defects

Two major defects, referred to as micropipes and stacking faults, create significant problems and debate. Three main processes have been shown to lead to the formation of micropipes, the first being the bunching together of numerous screw dislocations to form a single large screw-dislocation. At this point, it becomes energetically favourable to create a hollow core in the centre of the structure. The second and third modes of micropipe formation are through vacancy condensation at a helical dislocation and through system contamination, where particles are trapped in the growing crystal [2]. Stacking faults are formed when the stacking sequences are disturbed, illustrated in Figure 3.3, resulting in degradation of bipolar devices [2].
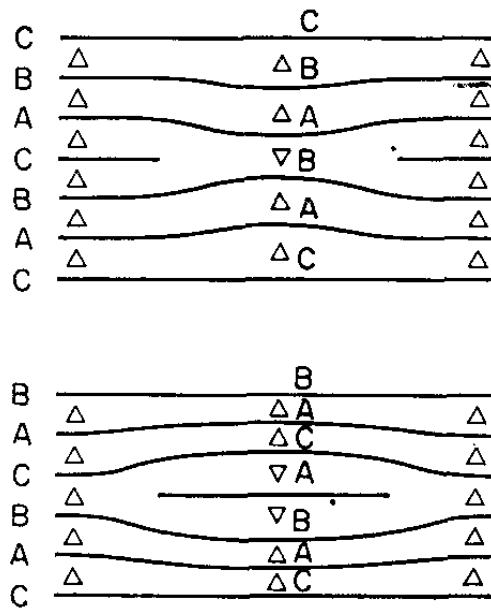
Figure 3.3: Stacking faults [56].

3.5 Commercial production of SiC

3.5.1 Acheson Process

Most SiC powder is currently manufactured using the Acheson process. The resultant powder consists of large particle sizes and mostly α-SiC due to the very high temperature regimes (between 1 600 °C and 2 500 °C). The reaction used during the Acheson process is given in Equation (3.1) as:

$$SiO_2 + 3C \rightarrow SiC + 2CO \tag{3.1}$$

The furnace dimensions are often up to 25 m long, 4 m wide and 4 m high, producing SiC crystals which are subsequently milled and purified to obtain a commercial-grade SiC powder [52]. The powder often undergoes different sintering mechanisms to produce different SiC materials for different applications [57]. The Acheson process occasionally includes sawdust and salt in lesser amounts, creating channels that help impurities escape and free chorine to react with metal impurities that become volatile [2]. Most commercially available SiC is manufactured from a mixture of silica, sand and some form of carbon with a low ash content. The reaction is energy-intensive, and only initiates above 1 500 °C [55]. Primary SiC formed under conditions above 1 200 °C is always β-SiC which is stable up to 2 100 °C and begins to transform monotropically to α-SiC slowly at 1 800 °C. It changes to the alpha structure rapidly and completely at 2 400 °C. The percentage of β-SiC converted to α-SiC is usually in the order of 5 % [55]. Even though these reported temperatures and conversions tend to vary in the literature, a typical Si-C phase diagram is shown in Figure 3.4 [58], indicating the silicon-rich and carbon-rich deposition regimes. These phase diagrams generally do not consider the precursor composition, deposition pressure, or hydrogen content.

36
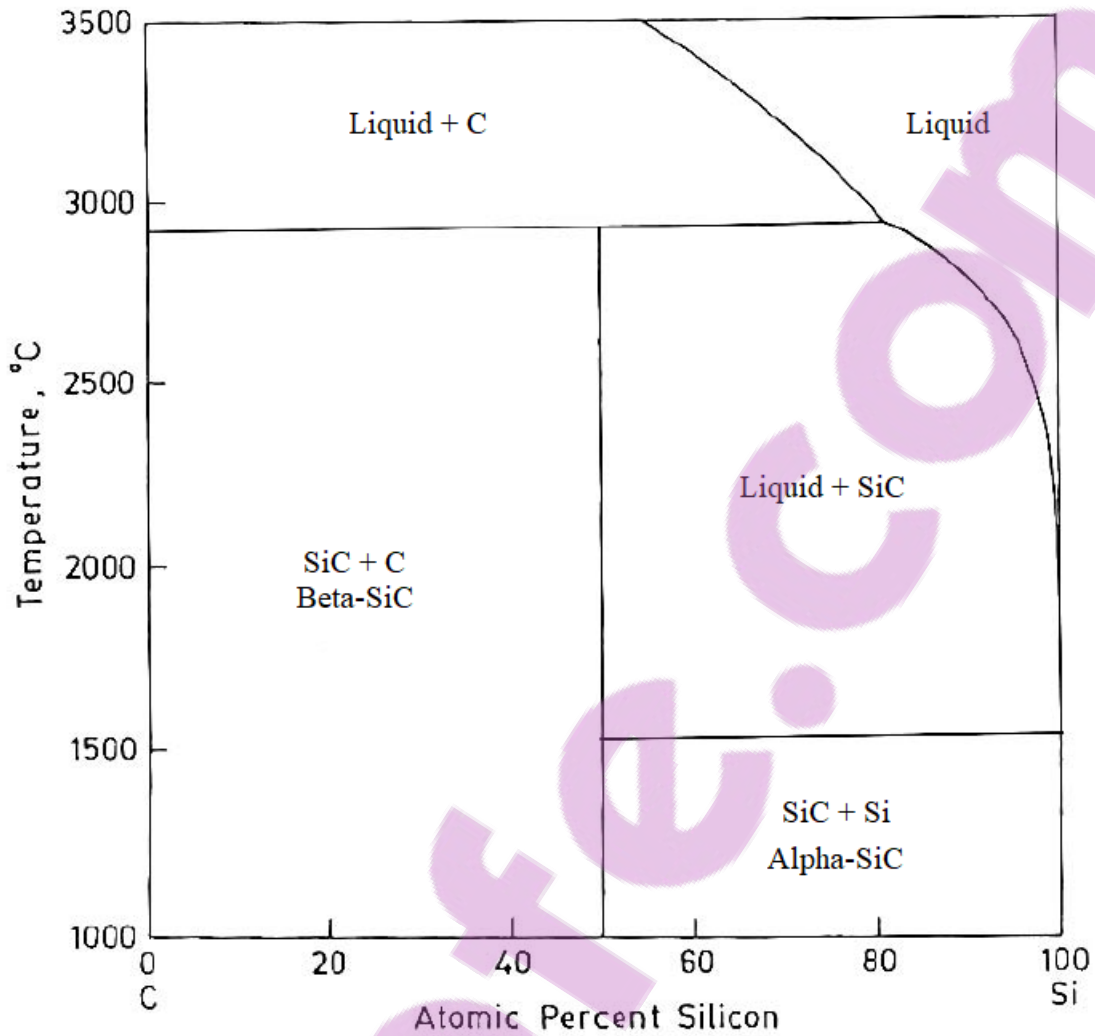
Figure 3.4: The Si-C phase diagram [58].

3.5.2 Sublimation growth

During the late 1970s, the seeded sublimation growth method was reported by Tairov and Tsvetkov [1]. Unlike the Acheson process, which operates under uniform temperatures, this method introduced material transport through the use of a thermal gradient. Application of this method enabled increased growth rates and allowed seeds of larger diameters and lengths to be produced. The technique is in most instances used today to manufacture SiC wafers. Typical parameters that affect crystal growth rate and quality are

seed temperature, source temperature, temperature gradient between seed and source, and ambient pressure [1].

3.5.3 Epitaxial growth

Epitaxial growth is achieved by modifying the sublimation method by having the source and substrate separated by a small gap of approximately 1 mm. The growth is carried out close to equilibrium in this arrangement. The substrate is thermally etched before sublimation begins. This makes it possible to grow, at low rates, thin homo-epitaxial layers on 6H and 4H with residual impurity concentration. This method is used mainly for device fabrication [2].

3.6 Physical properties

Silicon carbide is widely used as an abrasive in grinding, cutting and polishing glasses and sharpening stones. It is also used in the manufacture of porcelain, refractory brick, furnace linings and emery paper. The compound is also used in semiconductor technology [59]. Some of the physical properties of SiC are summarised in the following section.

3.6.1 Density

Experimental measurements place the density of SiC in the range of 3.166 g/cm^3 to 3.249 g/cm^3, depending on the polytype. Most of these measurements were obtained using X-ray data and calculating the density, ρ, using Equation (3.2).

$$\rho = \frac{4MW_{SiC}}{NV} \tag{3.2}$$

Here, MW_{SiC} is the molecular weight of SiC, V is the volume of the unit cell (i.e. the cube of the lattice parameter for 3C), N is Avogadro's constant and 4 is the number of formula

units in the cell. Table 3.1 gives density values for different polytypes near room temperature [1].

Table 3.1: Densities for different crystalline forms of SiC.

Polytype	Density (g/cm^3)	Temperature (K)
2H	3.214	293
3C	3.166 – 3.210	300
6H	3.211 – 3.24878	300

3.6.2 Lattice parameters of SiC

The X-ray diffraction technique is the most commonly used method to determine the lattice parameters for SiC. Table 3.2 gives the values at near room temperature for different crystalline structures [1].

39

Table 3.2: Lattice parameters for SiC polytypes.

Polytype	Lattice Parameter (Å)	Temperature (K)
3C	$a = 4.3596$	297
2H	$a = 3.0763$	300
	$c = 5.0480$	
4H	$a = 3.0730$	300
	$c = 10.053$	
6H	$a = 3.0806$	297
	$c = 15.1173$	
15R	$a = 12.691$	300
	$\alpha = 13°54'$	
21R	$a = 17.683$	300
	$\alpha = 9°58'$	
33R	$a = 27.704$	300
	$\alpha = 6°21'$	

3.6.3 Thermal conductivity

Silicon carbide is an attractive semiconductor material with highly suitable properties for high-power, high-frequency and high-temperature applications. The actual value of the thermal conductivity can vary with polytype [2]. Some typical values at room temperature are given in Table 3.3.

Table 3.3: Thermal conductivity of SiC at room temperature [1].

Polytype	Thermal Conductivity $(W.m^{-1}K^{-1})$
3C	32
4H	37
6H	36
6H ($N_{Al} = 5 \times 10^{19}$ cm^{-3} at 300 K)	23.1

The values of thermal conductivity, k_T, typically follow a trend in the form of Equation (3.3) [1].

$$k_T = AT^{-C} \tag{3.3}$$

where A and C are constants and T is temperature.

3.6.4 Physical properties of SiC polytypes

Descriptions of the physical properties of bulk SiC can easily be found in the literature [1, 2, 60, 61]. The various crystalline forms, however, differ in their physical properties by

varying degrees, depending on the specific polytype. These values are scattered in the literature, but are easily obtained in literature reviews [62-64], and are summarised in Table 3.4.

Table 3.4: Physical properties of SiC polytypes [62].

Property	Polytype			
	3C	2H	4H	6H
Hexagonality (%)	0	100	50	33
Stacking order	ABC	AB	ABCB	ABCACB
Lattice constant a (nm)	0.43589 to 0.43596	0.30753 to 0.3081	0.3070 to 0.3081	0.3073 to 0.3081
ρ (g/cm^3)	3.215	3.219	3.215	3.212

3.7   Methyltrichlorosilane

SiC mostly occurs as a single compound with an equal number of silicon and carbon atoms. The use of methyltrichlorosilane (CH_3SiCl_3), also known as MTS, consequently has the advantageous Si:C ratio of 1:1, and serves as a single-component source for the SiC product. MTS is usually diluted with a carrier gas such as hydrogen, although the pyrolytic decomposition of MTS can result in the breaking of the Si-C bonds resulting in the formation and deposition of carbon-rich [65] or silicon-rich deposits [66-68]. The deposition of these additional substances can be avoided under controlled conditions, such as the addition of nitrogen to remove free silicon [69]. Deng *et al.* [70] showed that a total

of 226 species could theoretically be involved in the CVD preparation of SiC from MTS/H$_2$ mixtures, and examined the equilibrium concentration distribution of the system. Their calculations indicated that the optimal deposition temperature for β-SiC is 1 480 K, as the deposition of graphite is minimal at this temperature. It was also implied that some species, such as SiCl$_3$H, C$_2$H$_2$, SiC$_2$ and Si$_2$C, play important roles in the mechanisms of the reactions, and that $CH_3SiCl_3 \rightarrow CH_3 + SiCl_3$ could be a favourable decomposition reaction. Their work also predicted that carbon deposition can be reduced with increasing H$_2$:MTS ratios. Similar work by Wang *et al.* [7] predicted that the predominant initial decomposition reaction is given by Equation (3.4), as a chlorine radical attacks a hydrogen atom on the MTS molecule.

$$CH_3SiCl_3 + Cl \rightarrow CH_2SiCl_3 + HCl \tag{3.4}$$

Experimental investigations undertaken by Papasouliotis & Sotirchos [6] in a hot-walled cylindrical reactor, at temperatures from 573 K to 1 273 K, indicated that deposition rates and stoichiometry varied markedly with the distance from the reactor entrance (residence time). The combined dependence of the deposition rate on temperature and distance in the reactor proved to be more complex, passing through one or two maxima along the reactor length. This was concluded to be due to the compositional changes in the gas phase with increasing residence time, with silicon-rich deposits favoured at low residence times and low temperatures. It was also found that an increase in HCl concentration suppresses the deposition of silicon, but can ultimately supress the deposition of SiC as well, given high enough concentrations. This is explained thermodynamically through Equation (3.5) [71] with an activity-based equilibrium constant close to unity, which allows suppression of Si deposition with relatively low quantities of HCl.

$$SiCl_2 + H_2 \rightarrow Si + 2HCl \tag{3.5}$$

43

A proposed SiC deposition route [72], represented by Equation (3.6), has an equilibrium constant orders of magnitude larger than that of Equation (3.5), requiring much larger quantities of HCl to hinder the deposition of SiC.

$$SiCl_2 + \frac{1}{2}C_2H_4 \rightarrow SiC + 2HCl \tag{3.6}$$

Zhang *et al.* [73] investigated the effect of surface-area to volume ratio ($\frac{A_s}{V}$), temperature and residence time on the deposition of SiC. They found at low $\frac{A_s}{V}$ ratios, two deposition rate maxima were present with increasing temperature, similar to [6], followed by a constant increase in deposition rate with increasing temperature. This pattern was attributed to temperature-selective deposition of Si and SiC. High initial deposition rates of Si and its preferred deposition rate at 900 °C, likely contribute towards the first maxima, with two different processes of SiC deposition accounting for the remainder of the trend. This trend, however, can be supressed entirely by increasing the $\frac{A_s}{V}$ ratio sufficiently. The authors state that this tendency is due to a change in deposition chemistry, rather than a depletion of the gas phase.

Loumagne *et al.* [74] found that the thermal dependence of SiC deposition could be categorised into three domains, namely:

i.   T < 850 °C, where deposition is thermally activated and the kinetics are governed by chemical reactions;

ii.   850 °C < T < 950 °C, where the deposition kinetics are still controlled by chemical reactions, but indicated a lower activation energy; and

iii. T > 950 °C, where mass-transfer controls the kinetics.

These domains also influence the effect of MTS and H_2 partial-pressures, and the authors derived kinetic data for the chemically controlled domains. Sone *et al.* [8] showed experimentally that growth rates of SiC CVD from MTS are limited by surface reactions at lower temperatures, and by mass-transfer at higher temperatures, with the critical transition occurring at approximately 1 300 ℃. They concluded that the SiC growth rate is controlled by the rate of CH_3 molecules adsorbed on Si sites. Attempts at deriving rate laws and reaction constants include that of Mousavipour *et al.* [75], who proposed a series of 15 reactions resulting in CH_4, CH_3Cl, $SiCl_2$, CH_2SiCl_2 and HCl as the major products. Table 3.5 summarises some of the parametric ranges and resulting growth rates found in the literature, arranged by ascending pressure. A more comprehensive list can be found in Ref. [76]. The results are scattered, indicating the complex mechanisms involved in SiC deposition.

Table 3.5: Summary of parametric ranges and growth rates in the literature.

Source	Temperature (K)	Pressure (kPa)	H_2:MTS	Growth Rates
Mousavipour *et al.* [75]	825 - 977	1.33 - 16	-	Kinetics only
Deng *et al.* [70]	300 - 2000	6	4:1.4	Equilibrium compositions only
Chin *et al.* [65]	1423 - 1873	8.7 – 66.7	0.3 to 40	25 – 720 µm/h
Reznik *et al.* [66]	1173 - 1373	90	1:4	0 – 130 mg/h
Zhang *et al.* [67, 73]	1073 - 1373	100	4:1	0 – 120 mg/h
Papasouliotis *et al.* [6]	573 - 1273	101.3	7-20	0 – 141 mg/min
Sone *et al.* [8]	1450 - 1650	101.3	-	0.01 – 4 µm/h
Federer [77]	1498 - 2048	101.3	45:1 to 5:1	0.21 – 4.01 µm/min

3.8   Microwave synthesis

SiC can be produced through the direct solid-state reaction of its constituents (Si and C) in a microwave field. This method does not utilise plasma chemistry, only microwave heating. Satapathy *et al.* [13] determined the optimum parameters for the SiC phase formation in a 2.45 GHz microwave field. In less than five minutes phase-pure SiC was formed at temperatures up to 1 300 °C, yielding sub-micron-sized SiC particles, shown in Figure 3.5 [13].
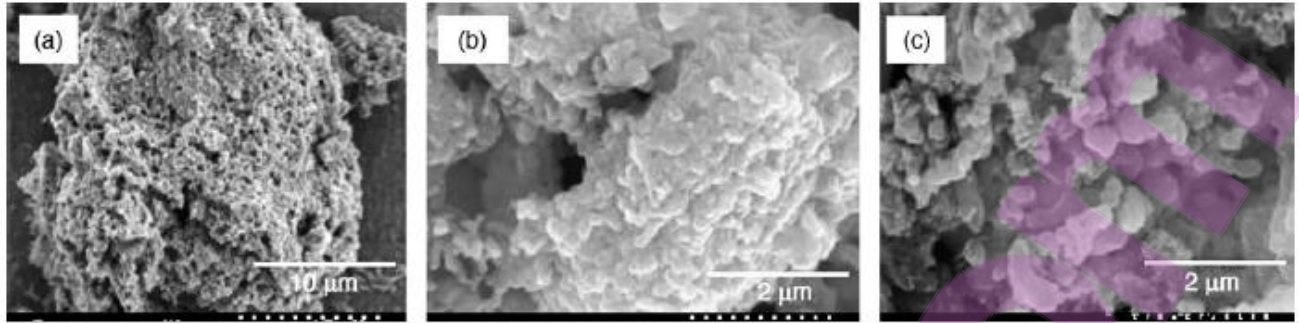
Figure 3.5: SEM micrographs of β-SiC powders synthesised using a 2.45 GHz microwave field [13].

Similarly, Moshtaghioun *et al.* [14] reported the synthesis of SiC nanopowders using carbothermic reduction of a silica precursor in a 2.45 GHz microwave field. β-SiC was produced at 1 200 °C after five minutes of microwave exposure, yielding particle sizes from 10 nm to 40 nm [14], shown in Figure 3.6.
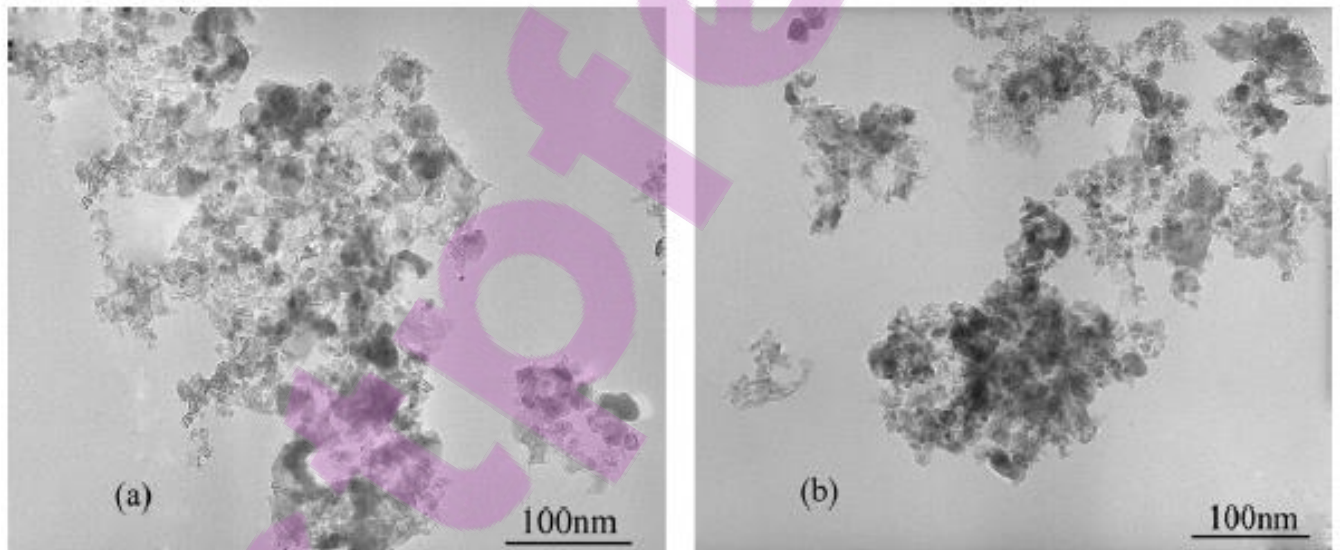
Figure 3.6: TEM micrographs of β-SiC particles after carbothermic reduction of silica in a microwave field [14].

3.9 Thermal vs. Plasma Enabled CVD of SiC

3.9.1 Chemical vapour deposition

Amorphous SiC powders have been produced by Kavecky *et al.* [78] through the chemical vapour deposition (CVD) of a reaction mixture consisting of SiH_4 and C_2H_2 in a vertical tubular flow-reactor operating between 900 °C and 1 250 °C. The resulting powders were characterised by particle sizes ranging from 100 nm to 200 nm and agglomerate sizes below 300 nm [78], shown in Figure 3.7.
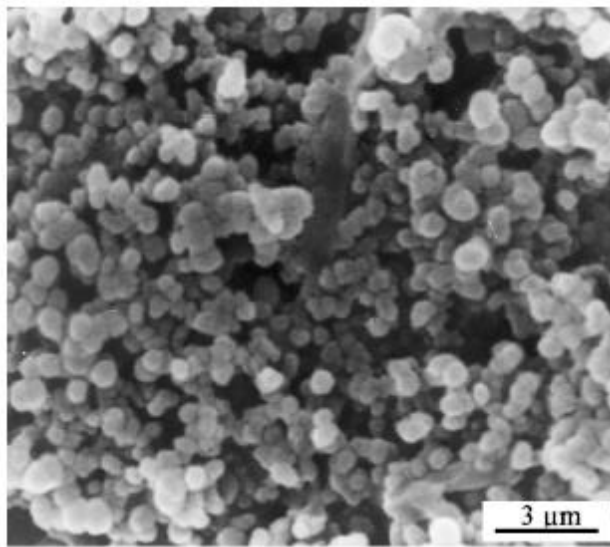
Figure 3.7: Micrograph of SiC obtained through CVD [78].

Even smaller particle sizes were obtained by Li *et al.* [79], at temperatures between 850 °C and 900 °C from liquid carbosilanes. Particle sizes ranged between 50 nm and 70 nm and are shown in Figure 3.8.
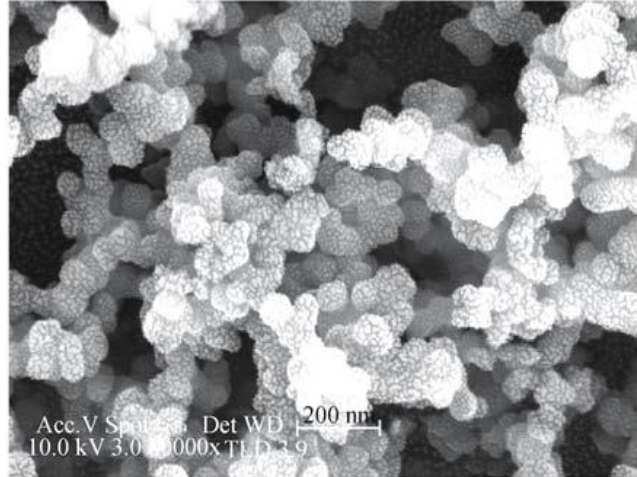
Figure 3.8: SEM micrograph of SiC nanoparticles from CVD of liquid carbosilanes [79].

Structural investigations have been undertaken by Neuhäuser *et al.* [68] who deposited silicon-rich SiC layers. They found that H_2:MTS ratios greater than 3 yielded silicon-rich layers, which also affected the colour and morphology of the layers. Chin *et al.* [65] used induction-heated substrates in a quartz tube vacuum system to investigate the structure of chemical vapour deposited SiC. Substrate temperature, chamber pressure and gas composition were found to influence the morphology of the layers, and the authors produced a phase diagram representative of the changing morphology-process relationships. Deposits at low temperatures, moderate pressures and low H_2:MTS ratios were found to be fine grained. At very high temperatures and H_2:MTS ratios, large single crystals were observed. The authors also reported that high H_2:MTS ratios, high pressures and low temperatures yielded silicon-rich deposits, whereas low pressures, low H_2:MTS ratios and high temperatures yielded carbon-rich deposits.

3.9.2   SiC Coating in Fluidised Beds

SiC forms an integral part of the TRISO-coated fuel particle, and is often deposited in fluidised bed configurations. Federer [77] found that the optimum temperature range for SiC deposition in a fluidised bed, using MTS as precursor, was 1 475 – 1 675 °C, and

H$_2$:MTS ratios > 20. In a pyrolytic deposition process for applying a multi-layer coating to a kernel of nuclear fuel, Graham *et al.* [80] used a fluidised bed consisting of 150-grain batch of UO$_2$ kernels with diameters approximately 800 μm. A preferred coating temperature for the multi-layer coating was set at 1 630 °C and suitably structured pyrolytic carbon was laid down at a temperature within 50 °C of the deposition temperature of SiC to minimise thermal stress formation. The multi-layer coating technology was also applied in the Pebble Bed Modular Reactor (PBMR) project, which utilised SiC and pyrolytic carbon-coated particles of enriched UO$_2$ encased in graphite to form a fuel sphere, or pebble, resembling a tennis ball [81]. Initially, during the fuel fabrication process, small beads of enriched UO$_2$ undergo a gelling and calcification process to produce uranium-fuel kernels. These kernels are subsequently placed in a fluidised bed CVD reactor, conventionally using an argon environment at a temperature of over 1 000 °C. For the PBMR fuel particles, the first deposited layer was a porous carbon layer, which accommodates for any mechanical deformation that the UO$_2$ may have undergone during the lifetime of the fuel. This layer was followed by a thin coating of pyrolytic carbon, followed by a layer of SiC, followed by an additional layer of pyrolytic carbon. These three layers acted as an impenetrable barrier for the immobilisation of radioactive decay products [81]. The final particles were each approximately 1 mm in diameter, and 15 000 of these fuel particles were then mixed with a graphite phenol powder and pressed into larger spheres approximately 60 mm in diameter. An additional layer of high-purity carbon was then added to form a "non-fuel" zone, and the resulting spheres were pressed, sintered and annealed to enhance hardness and durability [81]. The multi-layer spheres and fuel elements are shown in Figure 3.9 [81].
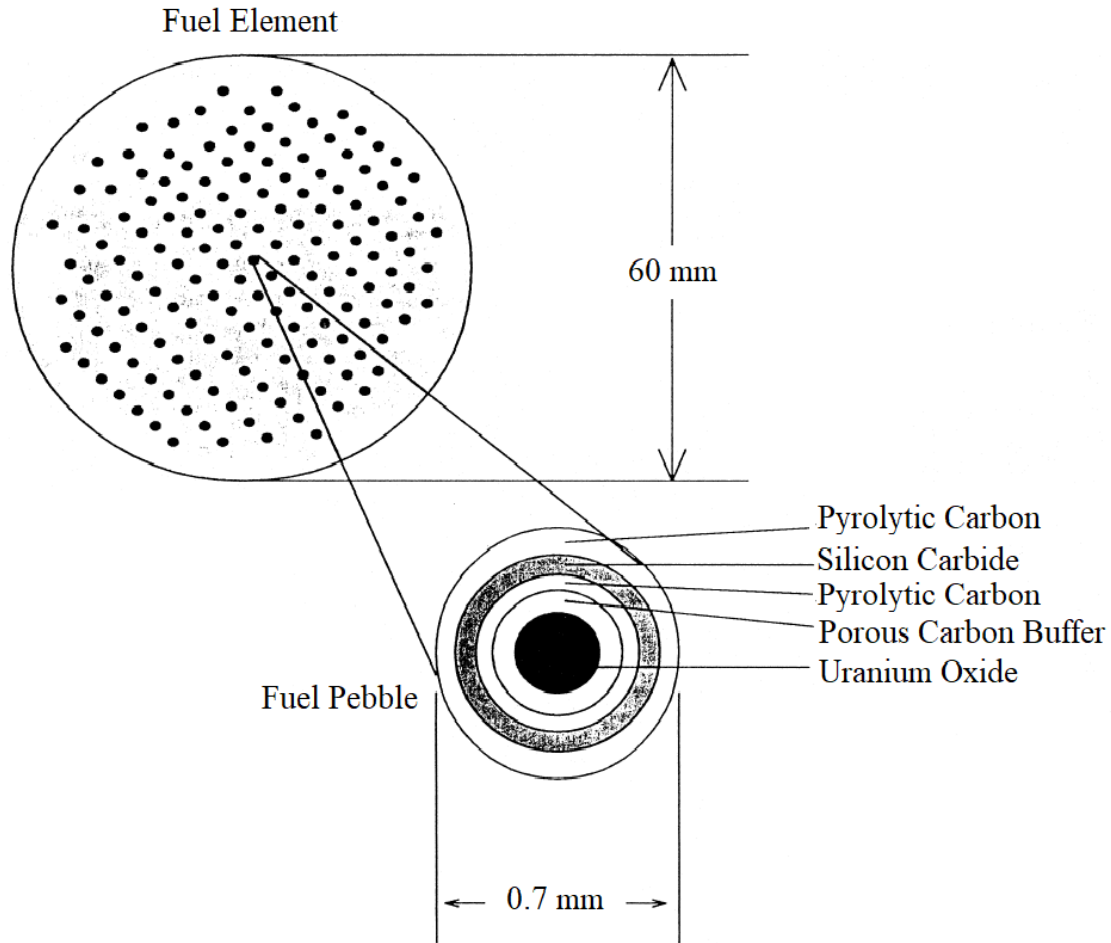
Figure 3.9: Multi-layer spheres used in PBMR fuel elements.

3.9.3 Plasma Spraying

Plasma spraying is part of thermal spraying, a group of processes in which finely-divided metallic and non-metallic materials are deposited in a molten or semi-molten state on a prepared substrate. The thermal plasma heat source (DC or RF discharges), with temperatures over 8 000 K at atmospheric pressure, allows for the melting of most materials. Powdered materials are injected in the plasma (RF discharges) or the plasma jet (DC arcs), where particles are formed, accelerated and melted, or partially melted, before they flatten and solidify onto the substrate (forming lamellae or splats) [82]. Figure 3.10 represents the basic concepts behind the technology.
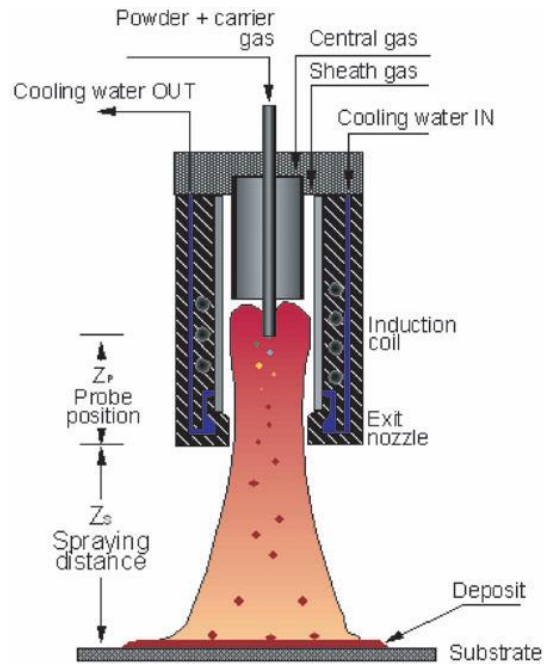
Figure 3.10: Plasma spray technology [82].

A group of researchers at the University of Alabama have shown that, if using SiO_2 and CH_4 as starting materials, SiC can be synthesised by plasma spraying. This results in SiC powders with average sizes of less than 100 nm, along with fibre-like microstructures [83]. The SiC is formed through the reaction shown in Equation (3.7).

$$SiO_2 \ + \ CH_4 \ \rightarrow \ SiC \ + \ 2H_2O \tag{3.7}$$

3.9.4 Arc plasma

Ishizaki *et al.* [84] reported a direct method for the production of carbide powders using the arc plasma method with methane as precursor. They produced SiC, titanium carbide (TiC) and tungsten carbide (WC) powders with particle sizes ranging from 20 nm to 40 nm [84]. Inoue *et al.* [85] also produced SiC powders using arc-plasma irradiation, with methane and silicon as precursors, yielding particles with sizes between 20 nm and 40 nm

[85]. Using silica and CH_4, Taylor and Pirzada [86] produced ultrafine SiC powders using a non-transferred arc thermal-plasma reactor.

3.9.5 Inductively coupled plasmas

Inductively-coupled plasmas (ICPs) are also capable of producing submicron-sized SiC powders. Hollabaugh *et al.* [87] developed a radio-frequency (RF) plasma system that made use of an induction coil, and was then utilised for the production of ultrafine and ultrapure SiC powders. The resulting sizes ranged from 10 nm to 20 nm, shown in Figure 3.11.
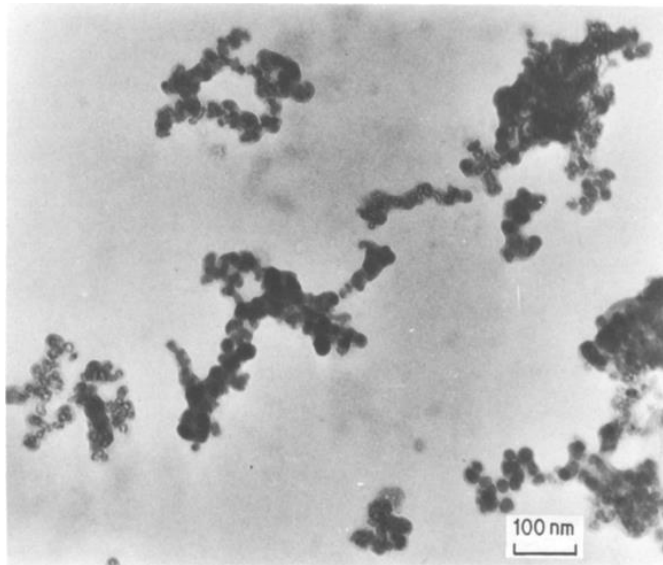
Figure 3.11: SiC nanoparticles produced through an ICP system [87].

Guo *et al.* [88] reported on the formation of SiC powders through the reaction of elemental silicon and CH_4 in an induction plasma. The resulting powder consisted of a mixture of α- and β-SiC, with sizes ranging from 40 nm to 60 nm. It was also found that the plasma gas composition had an influence on the proportions of crystalline phases [88]. A TEM micrograph of the resulting powders is shown in Figure 3.12.
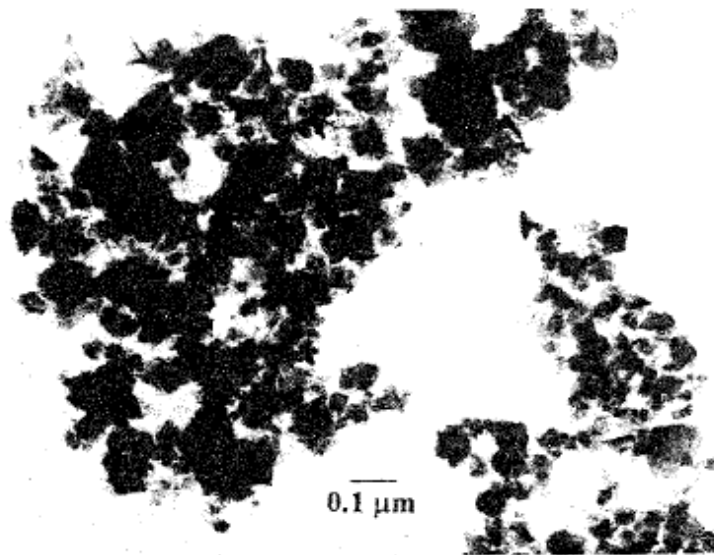
Figure 3.12: A TEM micrograph of SiC produced in an induction plasma [88].

Other examples of SiC powders produced from ICPs include Leconte *et al.* [89], who demonstrated how the use of ICPs allows for the production of large amounts of SiC nanopowders from bulk SiC powders, as well as Ko *et al.* [18], who used other organic precursors in RF inductively coupled plasmas to synthesise SiC nanopowders.

3.9.6 Direct-current plasma system

Nano-sized SiC powders have been prepared using direct-current (DC) plasma systems. Zhu *et al.* [90] published a paper on the synthesis of SiC nanopowders in a 15 kW DC plasma reactor and either silicon tetrachloride ($SiCl_4$) or MTS as precursor. The resulting particles were characterised by sizes ranging from 15 nm to 60 nm [90]. Similarly, Oh *et al.* [91] produced SiC using a DC plasma torch and $SiCl_4$ with CH_4. The resulting powder was characterised to be β-SiC, with small amounts of α-SiC and free carbon present in the powder. The average size of the particles was estimated to be less than 100 nm [91], shown in Figure 3.13.
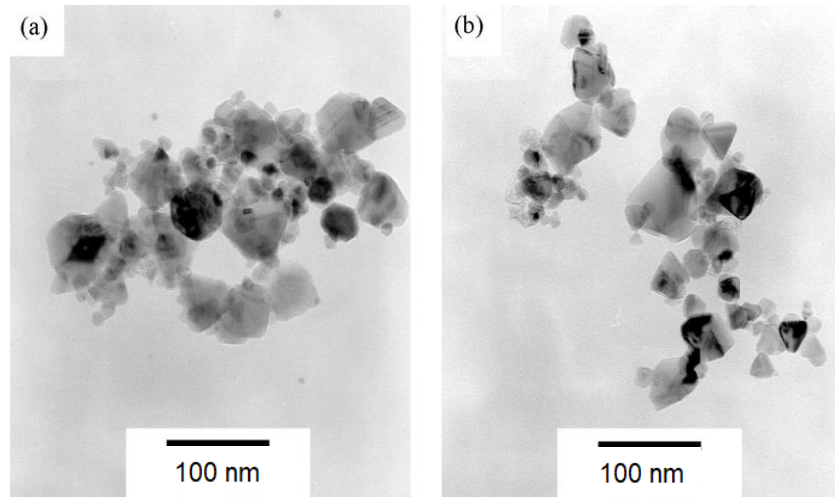
Figure 3.13: TEM micrographs of SiC produced through a DC plasma system [91].

3.10 SiC as a nuclear ceramic

A major concern for any ceramic component within the vicinity of an energetic radiation source, is the effect of radiation damage. A single alpha decay can result in ~ 1 200 atomic displacements within the crystalline lattice, significantly affecting the structure and properties of the ceramic, and inducing defects and voids [92]. Additionally, the generation of dislocations, along with the build-up of helium atoms, may lead to swelling of the ceramic, resulting in increased internal stresses and cracking [93] . This is also of concern with regards to the immobilisation of radioactive waste, where one management strategy involves the chemical immobilisation of the radio nuclides into the structure of a stable solid (often a ceramic). This immobilisation strategy is also implemented in composite fuels, which consist of a fissile phase dispersed in an inert non-fuel matrix, designed for high-temperature applications. An example of such a composite fuel is the tri-structural isotropic (TRISO) coated fuel particle. These particles are utilised in pebble-bed high-temperature reactors (HTRs), and are envisaged for Generation IV HTRs [92]. In these TRISO particles, the actinide fuel is distributed in thousands of small spherical particles [94]. Kernels are coated by CVD in a fluidised bed using MTS and hydrogen gas. An

interstitial layer consisting of SiC is deposited, which acts as the main barrier for fission product diffusion, effectively acting as a small, load-bearing pressure vessel [92].

SiC-fibre-reinforced/SiC (SiC/SiC) composites are also of interest in fission and fusion applications due their ability to retain high strength at temperatures greater than 1 500 °C in oxidising environments. In addition to their damage tolerance, SiC/SiC composites exhibit stabilising behaviour under irradiated conditions, high concentration of defects acting as sinks for migrating defects, and an inherently low activation -and decay heat [92]. Every rose has its thorns, however, as these SiC/SiC composites come with a number of challenges such as their thermal conductivity, gaseous transmutation rates, hermetic behaviour and joining technology [95]. For loss-of-coolant accidents (LOCA), the hydrothermal corrosion and steam oxidation of SiC become important factors and are currently under investigation [96].

As discussed in Section 3.7, low-temperature CVD deposits of SiC are often accompanied by the presence of free silicon. These silicon-rich layers are characterised by inferior high-temperature strength and creep properties, higher permeability to metallic fission products, and are subject to recrystallisation under high-temperature conditions, inducing pore generation [76]. Additionally, the formation of different isotopes of Si in the SiC crystal structure due to irradiation, affects the integrity of the SiC layer. Absorption of a thermal neutron by the ^{31}Si isotope leads to the formation of ^{31}P through beta-decay. The resulting phosphorous within the SiC matrix makes the material brittle and undesirable [76, 97]. With regards to grain sizes, it is expected that nanocrystalline materials will have a significant impact on the radiation resistance, attributed to the migration of defects to the grain boundary sinks [98, 99]. Some irradiation results of fine-grained (< 100 nm) SiC hinted at an improvement in radiation resistance [100]. It is therefore important to obtain a stoichiometrically ideal, nanocrystalline SiC deposit for use in nuclear applications.

3.11 Summary

The history of SiC's discovery and application indicates it is a relatively young material, with various applications in electronics, abrasives and nuclear-based industries due to its ideal physical properties. When SiC is deposited as a layer/coating, the resultant properties and polytypes vary depending on the deposition pressure, temperature and hydrogen concentration. The dependence on these parameters has prompted numerous studies within the literature focussed at optimisation of the layer quality for specific purposes. Different synthesis and deposition techniques are under investigation, including numerous plasma-enabled CVD methods. Conventional SiC coatings, however, are deposited using fluidised bed technology, e.g. the fuel fabrication process used during the PBMR project. Nuclear applications of SiC require stoichiometrically ideal, nanocrystalline SiC deposits, as silicon-rich deposits have detrimental effects on the layer integrity.

CHAPTER IV:
SPOUTED BED REACTOR DESIGN, OPERATION & MODELLING

4 Spouted Beds Reactor Design, Operation & Modelling

4.1 Introduction

This chapter focuses on the design considerations and applications of spouted bed technologies and concludes with a short overview of spouted bed coating technology, narrowing the field to plasma-assisted spouted bed reactors. Section 4.2 provides a brief introduction to the physical processes involved with spouted beds, as well as the requirements to be met to enable and maintain the spouting action. This is followed by the cone and inlet design considerations for optimal spouting conditions in Section 4.3, and the effect of solid's properties on spouting is discussed in Section 4.4. The effects of gas flow rates and bed depth are likewise discussed in Section 4.5, followed by a few examples of industrial applications in Section 4.6. The chapter concludes with a focus on microwave plasma-assisted spouted bed technologies found in the literature in Section 4.7.

4.2 Introduction to Spouted Beds

Consider a vessel filled with a bed of coarse particles and a gas inlet positioned at the bottom. If the gas injection rate is sufficiently high, the resulting high-velocity jet propels a stream of particles upwards through a newly formed hollow central core within the bed [101]. After being thrust upward above the bed level, the particles fall back onto the annular region between the vessel wall and the hollow central core. The particles then travel back downwards in this annular region, effectively forming a counter-current flow system, consisting of an upward flowing gas stream and downward flowing solid bed. This system is termed a *spouted bed* and is presented graphically in Figure 4.1[1].

---

[1] An informative CFD model of a spouted bed can be viewed at https://youtu.be/yHf6FOMiamY
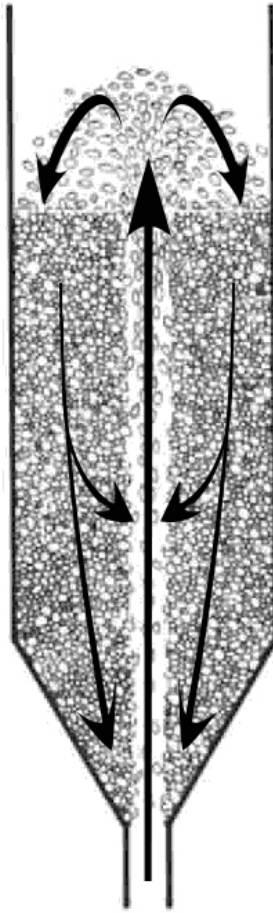
Figure 4.1: Visual representation of a spouted bed mechanic, with arrows representing the flow direction, adapted from Ref. [101].

Requirements for spouting include definite ranges of gas velocity, solid density and diameter, as well as vessel -and inlet configurations. Varying these conditions can result in transitions from a static bed configuration to that of a spouted bed, to a fluidised bed (and transitions in-between) [101]. These transitions are represented graphically using phase diagrams for specific configurations, an example of which is given in Figure 4.2 for wheat. These phase diagrams indicate that, for a given solid-gas and vessel configuration, there exists a maximum spoutable bed depth, H_m, beyond which the spouting action is replaced by poor fluidisation (bubbling or slugging).
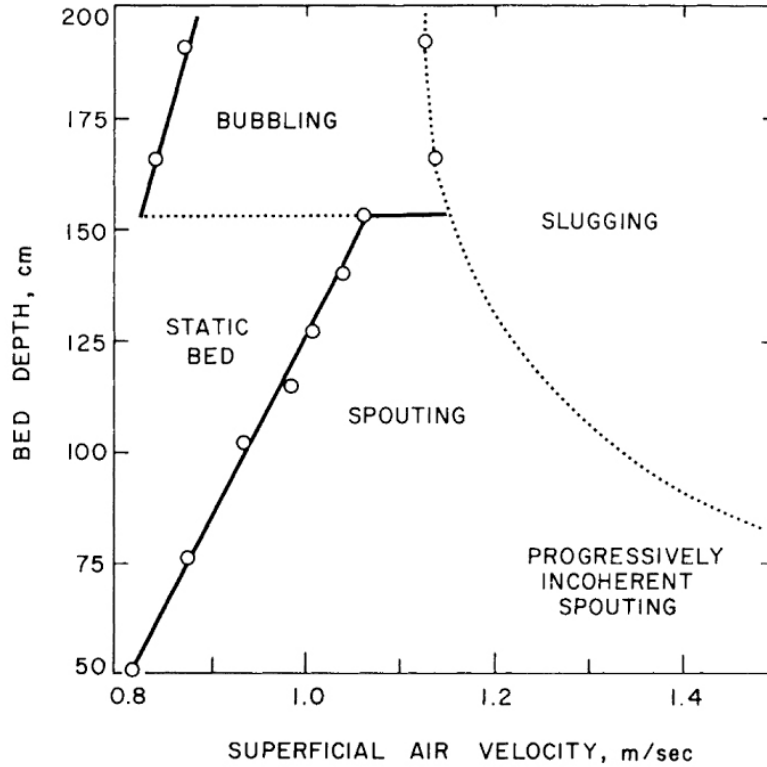
Figure 4.2: Phase diagram for wheat, with d_p = 3.2 mm to 6.4 mm, D_c = 15.2 cm, and D_i = 1.25 cm [102].

Fluidised beds differ from spouted beds in that fluidisation involves the passage of gas through part of the bed without inducing much movement, whereas a spouted bed requires agitation of the entire bed. This is brought about through the gas jet which enables intimate contact between the particles and the gas. Spouting actions also usually require particle diameter, d_p > 1 mm, below which fluidisation becomes dominant. The total frictional pressure drop, ΔP_s, across a spouting bed is also approximately 20 % lower than that of a fluidised bed [101].

An additional requirement for the spouting action is the minimum spouting velocity, U_{ms}, required to maintain the spouted state, and is dependent on the bed geometry as well as the solid and fluid properties. Various correlations exist to predict U_{ms} for various bed

configurations, an example is given by the Mathur-Gishler equation [102] in Equation (4.1).

$$U_{ms} = \left(\frac{d_p}{D_c}\right)\left(\frac{D_i}{D_c}\right)^{\frac{1}{3}}\left(\frac{2gH\left(\rho_s - \rho_f\right)}{\rho_f}\right)^{\frac{1}{2}} \tag{4.1}$$

Here, d_p is particle diameter, D_c is the column diameter, D_i is the inlet diameter, g is the gravitational acceleration, H is the bed height. ρ_s is the solid density, and ρ_f is the fluid density.

4.3 Cone and Inlet Design

The conical section at the bottom of the vessel, facilitates the flow of the solid particles from the annulus into the gas jet. This avoids a stagnant region in the lower corners of the vessel should a flat base be used. For the case of a very steep conical angle, spouting becomes unstable as the entire bed tends to be lifted by the gas stream. The solid's properties appears to affect the precise cone angle needed for effective spouting, however for most materials the ideal conical angle is prescribed at approximately 40° [103, 104]. The inlet design also affects H_m as well as the stability of the spout. Some designs include a constricting orifice at the narrow end of the cone, or a pipe protruding a short distance above the inlet surface [105]. These design concepts are shown in Figure 4.3.
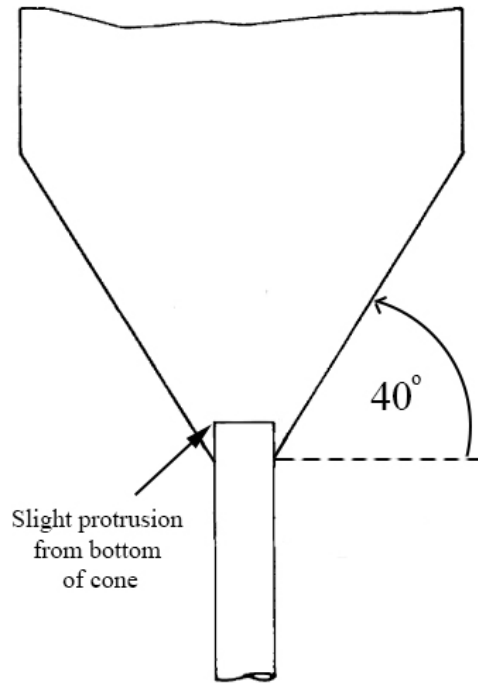
Figure 4.3: Cone and inlet design considerations.

4.4 Solids Properties

The minimum particle diameter necessary for spouting operation is generally quoted as 1 mm, however it has been shown that spouting action can be achieved for smaller sizes should the constraint be met which requires that the gas-inlet diameter not exceed 30 times the particle diameter [106], although this relation does not scale up well. Assuming all other variables constant, k, the effect of particle diameter and bed height on spouting velocity [101] can be given by:

$$U_{ms} = kd_pH^{\frac{1}{2}}$$

(4.2)

Particle size distribution favours uniformity for spouting stability, as a low permeability with wide ranges of particle sizes tend to distribute the gas flow, rather than produce the required jet action. The addition of even a small amount of fines to a uniformly sized bed can easily impair the spouting action, and the addition of larger coarse particles to a bed of finer material has similar effects [107]. It is noted, however, that the limits of the particle size distribution on the spouting action are fairly wide, with some beds still satisfactorily spouted up to an eightfold size spread and particles up to 3 cm in size [108].

The effect of particle density appears to be minimal, with various materials being spouted without any indications implying that limits exist which would prevent spouting entirely [101]. It is evident that particle shape and surface characteristics have much larger effects on the spouting stability [101]. The effects, however, prove difficult to evaluate as shape and surface characteristics are not easily defined.

4.5 Gas Flow Rate & Bed Depth

In shallow beds, where $\frac{H}{D_c} < 3$, a gas flow rate high above the minimum required flow rate for spouting results in an undefined spout shape. The movement of the solids in the region above the bed become chaotic, however, the downward motion of the particles in the annulus remains unchanged [102]. The maximum spoutable bed depth, on the other hand, is controlled by three different mechanisms causing instabilities beyond certain upper limits. These mechanisms are defined as the fluidisation of annular solids, choking of the spout and growth instabilities brought about by hydrodynamic conditions [101].

4.6 Applications

A popular application of spouted bed technology is the drying, heating and cooling of granular solids. These solids include agricultural products (e.g. wheat) [109], wood chips [110] and polymeric materials [111]. One major advantage of this drying technique is the wide temperature gap between the hot spout air and the bed, which avoids thermal damage

to the particles. Another industrial application of the spouted bed is granulation [112, 113], where millimeter-sized particles are grown from seed granules, in a layer-by-layer process. Often this is achieved by injecting a precursor liquid or gas into the bed along with the spouting gas. The advantages of this technique, compared to a fluidised or fixed bed, are generally the production of rounder, smoother, and harder granules, and avoids the problems of agglomeration of particles onto each other and the reactor walls. Other applications include energy valorisation from waste [114], tablet and particle coating [115, 116] and solids blending [117].

Of particular interest to this study is the use of spouted bed reactors for the coating of nuclear fuel particles with pyrolytic carbon and SiC. New generation HTGRs make use of TRISO coated nuclear fuel particles covered with a carbon-graphite fuel body. TRISO coatings consist of four sequentially deposited layers of pyrolytic carbon and SiC around a uranium oxide or carbide kernel, after a series of batch deposition processes. The TRISO coatings are the primary containment structure in the HTGR reactor concept and require high uniformity and structural stability [118, 119]. Using spouted bed technologies, a bed of fuel particles is spouted along with an appropriate hydrocarbon at high temperatures [120-123].

4.6.1 Plasma Spouted/Fluidised Beds

A plasma spouted bed reactor is fitted with a plasma-generating torch at the conical bottom section, and the spouting action is generated by the plasma jet itself [69, 124]. The advantage of this setup is the high temperatures attainable by the particles as they come into contact with the tail-end of the plasma. A notable disadvantage is the radiative and convective heat losses during operation. The efficiency of such a reactor is usually determined by the rates at which heat, mass and momentum are transferred based on plasma-particle interactions. Due to the high plasma-jet velocities, the particle residence times can be very short, and the resulting energy transferred to the particle can be quite low

(less than 5 %) [125]. The following methods can be adopted to improve the overall heat transfer efficiency [69]:

- Reduction in plasma jet velocity;
- increase in plasma volume;
- increase the wall temperature to reduce radiative losses; and
- improved flow patterns of solids throughout the system to improve residence times.

Plasma jet-heated reactors are favourably considered for use in coating applications due to the ultra-high temperature regimes necessary for surface deposition. Plasma spouted/fluidised beds are considered a favourable choice for bulk production of coated particles [32].

A DC plasma-spouted/fluidised bed was applied towards the granulation of spherical alloy grains from metal powder mixtures using two auxiliary injection nozzles located below the nozzle. Granulation of Fe-Al powders was found to be feasible in a laboratory-scale plasma-spouted/fluidised bed setup [126]. Circulating spout/fluidised bed reactors have proven to be an efficient option for successful operation of CVD processes to produce ultra-fine powders, as summarized by Sathiyamoorthy [32].

4.7 Microwave Plasma-enabled Spouted Bed CVD Reactors

Plasma-enabled chemical vapour deposition (PECVD) techniques are often used for the deposition of thin films at low temperatures. Karches *et al.* [30] generated a low-temperature plasma in a riser tube by coupling microwaves, represented in Figure 4.4. As a model application, NaCl crystals were coated with a thin silicon oxide film and the deposition rates were obtained up to 1 kg/min [30].

67
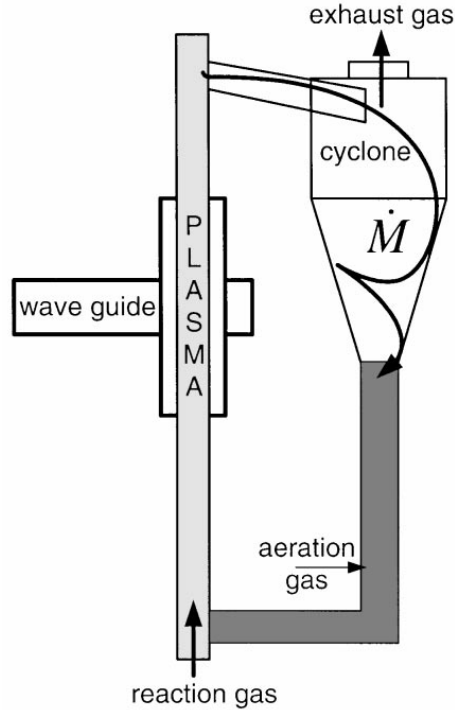
Figure 4.4: Experimental setup used by Karches *et al.* [30].

A similar setup was used by Borer and von Rohr [127] where thin SiO_x films were deposited on salt and silica gel particles by PECVD with a microwave plasma source integrated in the riser tube of a circulating fluidised bed reactor. The resulting reactor provided high deposition rates and good precursor conversion efficiency. The films deposited revealed a dense and coherent film morphology [127]. A different variation on this design is that of Tap and Porada [128] for plasma-enabled synthesis and coating of granular solid materials using a microwave plasma cavity and a CVD cavity, where microwave radiation is used to heat the granular material. It was shown that the interaction of the fluidised particles with the microwave field influences the ignition and stability of the microwave plasma to a significant degree [128]. Matsukata *et al.* [129] applied a microwave plasma as an excitation source of reactive gases, and alumina and silicon were used as bed materials. The hydrodynamic behaviour of the plasma-bubbling fluidised bed

68

was studied, and the field of plasma generation was investigated optically. It was concluded that heterogeneous CVD on the surface of particles may occur in this reactor [129].

Shin and Goodwin [31] reported diamond growth on particles in a fluidised bed reactor using MPECVD. Si and SiO_2 powders are used as seed particles without pre-treatment and good quality diamond was reported on both the Si and SiO_2 particles. Bayer *et al.* [130] presented the coating of a significant amount of particles in a fluidised bed under low-temperature plasma conditions using PECVD. The low-temperature plasma fluidised bed technique can be used for thin-film deposition (e.g. SiO_2, TiN, TiC, TiO_2 and diamond-like carbon), as well as non-coating processes (e.g. plasma cleaning, sterilization, activation, hydrophobic or hydrophilic finishing) [32].

Chung *et al.* [131] successfully applied a microwave plasma jet, combined with a spouted bed, for Ni/γ-Al_2O_3 catalyst preparation. The experimental setup, shown in Figure 4.5, consisted of a quartz glass tube (d_i = 27 mm, l = 370 mm), and a nozzle inlet (d_i = 9 mm) inclined upwardly at 60°. The plasma was generated by a microwave generator under atmospheric pressure and injected to spout the particles from the bottom of the spouted bed. A mixture of Ar and H_2 was used as the plasma gas.

A counter-current flow system, consisting of an upward flowing gas stream and downward flowing solid bed is termed a spouted bed. Requirements for spouting include definite ranges of gas velocity, solid density and diameter, as well as vessel- and inlet configurations.
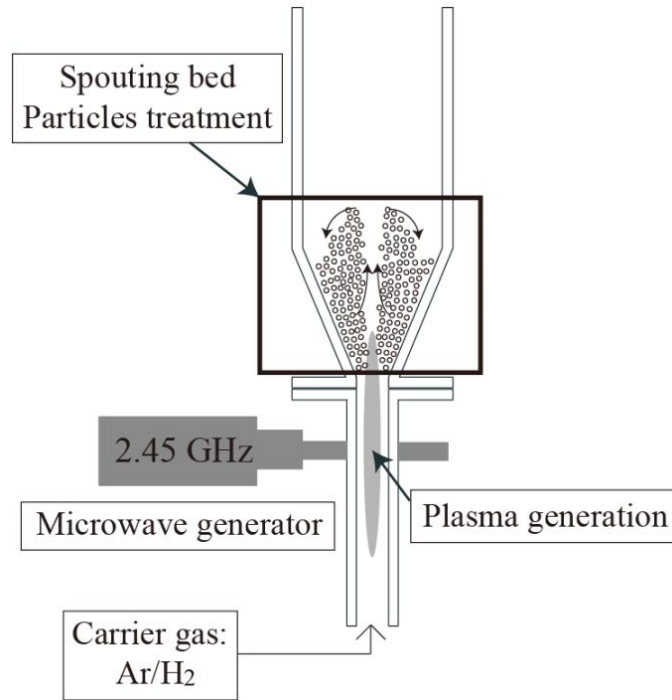
Figure 4.5: Experimental setup using a MW plasma jet for particle treatment [131].

4.8 Summary

Design requirements include cone and inlet specifications, solids' properties, gas flow rates, and bed depth. Various applications of spouted bed technologies include drying, heating and cooling of granular solids, and, of particular interest, the coating of nuclear fuel particles with pyrolytic carbon and SiC where a bed of fuel particles is spouted along with an appropriate hydrocarbon at high temperatures. Spouted beds are often combined with plasma-based coating technologies, with the added advantage of high particle temperatures. PECVD techniques are often used for the deposition of thin films at low temperatures, usually achieved through microwave discharges. Various experimental studies using microwave plasma-enabled CVD are reported, and show promising results for particle coating applications.

70

CHAPTER V: EXPERIMENTAL

5 Experimental

5.1 Introduction

In this chapter, the flow calibration-curves are first presented in Section 5.2, followed by a short description of the equipment and apparatus used during the experiment in Section 5.3. The design of experiment (DoE) is then given and described in Section 5.4, explaining why the specific DoE was chosen. The experimental method/procedure is presented point-wise in Section 5.5 and the chapter concludes with Section 5.6, with a short listing of the characterisation equipment utilised.

5.2 Calibration

The gas volumetric flow-rates through the Aalborg rotameters were calibrated using a Gilibrator® II system, and the resulting calibration curves are reported below. The flow rates were set at various values on the rotameters, and the corresponding flow rates were measured and read off the electronic Gilibrator® system. The plotted points all showed some degree of curvature. Since only interpolation between the points was used for the obtaining of the actual flow rates, a second-degree fit was used to increase the accuracy of the interpolations. The calibration curve for the argon flowing through the spout is given in Figure 5.1.
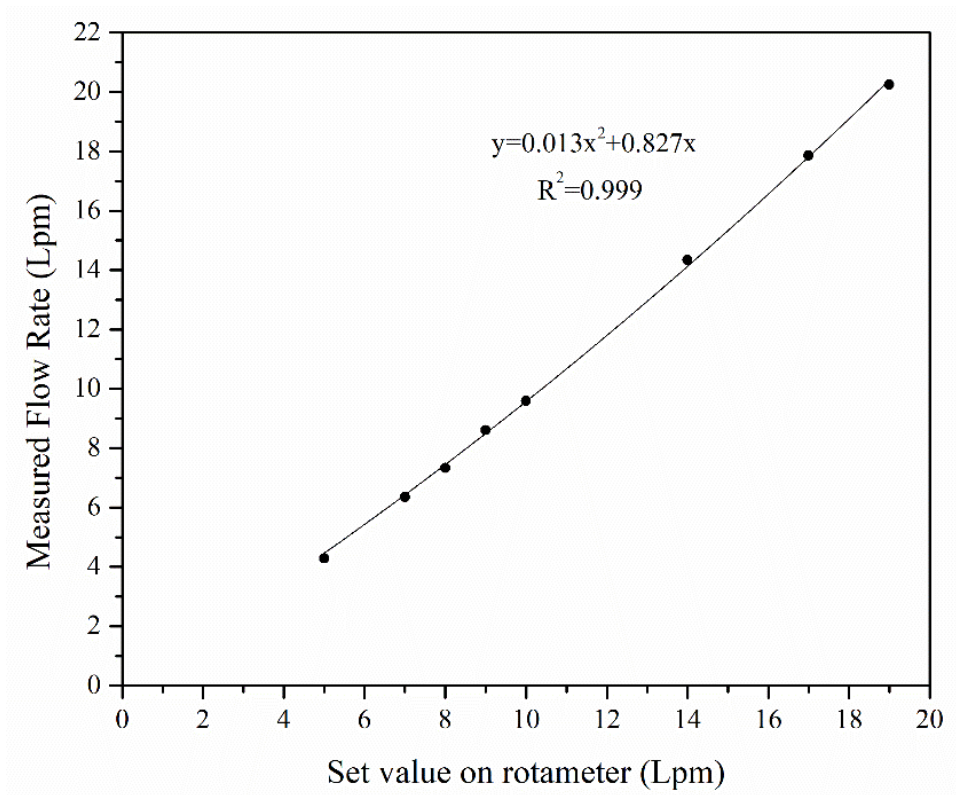
Figure 5.1: Argon calibration curve (spout).

Accordingly, the argon flow rate sweeping through the MTS container was also calibrated, as well as the hydrogen flow rate, and the resulting curves are given in Figure 5.2 and Figure 5.3.
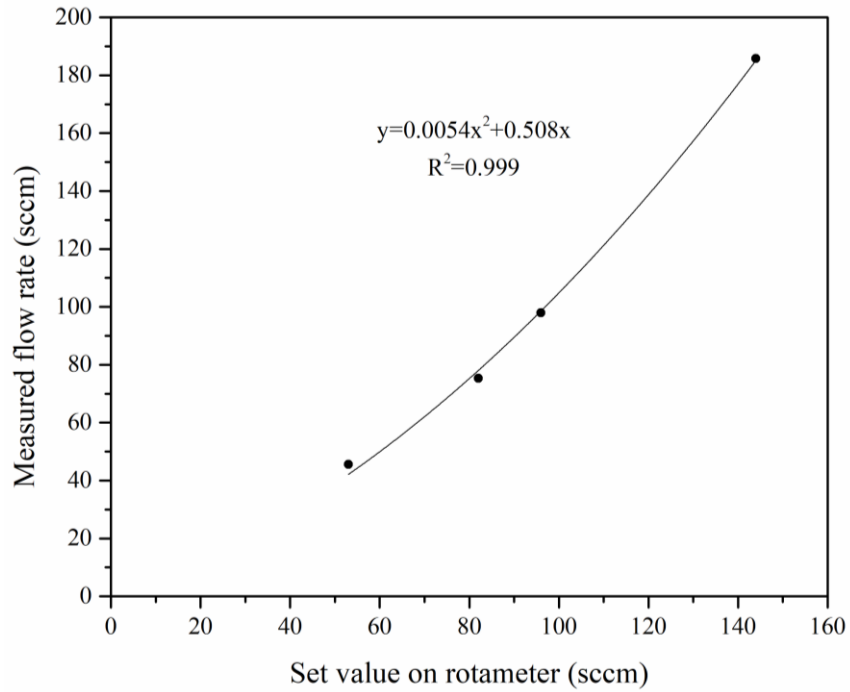
Figure 5.2: Calibration curve for the argon flow rate through the MTS container.
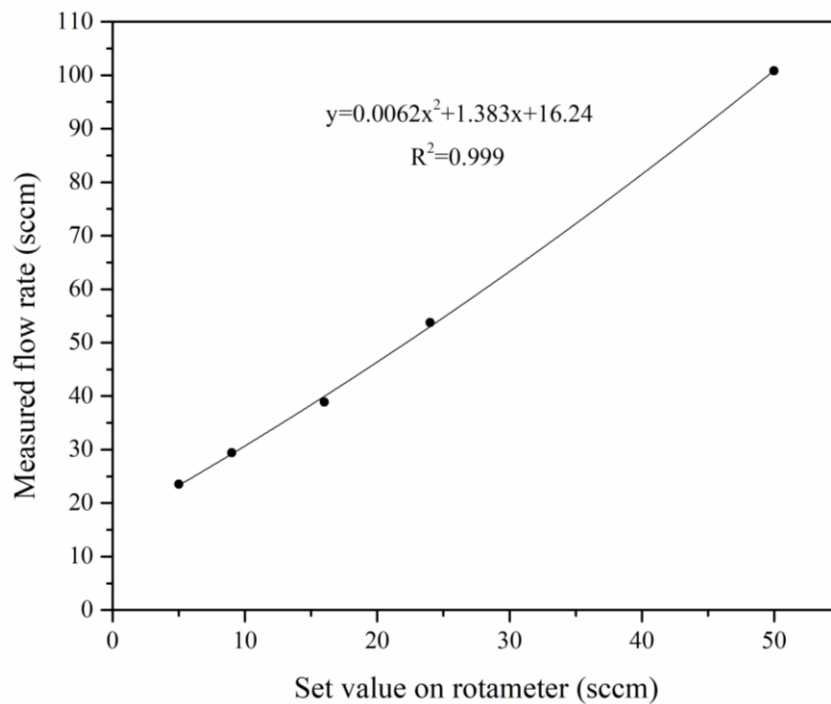
Figure 5.3: Hydrogen flow rate calibration curve.

The MTS mass flow rate was calibrated by measuring the change in MTS mass for various argon flow rates. The resulting curve is reported in Figure 5.4.
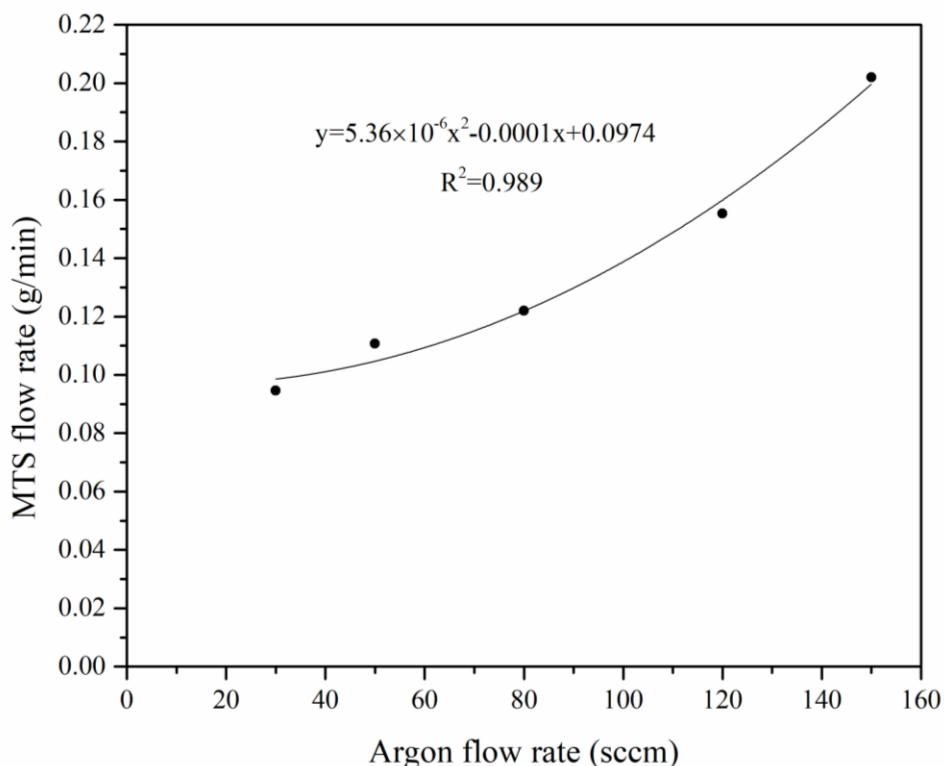
Figure 5.4: Calibration curve for the MTS mass flow rate.

5.3 Equipment/Apparatus

The experimental setup consisted of a commercial microwave source from Electronic GmbH & Co. (model no. PGEN2450/1.5–1.5KW2AIW). The equipment included a 1.5 kW power supply with MOS-FET amplifier, a microwave generator operating at 2.45 GHz and a water-cooled magnetron, as presented in Figure 5.5. Sub-atmospheric pressures were achieved using an Alcatel 2010I dual-stage rotary vane pump. The microwaves were guided from the generator along a rectangular waveguide fitted with three stub tuners and a sliding short. A transparent quartz tube, with inside diameter 20 mm and length 300 mm, was mounted between two support flanges, and positioned perpendicular to the metallic

waveguide between the stub tuner and the sliding short. The support flanges also served as in- and outlets to allow flow through the plasma zone. A graphite nozzle was inserted into the bottom of the quartz tube to bring about the spouting action of the bed. The nozzle was designed with a conical angle of 45° and an inlet diameter of 1.5 mm. A metallic grid was inserted into the top flange to prevent particles exiting the reaction zone.
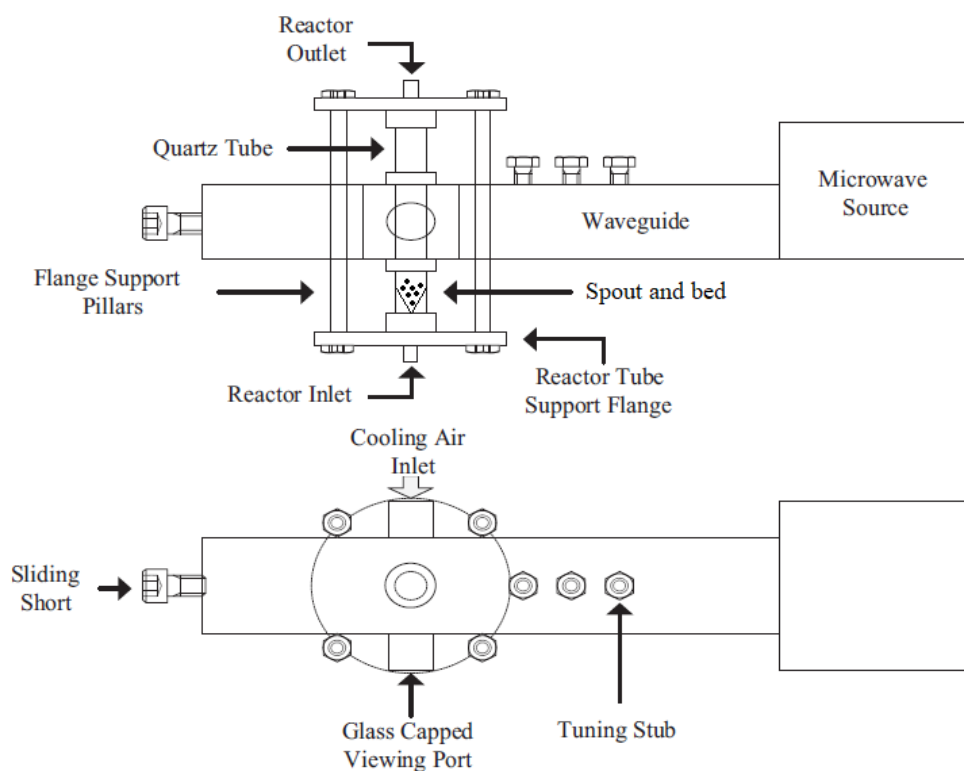
Figure 5.5: Physical layout of reactor assembly.

Argon and hydrogen flow rates were regulated using Aalborg rotameters. MTS was fed into the reactor through the sweeping action of an additional argon stream diverted through the MTS container. The MTS vaporisation assembly consisted of a 250 mL borosilicate glass jar equipped with a lid containing an inlet and outlet port. The argon inlet line was placed above the liquid MTS level, enabling diffusion of MTS into the argon stream. The rate of MTS mass diffusion into the argon stream was calibrated through a series of runs, at various argon flow rates. After passing through the reaction zone, the exiting gas stream

76

was fed through a $Ca(OH)_2$ scrubber to remove HCl and any unreacted MTS from the waste stream before entering an extraction system. A valve at the reactor exit allowed for easy control of the reactor pressure during operation. The schematic representation of the complete experimental flow path is shown in Figure 5.6.
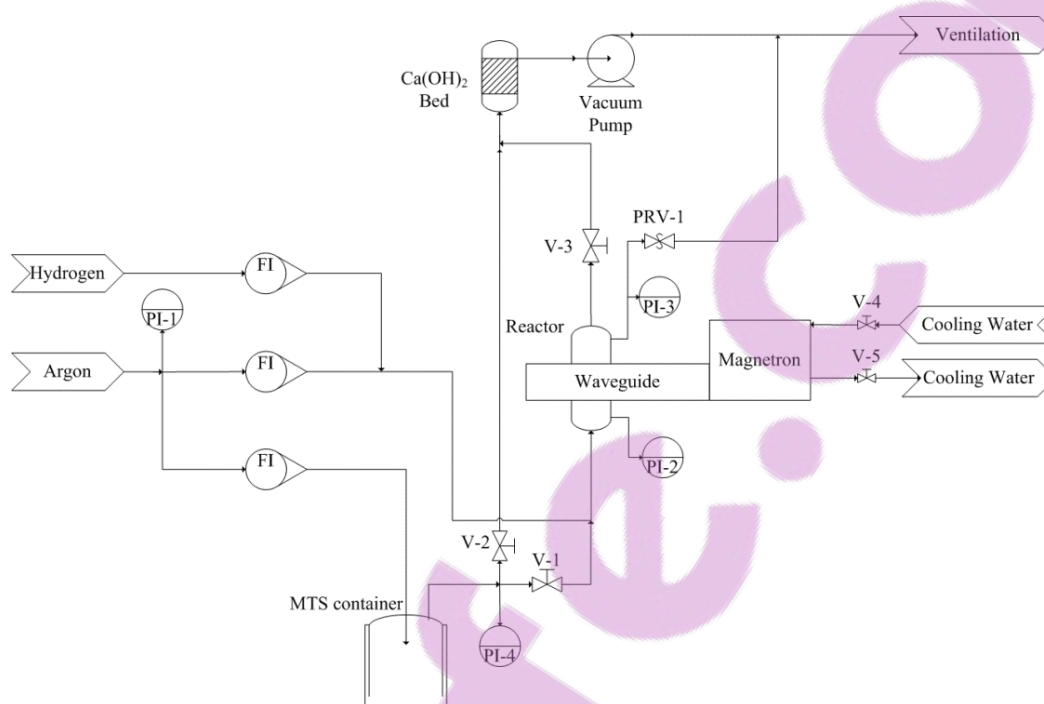
Figure 5.6: Schematic representation of the flow path of the experimental assembly (FI: flow indicator, PI: pressure indicator, PRV: pressure relief valve, V: valve).

MTS served as precursor material (> 99.0 % a/a) obtained from Merck & Co. Inc. Argon and hydrogen gas cylinders were obtained from African Oxygen Limited (Afrox) with > 99.9 % purity. The alumina spheres (Microbit Leonardo Microbeads) had a size distribution of ϕ = 1.5 mm to 2.5 mm, and a total bed mass of approximately 1 g (50 spheres) was used per experimental run. The spout design is shown in Figure 5.7, and was placed at the bottom of the tube (below the plasma zone). Particles were then spouted upwards through the plasma and fall back down.
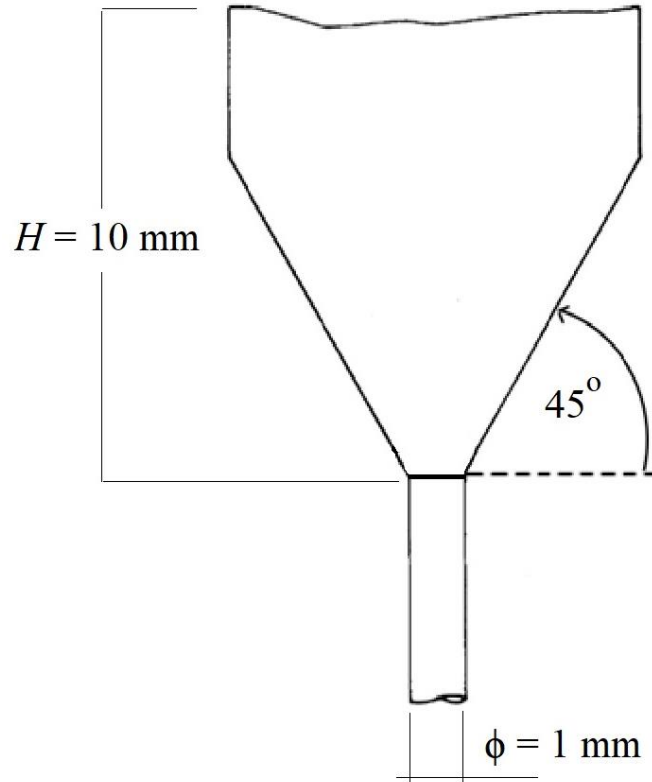
Figure 5.7: Spout design and bed height.

Using Equation (4.1), and substituting $H = 10$ mm, $\rho_f = 1.66$ kg/m³, $\rho_s = 3\ 950$ kg/m³, $d_p = 2$ mm, $D_i = 1$ mm and $D_c = 20$ mm, the minimum spouting velocity was determined to be $U_{ms} = 0.8$ m/s.

5.4 Design of Experiments

The experimental parameters are shown in Table 5.1. The design of experiments (DoE) was of a Box-Wilson 3-dimensional central composite design (CCD), covering a wide range of experimental parameters, within the capability of the system. This CCD comprises of an imbedded factorial design with a centre point that is surrounded by a group of 'star points', represented in Figure 5.8, to allow for estimation of the curvature. These star points are at a fixed distance $\alpha = [2k]^{\frac{1}{4}}$, where k is the number of factors [132].
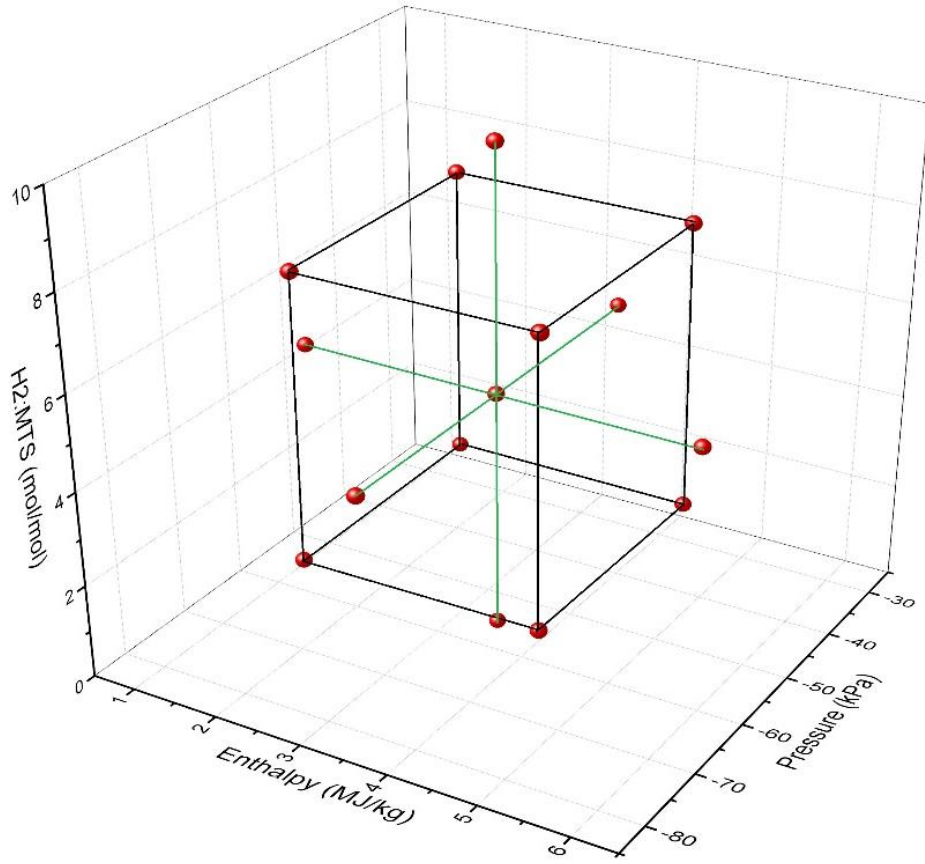
Figure 5.8: 3D central-composite DoE.

Table 5.1: Experimental Parameters.

Exp. No.	Spout velocity (L/min)	MTS flow (g/h)	H_2:MTS (mol:mol)	Power (W)	Pressure (kPag)
1	6.35	7.32	2	700	-50
2	6.35	7.32	8	700	-70
3	6.35	7.32	5	1000	-60
4	6.35	7.32	5	1000	-80
5	6.35	7.32	5	1000	-60
6	6.35	7.32	5	1000	-40
7	6.35	7.32	5	1000	-60
8	6.35	7.32	5	500	-60
9	6.35	7.32	8	700	-50
10	6.35	7.32	2	1290	-70
11	6.35	7.32	8	1290	-50
12	6.35	7.32	2	700	-70
13	6.35	7.32	8	1290	-70
14	6.35	7.32	10	1000	-60
15	6.35	7.32	5	1500	-60
16	6.35	7.32	0	1000	-60
17	6.35	7.32	2	1290	-50

5.5 Method/Procedure

Stable operation of the plasma system can be difficult to maintain, especially during the introduction of MTS vapour into the system. The following procedure was followed to minimise perturbances to the system as much as possible:

1. The vacuum pump is first switched on, and the pressure of the system is reduced to approximately 10 kPa absolute, with the valve above the reactor (V-3 in Figure 5.6) fully open.
2. The argon flow rate through the spout is initiated and increased to 6.35 L/min, which increases the absolute pressure to approximately 15 kPa. At this point the spouting action of the alumina pebbles is fully developed.
3. The microwave generator is initiated at 1 000 W, and the microwave plasma usually initiates shortly after. Failure to initiate is often an indication of an atmospheric leak, or contamination from a previous run.
4. At this point, hydrogen gas is introduced into the system at the required flow rate. The system is left unchanged for 3 to 5 minutes to allow for pressure stabilisation and cleaning of the alumina pebbles' surfaces (removal of moisture etc.).
5. The valve (V-3) is now slowly closed until the desired pressure in the reactor is achieved.
6. The argon flow through the MTS is initiated, and the valve allowing flow of MTS into the reactor (V-1) is opened slowly to allow for equalisation of the pressure in the MTS container (PI-4) with that of the reactor inlet pressure (PI-2).
7. During the experimental run, the alumina spheres darken in colour, and a black/brown powder deposits on the inner wall of the quartz tube.
8. The spheres are collected after runs, and the powder is flushed from the tube walls using acetone. The acetone is evaporated in a fume hood, and the powders are collected.

5.6 Characterisation Equipment

High-resolution scanning electron microscopy (SEM) was performed on the particles using a Zeiss Ultra Plus Field Emission Scanning Electron microscopes (Carl Zeiss, Germany) and transmission electron microscopy (TEM) was performed using a Phillips 301 instrument. Elemental mapping and energy-dispersive X-ray spectroscopy (EDX) were performed using a Quanta 200 3D SEM with an Apollo X Silicon Drift Detector (SDD). Powder X-ray diffraction (XRD) was conducted with a PANalytical X'pert Pro diffractometer using Co K_α radiation. The peak assignments were made using the databases supplied from the instrument manufacturer. X-ray photoelectron spectroscopy (XPS) was conducted using a Thermo ESCAlab 250Xi instrument, and verified with the PHI 5000 Scanning ESCA Microprobe. The peak deconvolutions were applied with assistance from the operators using the data reduction software package PHI MultiPak v9, using Gaussian-Lorentz fits. Optical photography of the particles was undertaken using a Nikon D7000 camera with AF-S Nikkor 18-200mm lens. Fourier Transform Infrared Spectroscopy (FTIR) was performed using a Bruker T27 Tensor spectrometer. Brunauer–Emmett–Teller (BET) analysis was performed using a Micromeritics TriStar 3000 Surface Area and Porosity Analyzer. Finally, thermogravimetric analyses (TGA) were undertaken using the Hitachi STA7300 instrument at the University of Pretoria.

5.7 Summary

The mass flow rates of MTS and argon were calibrated, and the calibration curves are reported. The experimental setup and apparatus are listed and described along with a schematic representation of the flow path. The materials (argon, hydrogen, MTS and alumina particles) purities are also reported. The experimental design followed a 3D central-composite design, with pressure, enthalpy (power) and hydrogen concentration as experimental parameters. Each step of the experimental run is reported systematically.

CHAPTER VI:
EXPERIMENTAL RESULTS & MATERIAL CHARACTERISATION

6 Results & Discussion

6.1 Introduction

In this chapter, the experimental results and accompanying statistical analyses are first reported. The results have been published [133] in the open literature. Deposition and growth rates are reported in Section 6.2, as well as the apparent kinetics of the deposition reaction. Section 6.3 presents the surface contour plots, and a brief discussion of the trends presented by them. This is followed by the Analysis of Variance (ANOVA) results in Section 6.4. This chapter continues with a summary of the SiC layer characterisation results, and expands on previously published results [133]. Section 6.5 focusses on the morphology and colouring of the layers, using optical photography and SEM techniques. This is followed by a brief look at the particle sizes using TEM imaging in Section 6.6. The elemental compositions are investigated in Section 6.7, utilising EDX, XPS, TGA and FTIR analyses. The crystallographic structure is discussed in Section 6.8 using XRD techniques, followed by surface area and porosity investigations in Section 6.9. Finally, a short discussion is presented on the effect of heat treatment on the deposited layers in Section 6.10.

6.2 Experimental Results: Deposition and Growth Rates

The system enthalpy, H_{TOT}, which applies to all the gaseous components present in the system (argon, hydrogen and MTS), was calculated using Equation (6.1).

$$H_{TOT} = \frac{P_f - P_r}{\dot{M}_{TOT}} \tag{6.1}$$

Here, P_f is the forwarded power, P_r is the reflected power, and $\dot{M}_{TOT}$ is the total mass flow rate. The measured deposition rates and growth rates are given in Table 6.1. The deposition rates, reported in g/h, were determined by the mass differences of the particles before and

after runs. The layer growth rates, reported in µm/h, were calculated by measuring the layer thicknesses on calibrated SEM micrographs. Using two independent methods has the added benefit of reducing possible measurement errors. The measured results appear to be in relative agreement with higher mass deposition rates coinciding with higher layer growth rates. It should be noted, however, that during preparation for SEM characterisation, the particles are embedded in an organic resin which often damages the SiC layer, making accurate layer thickness measurements vary slightly. Depending on the operating conditions, the mass deposition rates varied from 0.012 g/h to 0.208 g/h, and the layer growth rates varied from 50 µm/h to 140 µm/h. The lower values do not coincide with the same experimental point, suggesting that the various deposited layers do not necessarily consist of identical compositions or morphologies. This postulation is confirmed as the chapter progresses.

Table 6.2 reports the mean, standard deviation and 95% confidence intervals for both the mass deposition measurements and the layer growth rates. Due to the various measurement methods used, care was taken to restrict the significant figures of the reported values to the lowest amount confidently measured.

The kinetics of the deposition mechanism were further investigated by repeating an experiment for varying run times, while keeping the operating parameters constant. Seven runs were completed, varying from 3 to 40 minutes, and for each run a new batch of alumina spheres was used. The experimental parameters were set to that of experimental point no. 3 (the central point). The results are shown graphically in Figure 6.1, which indicated that two regimes are present with regards to the change in deposition rate, in contrast to the expected outcome of a constant deposition rate. A possible explanation entails a change in plasma enthalpy during each run, brought about by the additional deposition of SiC on the quartz tube walls.

Table 6.1: Results of deposition -and growth rate measurements.

Exp. No.	Deposition Rate (g/h)	Dep. Rate per Surface Area (g/(h·m^2))	Layer Thickness (µm)	Run Time (s)	Growth Rate (µm/h)
1	0.035	55.7	18.2	1304	50.2
2	0.060	95.5	17.1	1208	51.0
3	0.090	143.2	26.9	1200	80.7
4	0.208	331.0	47.2	1198	141.7
5	0.078	124.1	32.2	1216	95.3
6	0.116	184.6	24.3	1204	72.6
7	0.119	189.4	36.4	1200	109.3
8	0.030	47.7	17.5	1199	52.5
9	0.029	46.2	24.7	1200	74.2
10	0.180	286.5	36.0	1200	108.1
11	0.060	95.5	25.1	1200	75.2
12	0.060	95.5	26.2	1200	78.5
13	0.012	19.1	23.9	1199	71.6
14	0.067	106.6	23.9	806	106.7
15	0.090	143.2	22.5	1198	67.5
16	0.030	47.7	29.5	1201	88.5
17	0.077	122.5	24.7	1200	74.0

Table 6.2: Statistical functions of the measured deposition/growth rates.

	Deposition Rate (g/h)	Growth Rate (μm/h)
Mean	0.079	82.2
Stnd. Dev.	0.051	23.3
95% Confidence	0.024	11.1

This layer of SiC could potentially hinder the penetration of microwaves into the plasma [134, 135], an effect which is worsened with time and appears to stabilise after approximately 10 minutes. Some studies have shown that growth rates become constant after 1 minute [8], however this is not in full agreement with the experimentally observed pattern.
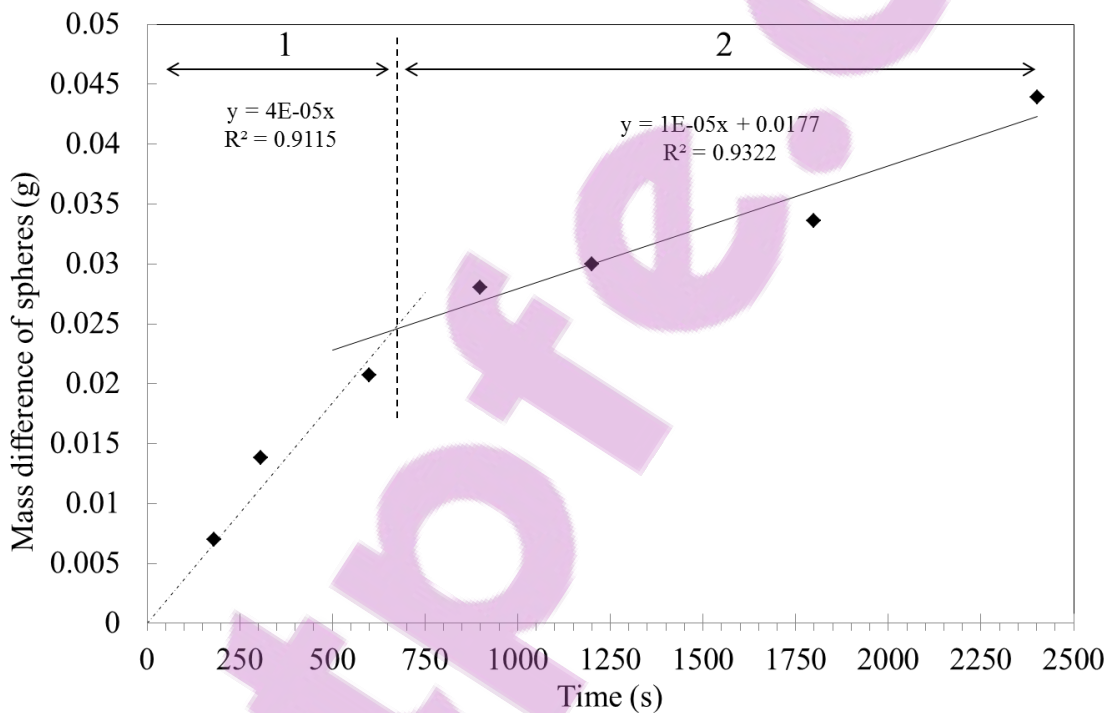
Figure 6.1: Experimentally determined deposition rate regimes of the SiC deposition mechanism, at the central point (Exp #3).

6.3 Contour Plots and Optimisation

The effects of the varying parameters on the deposition -and growth rates are represented using 3D surface contour plots, shown in Figure 6.2. These plots were generated using quadratic polynomials in the form of Equation (6.2).

$$y = c_o + c_1X_1 + c_2X_2 + c_3X_3 + c_4X_1X_2 + c_5X_1X_3 + c_6X_2X_3 + c_7X_1^2 + c_8X_2^2 + c_9X_3^2 + \cdots \qquad (6.2)$$

where X_1 represents enthalpy, X_2 represents H_2:MTS molar ratio, and X_3 represents system pressure. The plots shown here represent pressures of -50 kPag (a & d), -60 kPag (b & e) and -70 kPag (c & f). The values for the coefficients are given in Table 6.3 for the mass deposition and layer growth rates, respectively. An additional term, also shown in Table 6.3, was added to each polynomial to improve overall fit with minimal effect on the overall shape of the curves.

Table 6.3: Values for polynomial coefficients.

Response	c_o	c_1	c_2	c_3	c_4	c_5	c_6	c_7	c_8	c_9	Add. Term	C_{10}
Mass Dep.	0.459	2.34E-3	-0.037	0.021	0.023	-2.52E-3	-1.39E-3	-0.013	-2.46E-3	1.33E-4	$C_{10}X_1X_2X_3$	5.04E-4
Growth Rate	645.7	-380.1	25.88	13.50	-1.162	-8.089	0.318	50.02	-0.270	8.86E-3	$C_{10}X_1^2X_3$	1.038

When considering the surface contour plots (Figure 6.2), it is apparent that increasing the enthalpy generally increases the deposition -and growth rates. This follows the expected Arrhenius-type dependence of Equation (6.1) on temperature, with a broad range of activation energies summarised in Ref. [6]. In this study, increasing the microwave power

(enthalpy) increased the plasma temperature, yielding increased deposition rates. Likewise, an increase in H_2:MTS ratio also resulted in an increase in deposition -and growth rates, at least for most operating conditions. Hydrogen not only provides a more reducing environment, but likely takes part in the homogeneous decomposition reactions of MTS at low temperatures leading to solid deposition (SiC, Si or C) [6], described here by Equations (6.3), (6.4) and (6.5) [136].

$$CH_3SiCl_3 + H_2 \rightarrow SiCl_2 + HCl + CH_4 \tag{6.3}$$

$$CH_3SiCl_3 + H_2 \rightarrow Si + 3HCl + CH_3 \tag{6.4}$$

$$2CH_3SiCl_3 + H_2 \rightarrow SiCl_4 + SiCl_2 + 2CH_4 \tag{6.5}$$
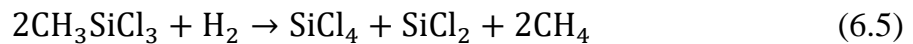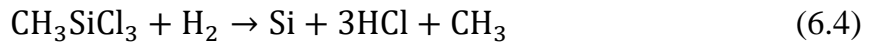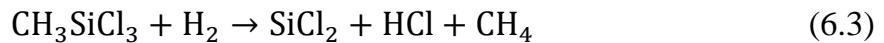
From these reactions, SiC is deposited through Equations (6.6) and (6.7).

$$CH_4 + Si \rightarrow SiC + 2H_2 \tag{6.6}$$

$$SiCl_4 + CH_4 \rightarrow SiC + 4HCl \tag{6.7}$$

When H_2:MTS ratios are very high though, the deposition rate is negatively influenced at low pressure settings (e.g. Figure 6.2 c & f) . This is possibly related to the high energy demand of hydrogen dissociation and ionisation [35], discussed in Chapter 2. At lower pressures, the mean free path of the particles is much larger, and collisions are less frequent. The plasma is consequently further from thermal conditions, resulting in lower temperatures, and possibly biased chemical reactions. Increasing the hydrogen concentration consequently requires higher energy input, which affects the plasma enthalpy and reaction rates.
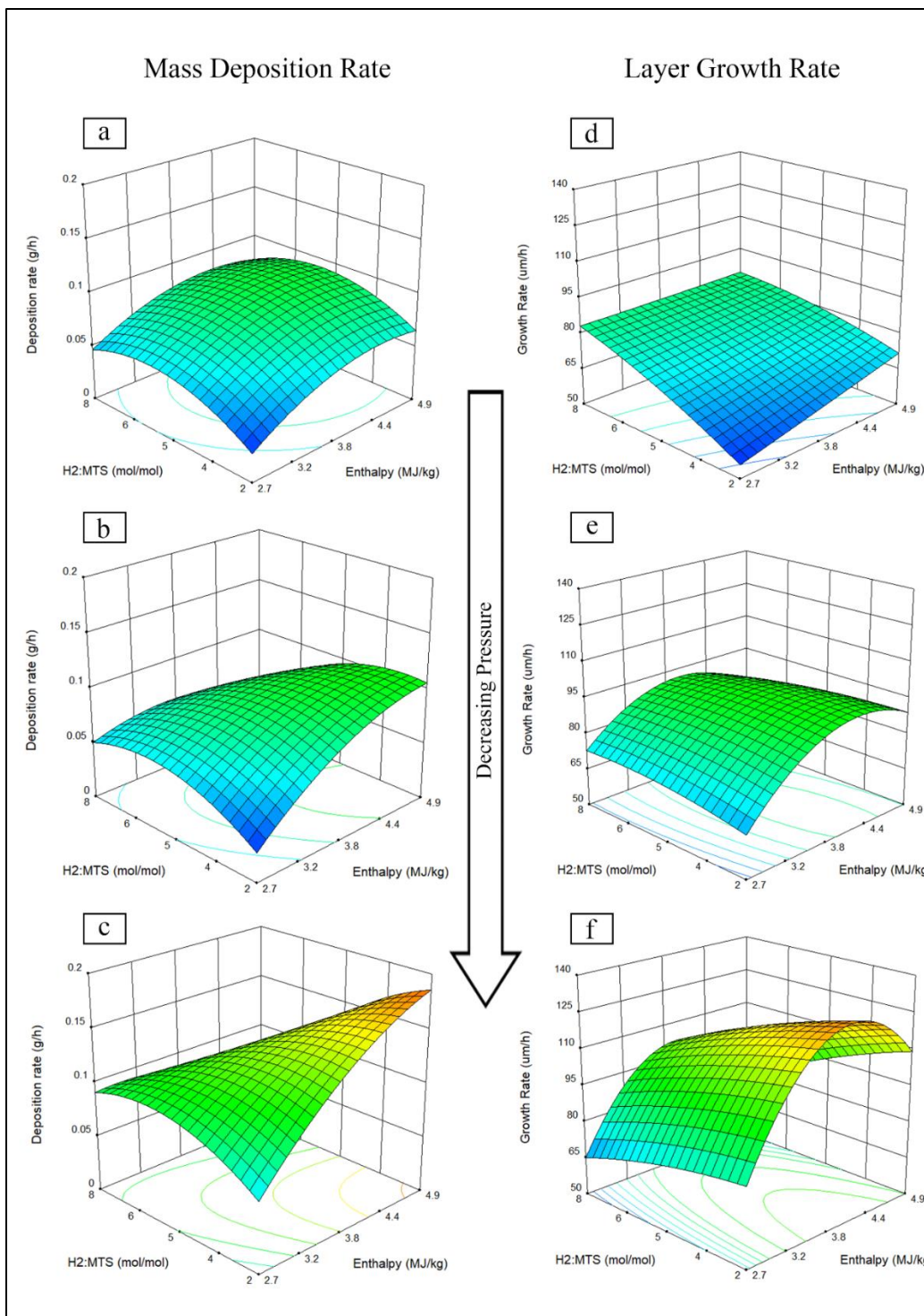
Figure 6.2: Surface contour plots depicting the effect of varying operating parameters on the mass deposition rate (a - c) and the layer growth rate (d - f).

90

This is possibly related to the high energy demand of hydrogen dissociation and ionisation [35], discussed in Chapter 2. At lower pressures, the mean free path of the particles is much larger, and collisions are less frequent. The plasma is consequently further from thermal conditions, resulting in lower temperatures, and possibly biased chemical reactions. Increasing the hydrogen concentration consequently requires higher energy input, which affects the plasma enthalpy and reaction rates.

Pressure, by contrast, exhibited an opposite effect by increasing the deposition -and growth rates as pressure decreases. This trend seems to exist for most settings of enthalpy and H_2:MTS ratio settings, although it appears to be much more prominent at high enthalpies. This trend is likely explained by the decrease in particle collisions associated with decreased operating pressures. Subsequently, non-thermal plasma conditions arise with operating temperatures below 1 300 K, which favour the production of silicon-rich deposits [6, 25, 67, 122]. It is possible that at these conditions, the deposition of Si is favoured, resulting in an apparent increase in the deposition rate. With regards to this experimental system, however, decreasing the operating pressure also affects the pressure inside the MTS container. This allows for a slight increase in MTS concentration in the feed stream, resulting in increased particle growth rates [137, 138]. It is also possible that decreasing the operating pressure will exacerbate any potential atmospheric leaks in the system, and increase the amount of SiO_2 formed during runs. The quality/composition of the layers may therefore provide a more accurate explanation of the observed trends and is further investigated in this chapter.

6.4   Response Surface Methodology (RSM) and ANOVA Analysis

The statistical relevance of these results was verified by an Analysis of Variance (ANOVA), which is summarised in Table 6.4 for both deposition -and growth rate models.

Table 6.4: Summary of the ANOVA results for each deposition model.

Response	Model F –value	Model p-value	Lack of fit p-value	Most significant term	Least significant term	R-squared	Pred. R-squared	Adeq. Precision
Mass Dep.	3.07	0.091	0.228	Pressure	H_2:MTS	0.836	-0.926	5.97
Growth Rate	2.90	0.102	0.450	Pressure	H_2:MTS	0.829	-1.84	7.22

In both cases, the model F-values are approaching 3, implying there is an approximate 10 % chance that F-values this large could occur due to noise. Additionally, the lack of fit p-values > 0.05 indicate that there is a non-significant lack of fit, which is a requirement for an adequate model. The adequate precision values measure the signal to noise ratio. A ratio greater than 4 is desirable. The reported ratios of 5.97 and 7.22 indicate adequate signals. In both cases, the models can therefore be used to navigate the design space; however, caution is always advised when doing so.

Both models indicated that the most significant term is that of pressure, which is apparent from the surface contour plots in Figure 6.2. The least significant terms are those for the H_2:MTS molar ratios.

6.5   Electron Microscopy and Optical Colour Mapping

Ten particles were randomly selected from each experimental run and placed onto an adhesive surface, mounted on a sample holder. The samples were carbon coated and underwent scanning electron microscopy (SEM) and energy-dispersive X-ray spectroscopy (EDX) characterisation.

The surface morphologies vary in structure depending on the experimental parameters. Micrographs of nine different samples are shown in Figure 6.3, Figure 6.4 and Figure 6.5. The samples shown here include the points of highest & lowest pressure, enthalpy and H_2 concentration, as well as the center point and two samples that exhibited large deviations in colour. Representative images are shown at low magnification (left columns) and high magnification (right columns) to investigate both large scale structures, as well as individual particle sizes and agglomeration. Some samples became unstable at higher magnifications due to electron charging, so they were limited to slightly lower magnifications. At $10^3 \times$ magnification (left column), the morphologies vary from smooth plateau-like features, e.g. Exp #1, to quasi-spherical (cauliflower-like) agglomerates, e.g. Exp #3. Often the light (electron) scattering appears lighter or darker, possibly due to the positioning in the SEM, sample height, contrast settings etc. At $10^5 \times$ magnification (right column), however, these agglomerates appear to become more dissimilar from each other. The quasi-spherical structures are still present in some samples such as Experiment numbers 1, 3, 6, 8 and 14. The agglomerates in experiments 4, 15 and 16 appear to consist of much smaller particles, densely packed together. Some samples even produced rod-like structures seen in Exp #10. These variations in nanoscale morphologies could potentially result in different macroscopic properties of the layers, including colour.

The images reported are representative of each sample, although deviations in the morphology did occur, likely due to deviations in the local particle-plasma environment, with gas composition and electron temperatures varying throughout the reactor volume.

Exp #1 (1000 x) Exp #1 (50 000 x)

Power: 700 W
H_2:MTS: 2
Pressure: -50 kPag

20 µm EHT = 1.00 kV   Signal A = InLens   Date :27 Jun 2017
       WD = 2.6 mm   Photo No. = 48833   Time :14:26:08

200 nm EHT = 1.00 kV   Signal A = InLens   Date :27 Jun 2017
        WD = 2.5 mm   Photo No. = 48827   Time :14:20:39

Exp #3 (1000 x) Exp #3 (100 000 x)

Power: 1000 W
H_2:MTS: 5
Pressure: -60 kPag

30 µm² EHT = 1.00 kV
        Signal A = InLens   Photo No. = 22801   Date :11 Apr 2017   WD = 2.2 mm

200 nm² EHT = 1.00 kV
         Signal A = InLens   Photo No. = 22783   Date :11 Apr 2017   WD = 2.4 mm

Exp #4 (1000 x) Exp #4 (100 000 x)

Power: 1000 W
H_2:MTS: 5
Pressure: -80 kPag

10 µm² EHT = 1.00 kV
        Signal A = InLens   Photo No. = 22830   Date :11 Apr 2017   WD = 2.3 mm

200 nm² EHT = 1.00 kV
         Signal A = InLens   Photo No. = 22829   Date :11 Apr 2017   WD = 2.3 mm

Figure 6.3: SEM micrographs of samples 1, 3 and 4 at low (left column) and high (right column) magnification.
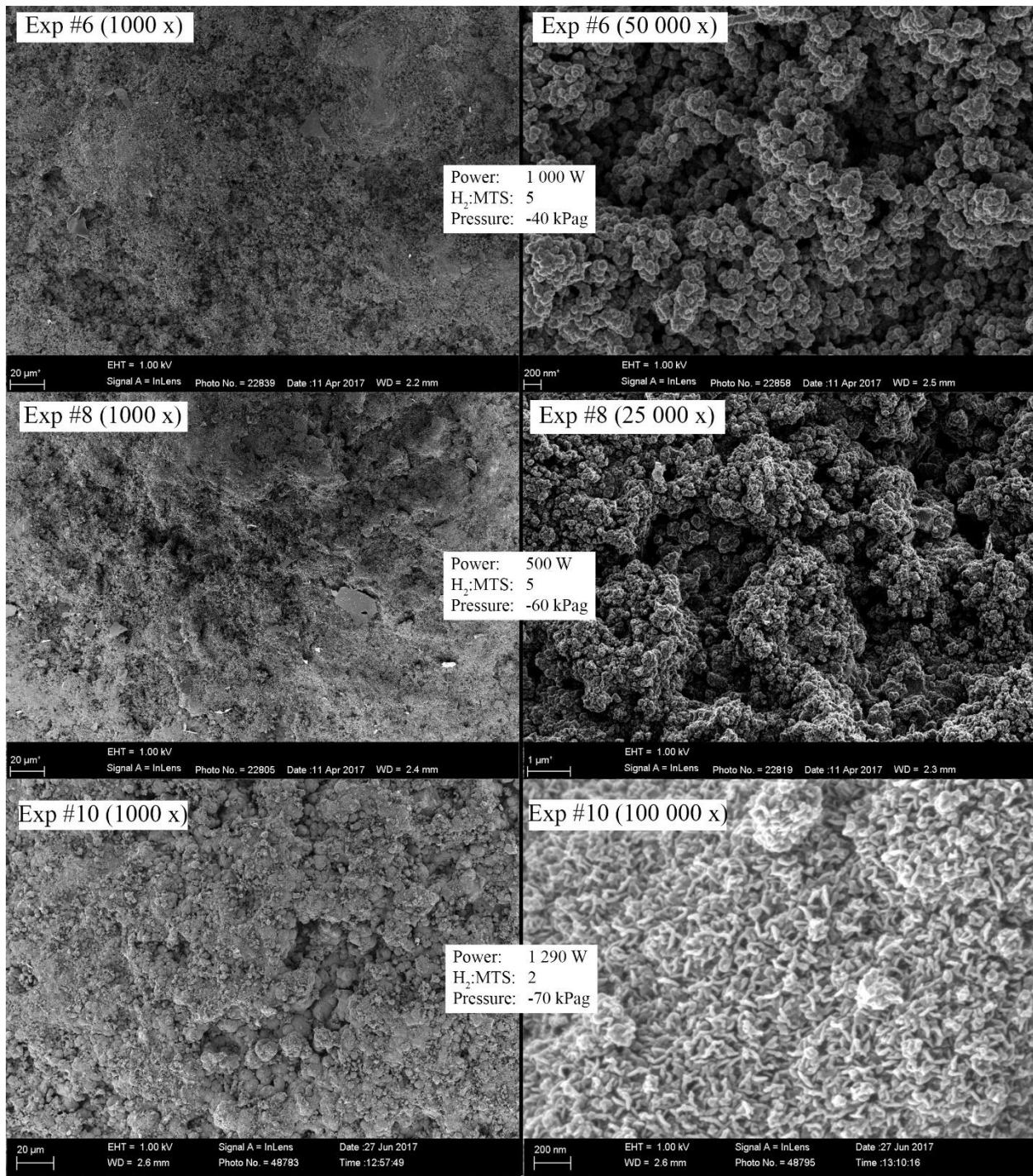
Figure 6.4: SEM micrographs of samples 6, 8 and 10 at low (left column) and high (right column) magnification.
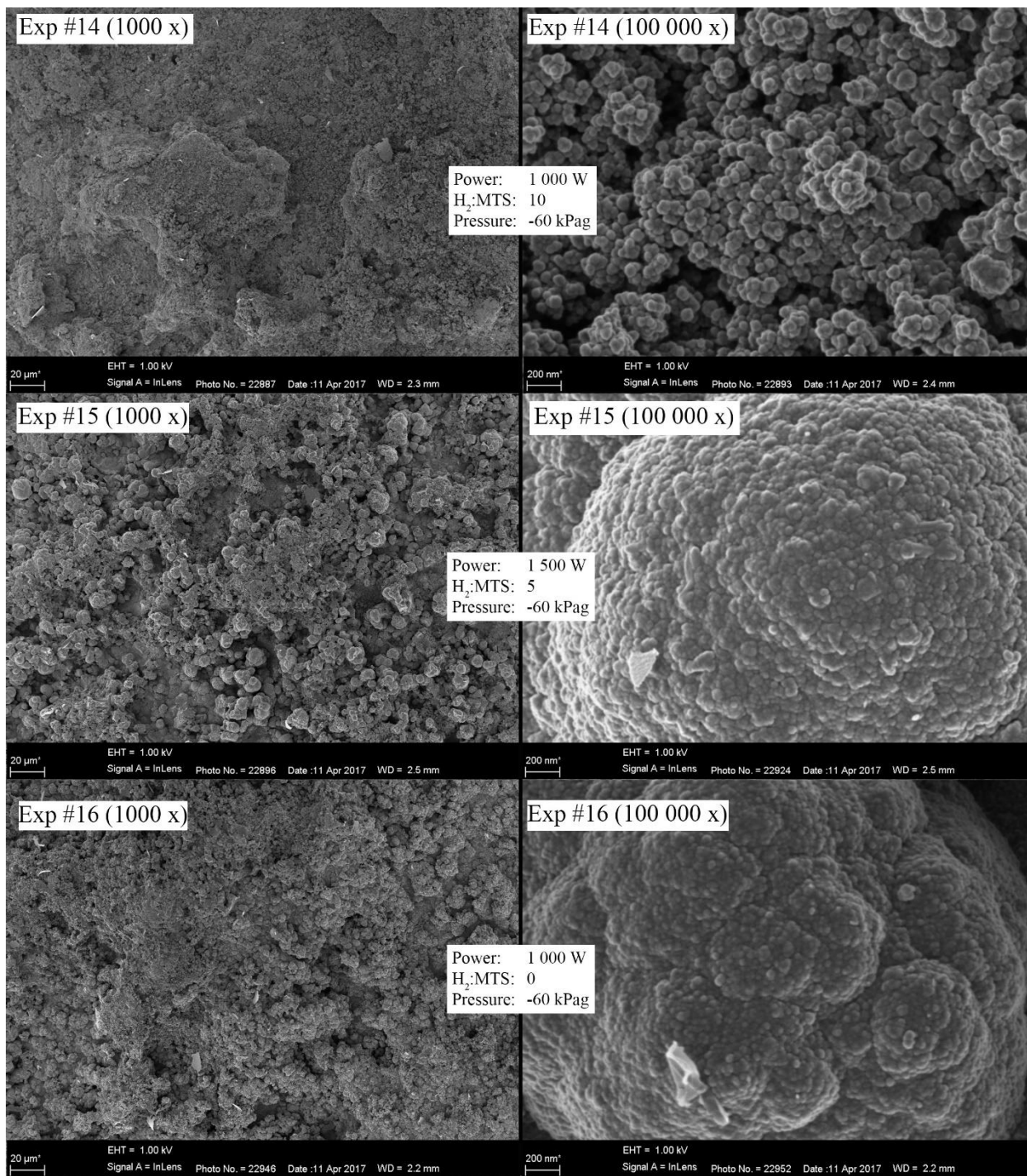
Figure 6.5: SEM micrographs of samples 14, 15 and 16 at low (left column) and high (right column) magnification.

A change was also noted in the colour of the final particles between experimental runs, illustrated in Figure 6.6 and Figure 6.7, similar to the morphological changes accompanying the varying operating parameters. Immediately apparent is the unusual colouration of Exp #4, discussed later.

Further investigation suggested that these colours are strongly influenced by the pressure and enthalpy conditions, whereas hydrogen concentration has a negligible effect. It is expected that the appearance of these colours is the direct result of the underlying morphological, and possible crystalline structures, inherent in the deposited layers, as well as their elemental composition. A generalised "colour chart" was accordingly created, shown in Figure 6.8. The interpretation of colour differs between observers, computer monitors and printers, and therefore caution is advised when interpreting these results.

Accordingly, the same chart template was used to visually represent the changing morphologies within the same regions, shown in Figure 6.9 using SEM micrographs. The transitions between the regions are not sharp, but rather indicate a gradual change in colour and morphology as the process parameters are varied.

Figure 6.6: Optical colours of samples 1 - 9.

Figure 6.7: Optical colours of samples 10 - 17.

The resulting graphs, in conjunction with the SEM micrographs, indicate that higher enthalpy values and lower pressures generally result in darker colours accompanied by smaller particle sizes (regions VI to IX). The system also shows denser structures at these conditions. In coatings, this typically means the deposition process allows for higher mobility of the precursors along the particle surface.

In contrast, lower enthalpy values and higher pressures result in slightly lighter colour variations accompanied by larger quasi-spherical agglomerates (regions I – V). These particle-like structures reflect a lower mobility of the precursor along the particle surface (i.e. high sticking coefficients) resulting in the more columnar and particle-like structures.

The colour variations are likely brought about by varying elemental compositions and/or microscopic variations in the accompanying morphological map. The changes in morphology are explained by the effect of the operating conditions on the film deposition and growth processes which generate specific morphologies. The temperature of a plasma system is strongly influenced by the microwave power, and a strong link is apparent between microwave power and particle size [26, 138]. When microwave power is increased, the particle size decreases, which is evident in the different morphologies presented in Figure 6.9. This result is supported by theoretical calculations done by Vennekamp et al. [24]. At lower power, the reactivity of the plasma results in a smaller number of nuclei. Molecules formed by the chemical reaction condense in the few nuclei, resulting in larger particles. Likewise, at higher power, more nuclei are formed, and thus smaller particle sizes are obtained [139]. Pressure, however, has an opposite effect, and appears to increase the particle sizes as it increases. This correlation is justified when compared to the literature [26, 140], where an increased pressure would allow for increased particle collision probability, resulting in enhanced particle growth.
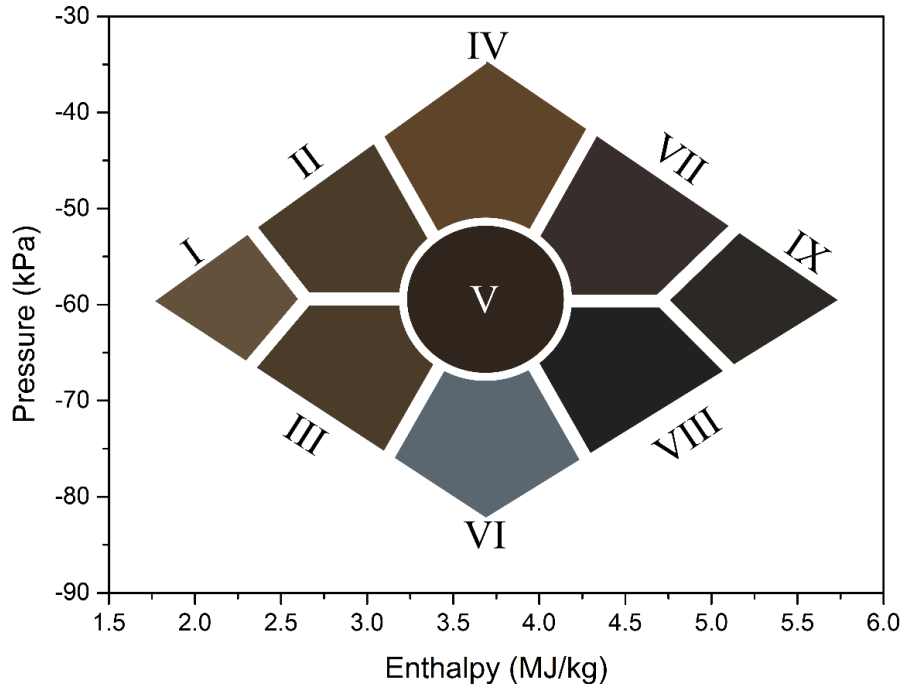
Figure 6.8: Colour chart representing various particle colours within the design space.
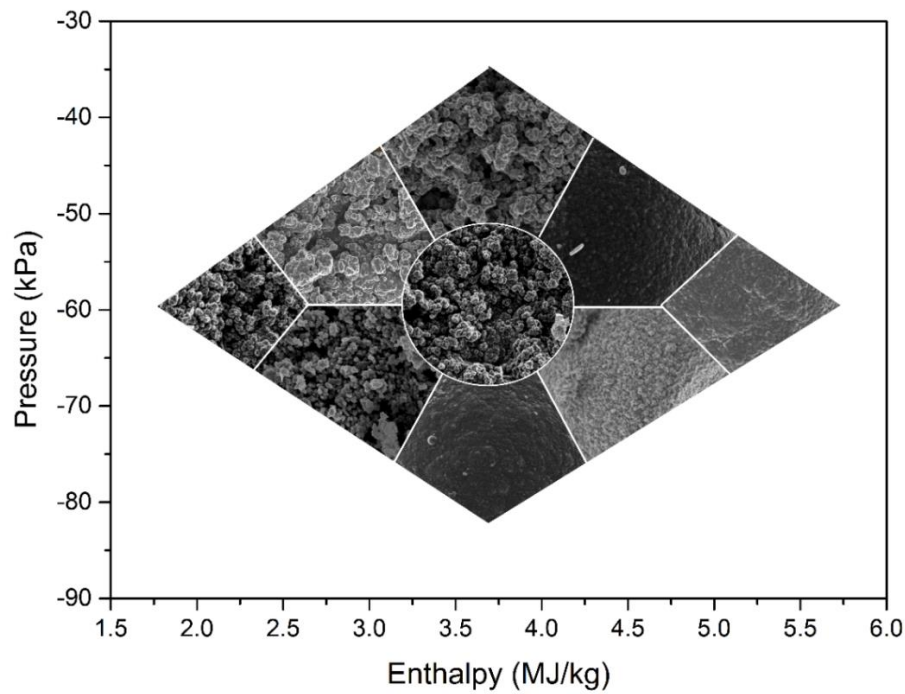
Figure 6.9: Similar chart showing the various morphologies throughout the design space.

6.6 Particle Size: TEM

Particle sizes were probed using TEM characterisation. The collected powders were analysed for this purpose; an example is shown in Figure 6.10. The image showcases an agglomerated particle, consisting of nano-sized particles, with sizes below 100 nm.
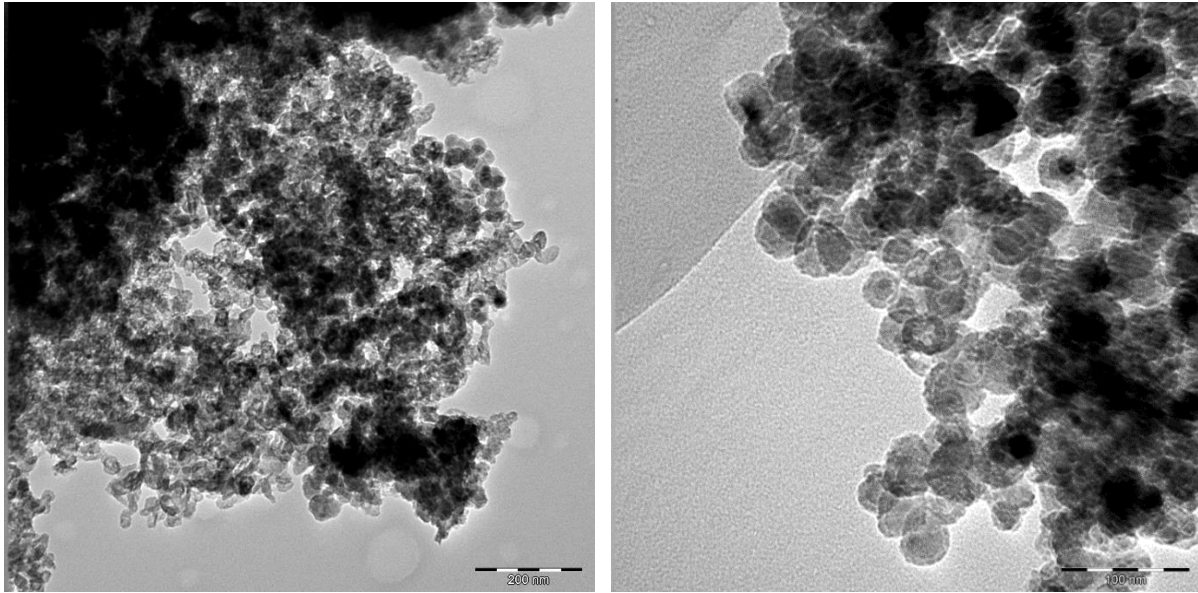
Figure 6.10: TEM image of nano-sized SiC particles.

TEM analyses can be very informative, given the correct instrumentation and operating knowledge. A more in-depth study of the microstructure of deposited SiC from MTS is reported elsewhere [66] using high resolution TEM micrographs.

6.7 Elemental Composition: EDX, XPS, TGA and FTIR

Five randomly selected particles from each experimental batch were embedded in an organic resin (Struers Epofix, resin 1), followed by grinding and polishing of the surface. The thickness of the resin was measured, and the diameter of the particles are known. The resin was then ground until the thickness was equal to the original thickness minus the radius of the particles. This ensured that the cross sections of the particles were clearly

visible. SEM micrographs of these cross sections were then used for layer thickness measurements, as well as elemental mapping using EDX, shown in Figure 6.11, Figure 6.12 and Figure 6.13. During elemental mapping, three distinct phases were identified based on the relative elemental compositions. EDX indicated a silicon/carbon phase, marked as blue (except in Exp# 3 where is was accidentally marked as red during scanning), however this phase is sometimes identified as a silicon rich layer (also blue). This discrepancy in the identification is likely brought about by a silicon-rich or carbon-rich SiC layer. These values should be considered with caution though, as it is well known that the identification of carbon is somewhat unreliable using EDX techniques.

When considering the "extreme" points i.e. the highest and lowest enthalpy, H_2:MTS and pressure points, some observable patterns become apparent. At very low pressure (Exp #4), the layer appears very thick, as discussed earlier, and is characterised as silicon only. This is in contrast with literature [65] and the XRD and XPS results reported later in this chapter. At high pressure (Exp 6) the layer is classified as a Si/C layer, indicating that a higher carbon content is present than at low pressure. At high enthalpy (Exp #15), the layer is clearly identified as a Si/C layer, whereas at low enthalpy (Exp #8) the layer is much thinner and is identified as a Si/Al/C/O layer. This suggests that the layer thickness is small so that the surrounding layers are also detected, and the supposed aluminium and oxygen content are likely from the alumina particle (yellow), and the carbon content could likely be from the organic resin layer (red), leaving a silicon-rich layer (blue) at these conditions.

At high H_2:MTS ratios (Exp #14), a clear Si/C layer is identified. At low H_2:MTS ratios (Exp #16), the layer is also clearly identified as a Si/C layer, again indicating that H_2 content has little effect on the elemental composition of the resulting layers.
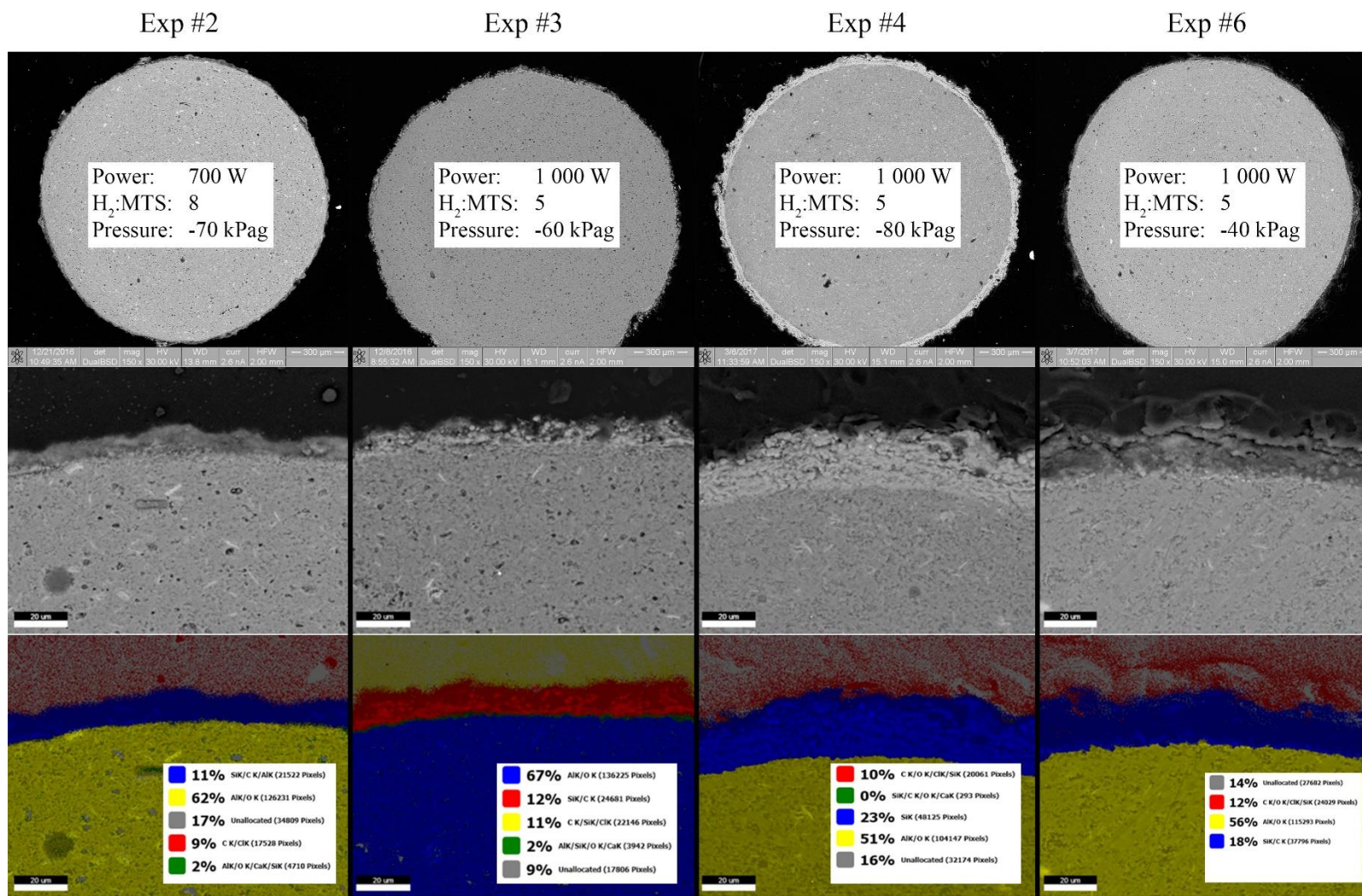
Figure 6.11: Elemental mapping of samples 2, 3, 4 and 6.
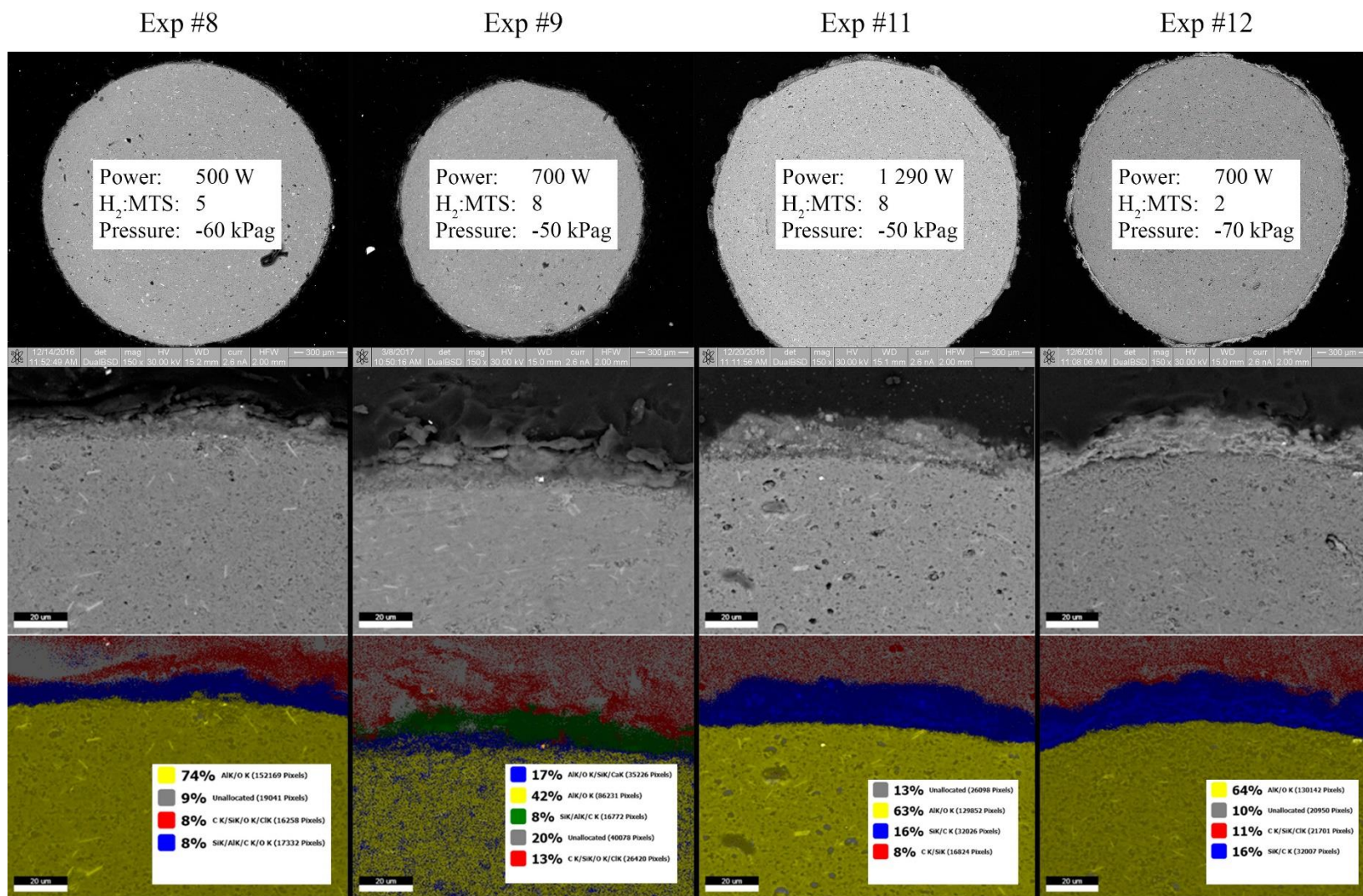
Figure 6.12: Elemental mapping of samples 8, 9, 11 and 12.
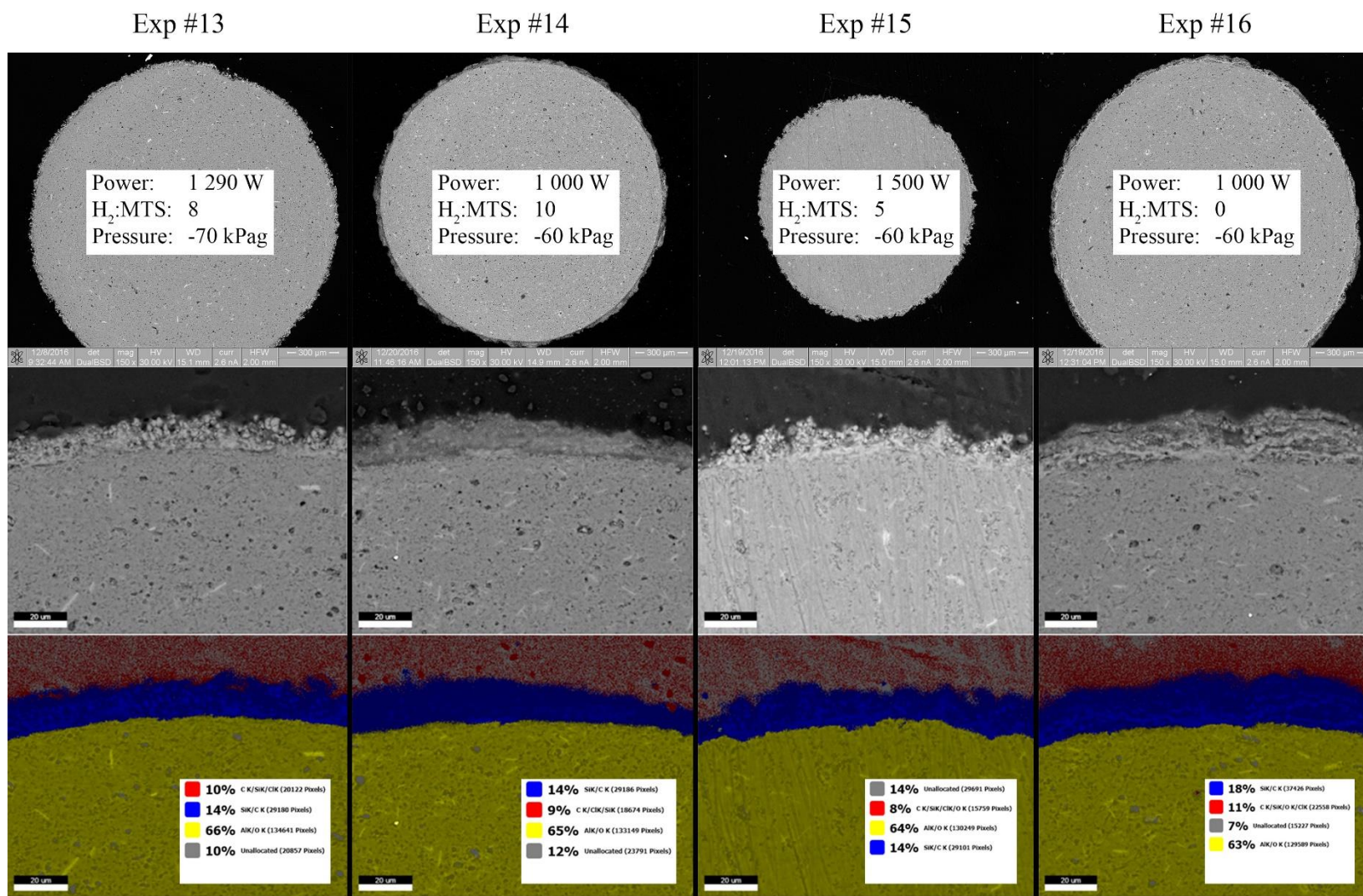
Figure 6.13: Elemental mapping of samples 13, 14, 15 and 16.

The surface chemistry of the deposited layers was characterised using XPS, in order to semi-quantitatively identify chemical compounds present in the layer, as opposed to single elements seen with EDX. Powders collected from the quartz tubes were submitted for XPS analysis. The carbon (1s) and silicon (2p) orbital results were accordingly deconvoluted and are shown in Figure 6.14 for two experimental points, namely the central point (Exp #3) and Exp #10. These two points were chosen as they were vastly different in their optical colours, which could allude to a difference in chemical composition. The corresponding peaks and their possible chemical states were identified from the literature [141-143].

Electron Orbit	Exp #3	Exp #10
C 1s		
Si 2p		
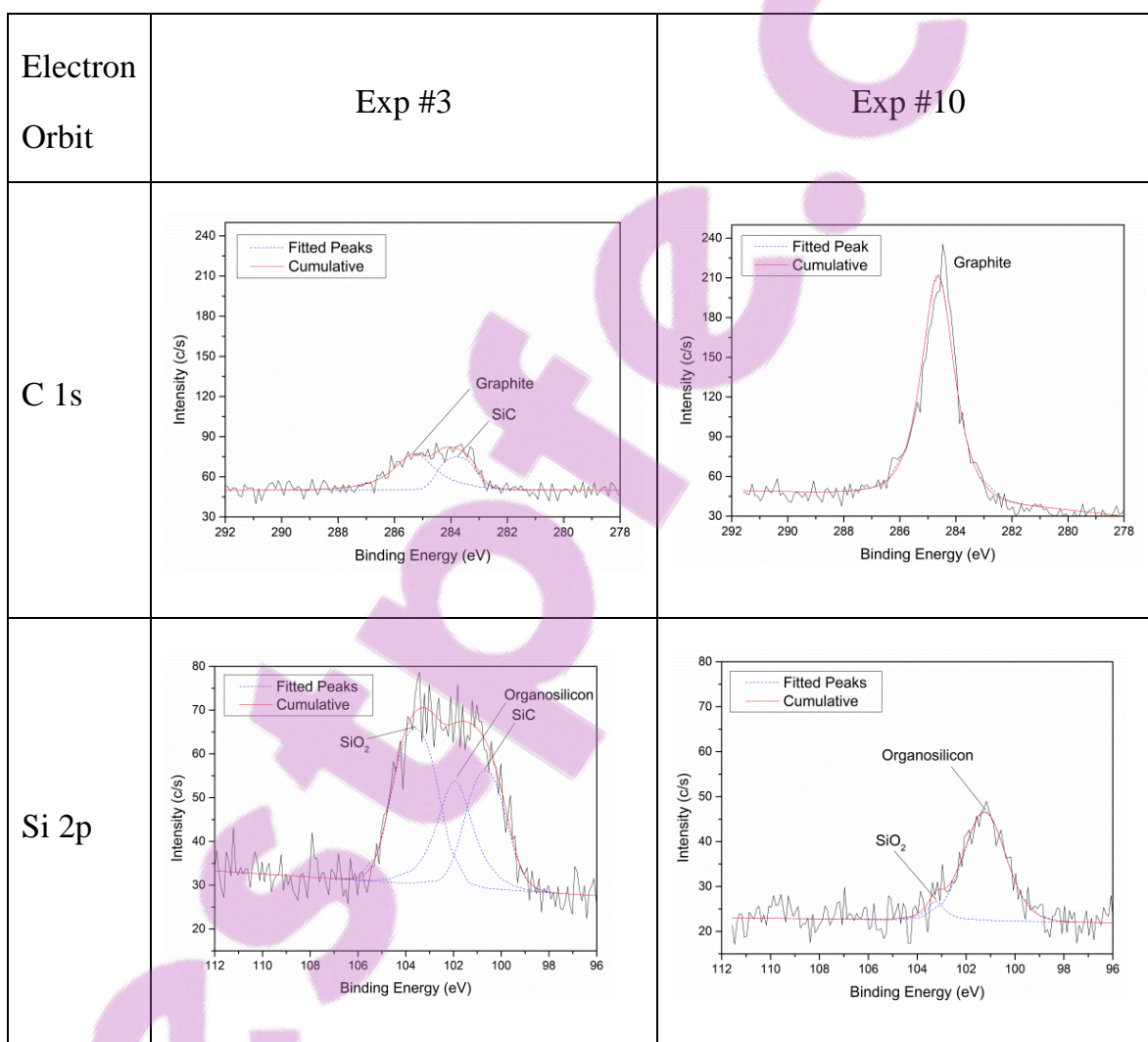
Figure 6.14: Comparison of XPS spectra for Exp #3 (left) and Exp #10 (right).

Exp #10 yielded a sharp graphite peak, indicative of a carbon-rich deposit which might explain the darker colours seen in region VIII of Figure 6.8. This supposedly corresponds with low deposition pressures, where the silicon atoms desorb more rapidly [144]. The organosilicon peaks are likely indicative of unreacted or partially reacted MTS compounds embedded in the layers.

In order to quantify the amount of organosilicon present in the layers, the corresponding powders from both of these runs were submitted for thermogravimetric analysis (TGA) in air as well as both nitrogen and argon atmospheres; the results are shown in Figure 6.15. Sample weights were 8.167 mg and 14.183 mg (at the discretion of the operator) taken from Exp #3 and Exp #10, respectively, and placed in an alumina pan. The temperature was ramped to 1 000 °C at a rate of 10 °C/min and then kept constant for 15 min. Gas flow rates were set at 200 mL/min.

The TGA results in Figure 6.15 illustrated that as much as 16 % of the layer's weight is likely composed of organosilicons, which likely decomposes to form Si and HCl. This mass loss appears to occur in three distinct steps, independent of background gas, possibly due to the evaporation of unreacted MTS, HCl and other organosilicons embedded in the layer.

A curious phenomenon that occurred is illustrated in Figure 6.16. Under argon, the SiC sample showed an initial decrease in mass, followed by an increase from approximately 400 ℃, mimicking the same trend when analysed in air. The analysis was repeated with the same sample, using a different instrument at a different facility, and the results showed a similar trend. The most likely explanation at present remains experimental error.
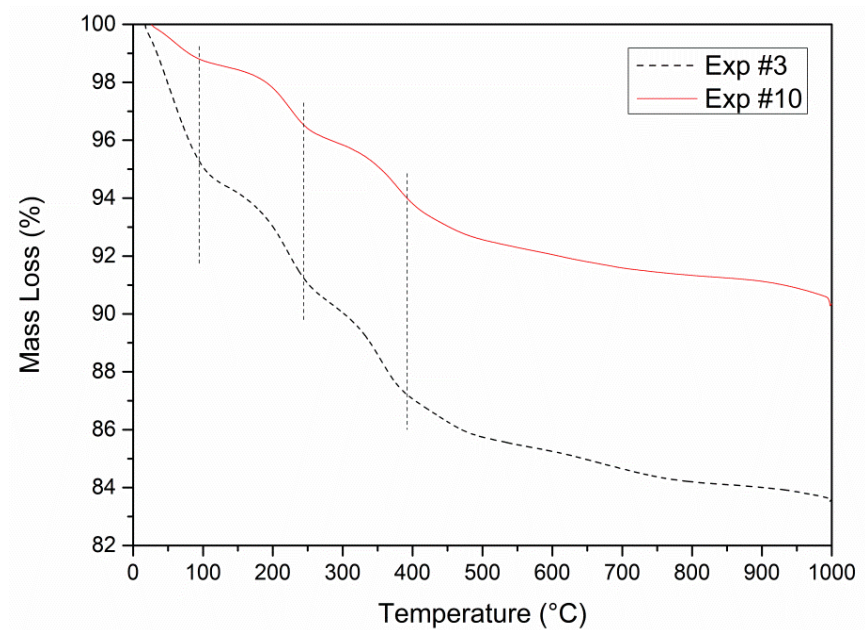
Figure 6.15: TGA in nitrogen, comparing the relative amounts of organosilicon between two samples.
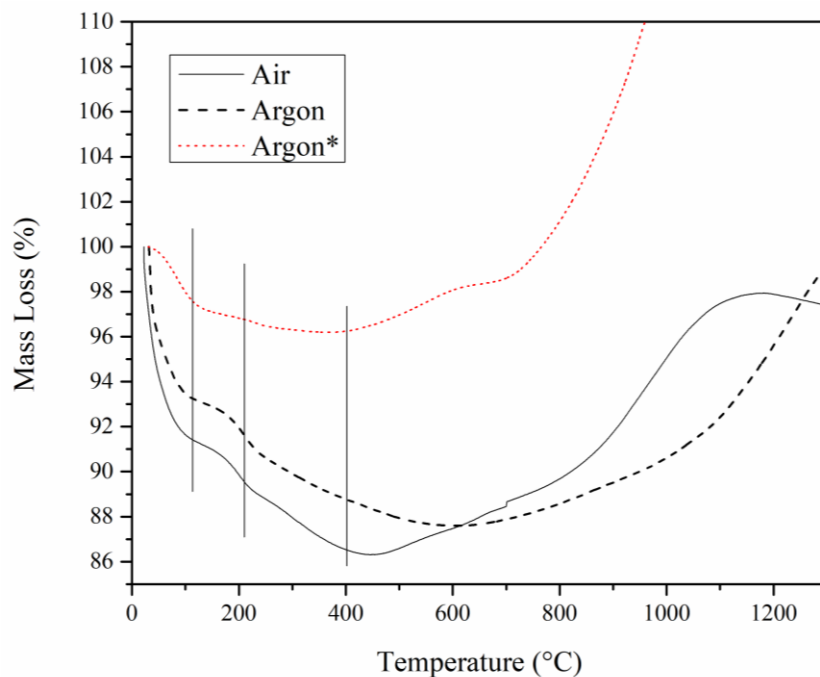
Figure 6.16: TGA curves of SiC under air and argon. Argon* was a repeat of the sample on a second instrument at a different facility.

109

The samples from the highest and lowest enthalpy and pressure experimental points were also submitted for XPS analysis. The results are given in Figure 6.17. Only the Si (2p) orbital spectra are shown here for conciseness.
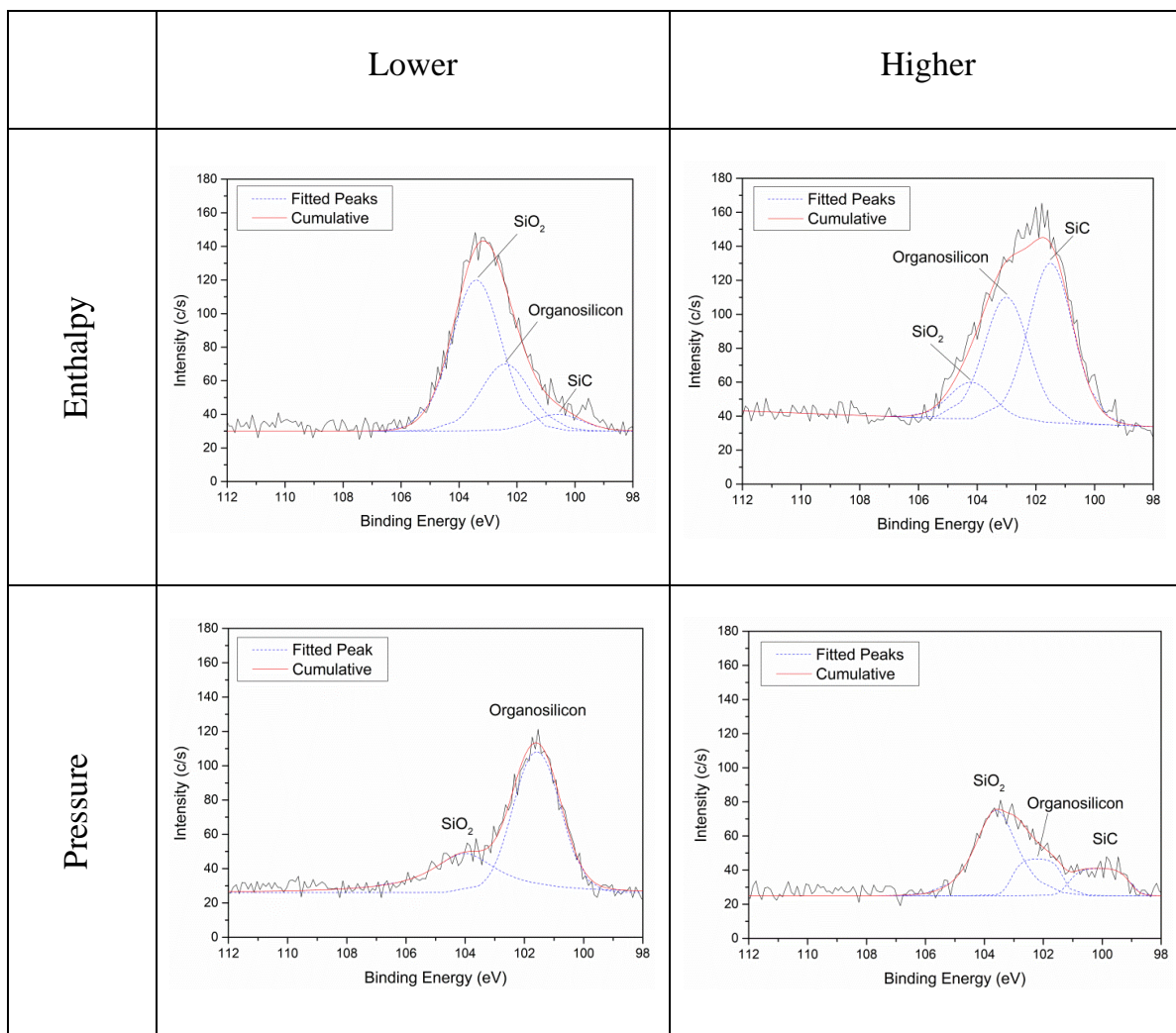
Figure 6.17: Si (2p) XPS results from the lower enthalpy (top left) and pressure (bottom left) and higher enthalpy (top right) and pressure (bottom right) experimental points.

The results demonstrate a relative increase in SiC with an increase in both enthalpy and pressure. The absence of silicon in the XPS results is likely due to the nature of the measurement technique, which limits the measurement area to the surface of the particles. It is expected that the free silicon on the surface has undergone oxidation and formed SiO_2, evident in the XPS results. Also evident, is that low enthalpy conditions (top left) yield silicon-rich layers, in agreement with EDX results, and high pressures (bottom right) also yield silicon-rich deposits.

For powder analyses, it was uncertain whether the powders collected from the quartz tubes were identical in composition to that of the layers deposited directly onto the particle surfaces. XRD and FTIR spectroscopy were subsequently used to confirm this assumption by comparing the powdered samples' spectra directly with those of the deposited layers. To this end, particles from the central point were sonicated in ethanol, after which the ethanol was evaporated, and the particles removed. The remaining powders were collected and submitted for XRD and FTIR analyses. The spectra are compared directly to those of the powders collected from the quartz tube during the same run. The FTIR comparison is shown in Figure 6.18. A standard β-SiC sample, obtained from Sigma-Aldrich, is also compared here as an additional verification of the presence of SiC in the product samples. The corresponding positions of the troughs are indicative of β-SiC, despite the large difference in the y-axis scales. Positions A and B are located at approximately 770 cm^{-1} and 1060 cm^{-1}, corresponding to bonded Si-C stretching and S-CH$_2$ rocking or wagging [136, 145]. Position B could alternatively be associated with Si-O stretching [136, 146].
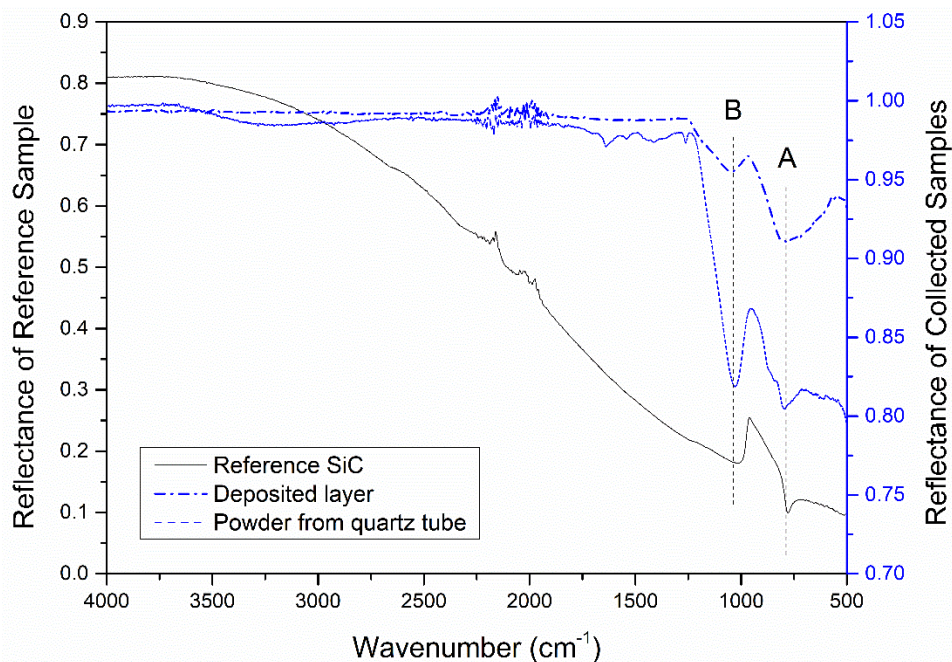
Figure 6.18: FTIR spectrum of the collected powders compared to a β-SiC reference sample.

6.8 Crystallographic Structure: XRD

Powders collected from the quartz tubes were submitted for XRD analysis. The presence of β-SiC (cubic) was confirmed for most samples, as well as the presence of silicon. The occurrence of broadened peaks suggests the presence of amorphous SiC, and its relative proportion varies between experimental runs. Again, the powders were collected from the runs corresponding to the lower and higher pressure and enthalpy limits, namely experiment numbers 4, 6, 8 and 15. These powders were submitted for XRD analysis and the results are shown in Figure 6.19. The corresponding phase amounts of crystalline material (weight %) were estimated and are reported in Table 6.5. The reader is cautioned as these samples indicated the presence of a large amount of amorphous material, which affects the accuracy of the results.

112

Table 6.5: Relative phase amounts (weight %) of crystalline material for highest and lowest pressure and enthalpy runs.

	Low P	High P	Low H	High H
Si %	31.40	15.60	20.00	42.90
SiC %	68.60	67.20	33.30	52.00
Quartz %	-	-	16.50	-
Unidentified %	-	17.20	30.30	5.100
SiC/Si ratio	2.180	4.310	1.670	1.210

All deposits are characterised by excess silicon, and initial consideration of the results indicates an increase in the amount of Si with an increase in enthalpy, accompanied by a decrease in Si with increasing pressure. This is in contrast to the expected occurrence of silicon-rich deposits at lower temperatures and higher pressures [144]. This is explained by considering that these values are only indicative of the crystalline material present in the deposits, and do not take into account the amount of amorphous material. It is therefore only evident that an increase in both pressure and enthalpy results in an increase in the amount of crystalline SiC and Si. Additionally, the preferred orientation of the deposits corresponds to the [111] and [220] crystal planes, giving much higher intensities relative to the [200] and [311] planes.

This trend of increased SiC deposition with increased enthalpy and pressure, is supported by the XPS results from the same experimental points (Figure 6.17), which also

demonstrates a relative increase in SiC with an increase in both enthalpy and pressure. The presence of SiO_2 is not seen in the XRD results as the SiO_2 is amorphous and does not appear on XRD measurements.

	Lower	Higher
Enthalpy		
Pressure		
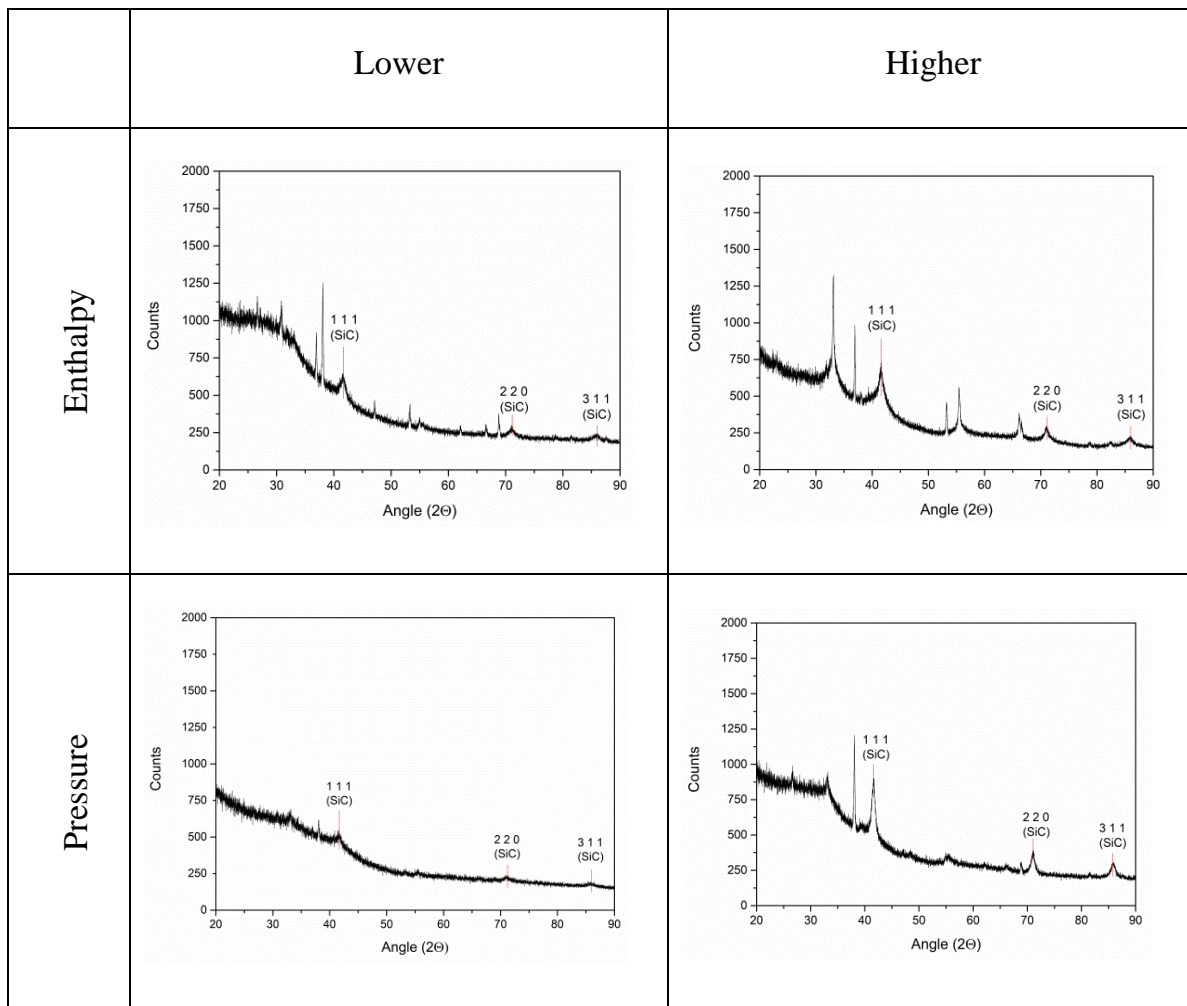
Figure 6.19: XRD spectra obtained from the minimum enthalpy (top left) and pressure (bottom left) as well as the maximum enthalpy (top right) and pressure (bottom right) runs, respectively.

The relatively high amount of amorphous material at low pressures could potentially be linked to the unusual discolouration seen in Figure 6.6. Additionally, XRD analyses were performed on the runs coinciding with those illustrated in Figure 6.1 to observe any

changes in the amount of crystalline material with run time. The XRD patterns are shown in Figure 6.20, and indicate an increase in the ratio of crystalline to amorphous material with increasing run time. The unlabelled peaks are those of silicon. The relative phase amounts of crystalline material (weight %) were estimated using the Rietveld method with the software program X'Pert Highscore Plus, and are given in Table 6.6.

Table 6.6: Relative phase amounts (weight %) from XRD patterns.

Time (min)	5	10	15	20	30	40
Si %	27.3	23.3	20.0	19.2	18.1	28.8
SiC %	72.7	76.7	58.0	80.8	81.9	71.2
Quartz %	-	-	22.0	-	-	-
SiC/Si	2.66	3.29	2.90	4.20	4.52	2.47

The relative phase amounts reported are those of the crystalline material only. The ratio of silicon carbide to silicon (SiC/Si) ranges from 2.47 to 4.52, while a run time of 30 minutes yielded the highest SiC/Si ratio of 4.52. A high percentage of crystalline SiO_2 (quartz) was identified in the sample running for 15 minutes. This anomaly is likely due to contamination from the quartz tube during collection of the powders.

When considering the results together with those of Figure 6.19, the relative SiC/Si ratios point towards a more stoichiometric Si/C deposition when operating close to the central point of the design space.
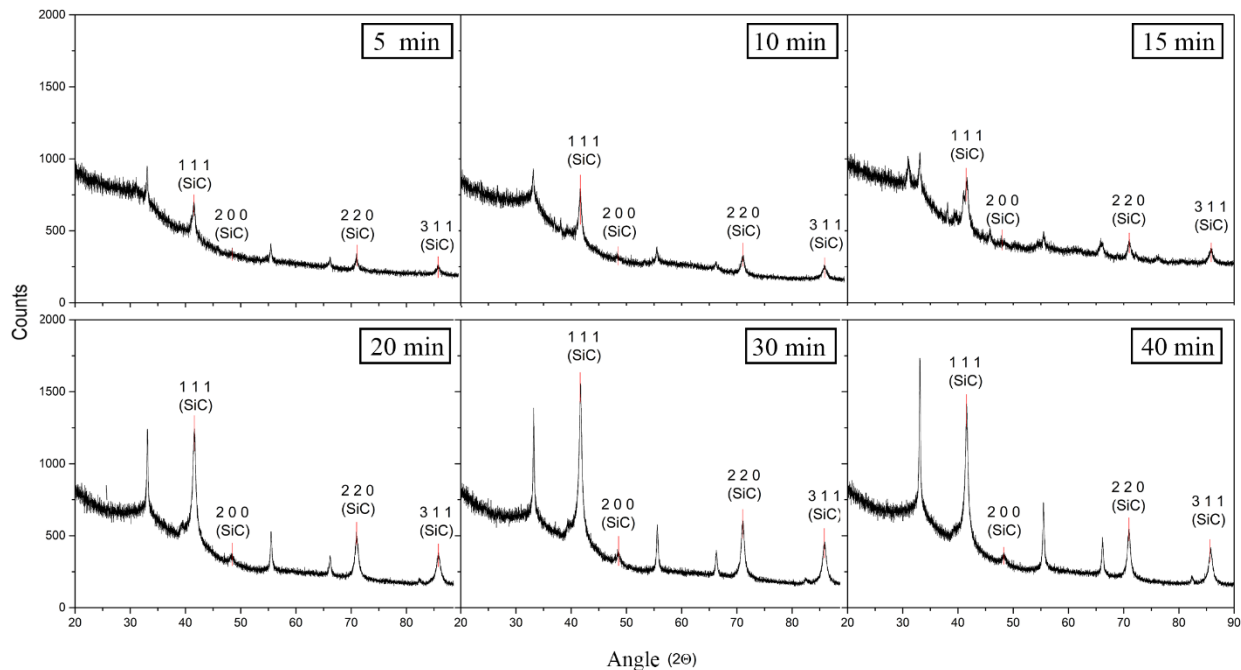
Figure 6.20: Graphical depiction of the change in XRD spectrum with run time.

Once again, to confirm the composition of the powders from the quartz tube are similar to those on the particle surfaces, an XRD comparison is shown in Figure 6.21. The comparatively small peaks of the sonicated powders are likely due to the small amount of powder available for the analysis, which approaches that of the lower detection limit of the instrument. Relative phase quantification using the Rietveld method, indicated that the powder and sonicated samples had similar SiC/Si ratios of 2.47 and 2.79, respectively.
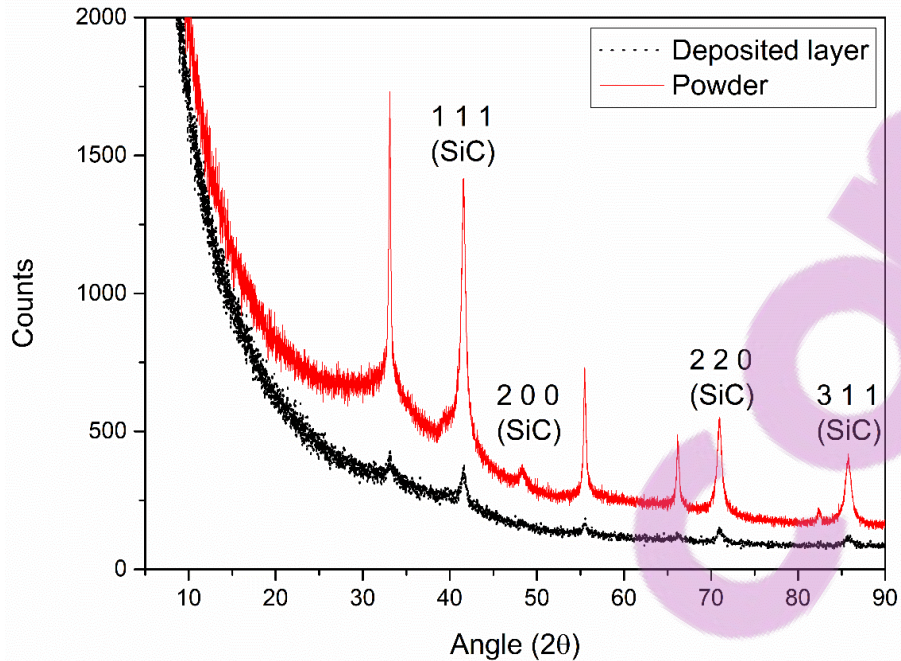
Figure 6.21: XRD-based comparison of the powders collected from the quartz tubes with those of the deposited layers on the particles.

6.9 Surface Area & Porosity

The powders collected from the central point (Exp #3) were submitted for BET analysis in order to quantify the surface area and surface pore volumes. The results are summarised in Table 6.7.

Table 6.7: BET analysis results.

Surface Area (m^2/g)	Error (%)	Micropore volume (cm^3/g)	Ave. Pore Width (nm)
46.3607	2.4	0.001881	8.9479

The accompanying adsorption/desorption isotherm (77.3 K) curve is reported in Figure 6.22. The shape of the curve corresponds most closely to that of a reversible Type II isotherm, given by the physisorption of most gases on nonporous or macroporous adsorbents. The gradual slope of the initial section ($\frac{p}{p^0} < 0.8$) indicates a significant amount of overlap of monolayer coverage and the onset of multilayer adsorption [147]. The corresponding pore size distribution is given in Figure 6.23, showing the majority of pore sizes to be below 20 nm, classified as mesoporous.
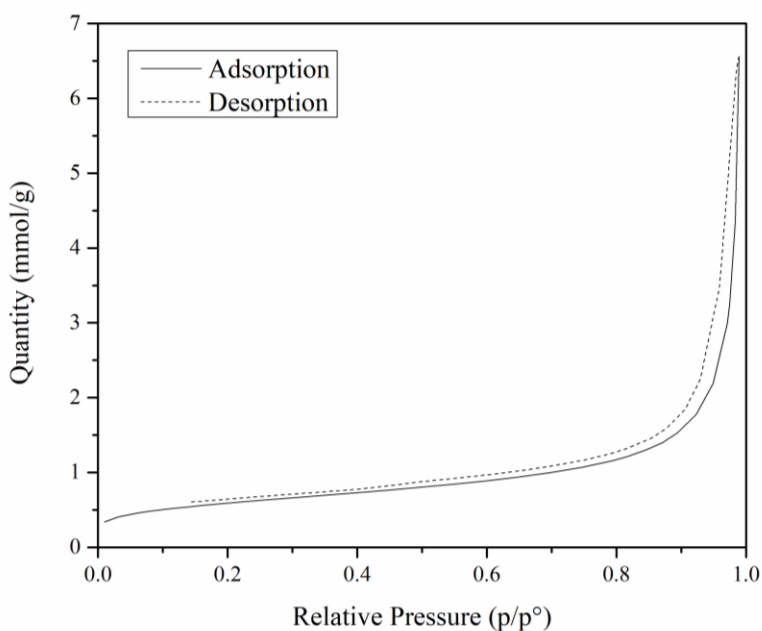
Figure 6.22: Absorption/desorption isotherm curve of SiC (Exp #3).
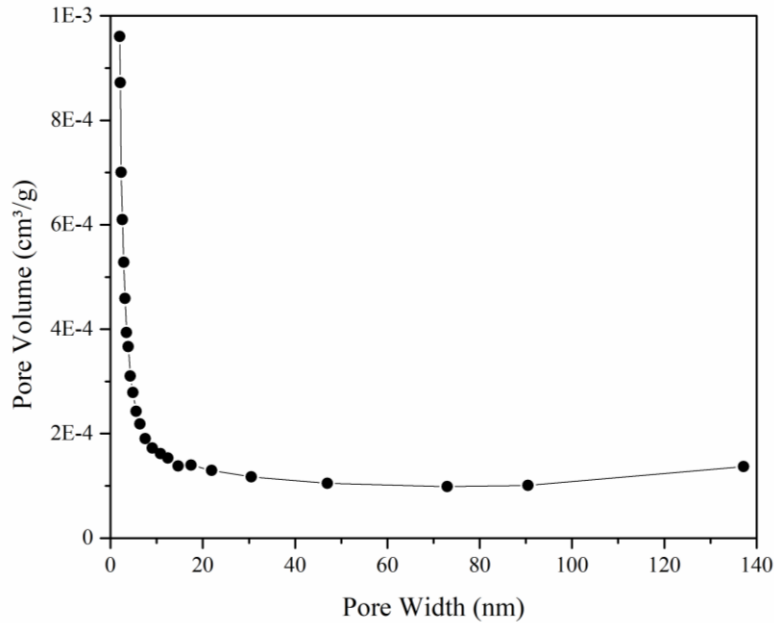
Figure 6.23: Pore size distribution of SiC powder.

6.10 Heat Treatment/Annealing

Particles from Exp #3 were annealed in air at 1 000 °C, and the SEM micrographs are shown in Figure 6.24 to illustrate the change in the physical structure of the layer. These images show that, after annealing, a sharper transition is apparent between the SiC layer and the resin. The layer becomes more defined and identifiable. Elemental mapping of the layer, shown in Figure 6.25, indicated that after annealing there was a marked increase in oxygen, indicative of silicon oxidation within the layer. There was also a decrease in chlorine, likely due to the evaporation/reactions of organosilicons indicated by the TGA results (Figure 6.15 & Figure 6.16) and the XPS results (Figure 6.14 & Figure 6.17).
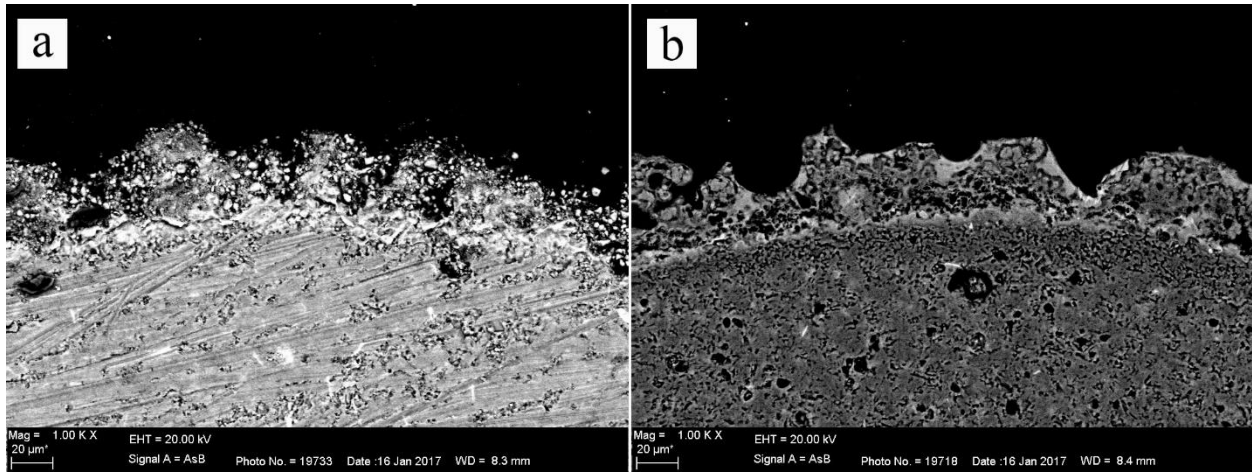
Figure 6.24: Comparison of SiC layer before (a) and after (b) annealing.
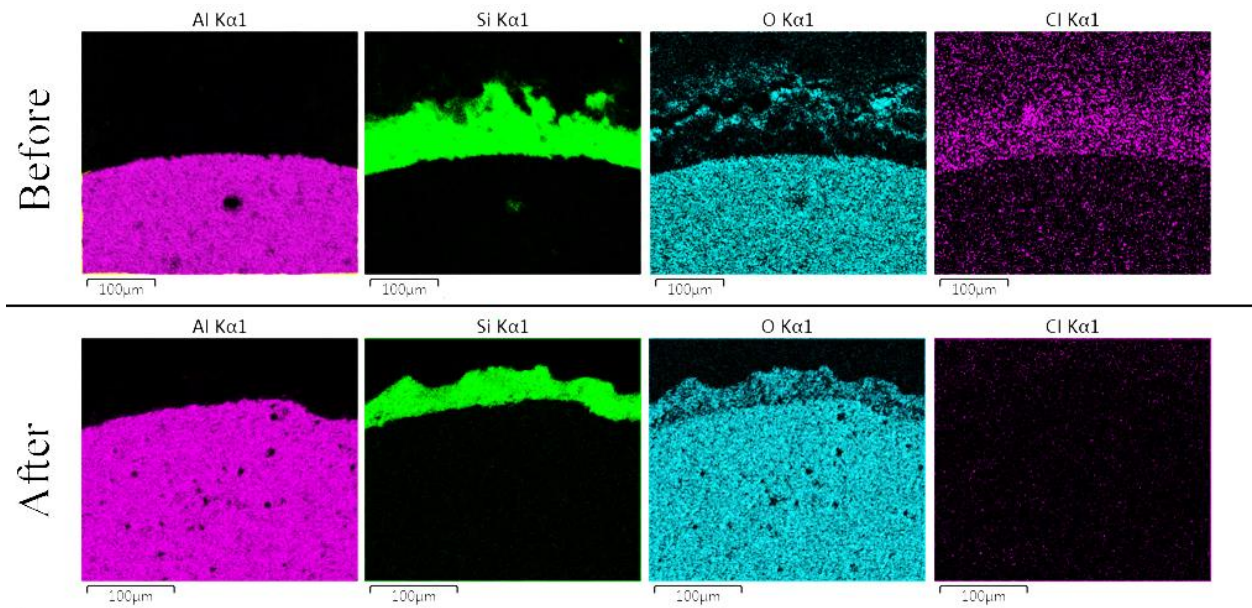
Figure 6.25: Elemental mapping of sample layer indicating the effect of annealing in air.

XPS characterisation of the annealed particles yielded the results shown in Figure 6.26. The result for the Si (2p) orbital is shown and compared to the same particle before annealing.
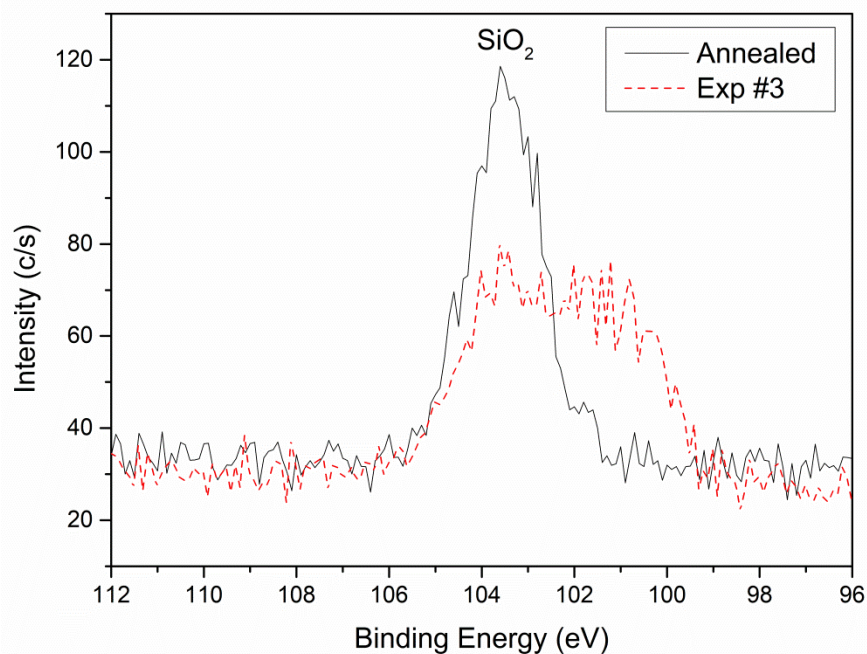
Figure 6.26: XPS comparison before and after annealing of the particles.

The result is a marked decrease in both organosilicon and SiC, accompanied by a relative increase in silica (SiO_2) on the surface. Due to the annealing process having been undertaken in atmospheric conditions, the increase in SiO_2 is likely the result of an oxidation reaction of Si, organosilicons and SiC on the surface of the layers.

6.11 Summary

Layer growth rates were measured and varied from 50 μm/h to 140 μm/h, and mass deposition rates varied from 0.012 g/h to 0.208 g/h. The differences in growth rate and deposition rate, evident in Figure 6.2, are likely due to the different morphologies and compositions of the layers deposited at different conditions. Repeated experiments at the central point (Exp #3) indicated that two deposition rate regimes are present, in contrast to

the expected outcome of a constant deposition rate. A possible explanation entails the additional deposition of SiC on the quartz tube, hindering penetration of microwaves. Surface contour plots, representing the mass deposition and layer growth rates, indicated an increase in enthalpy generally increases the deposition rate. Likewise, an increase in H_2:MTS ratio also caused in an increase in deposition rate, however, pressure appeared to have an opposite effect, increasing the deposition rate as it decreases. ANOVA results indicated the most significant parameter to be operating pressure.

SEM and optical photography results yielded both a morphological and optical colour map of a 2D section of the design space. These maps indicated that higher enthalpy values and lower pressures generally result in darker colours accompanied by smaller particle sizes, whereas lower enthalpy values and higher pressures result in slightly lighter colour variations accompanied by larger quasi-spherical agglomerates. TEM images confirmed that the agglomerates consist of particles below 100 nm. Using EDX, XPS, TGA and FTIR results, it was found that higher enthalpies and pressures yielded silicon-rich deposits. Considering XRD results in conjunction with these results, it was found that an increase in both pressure and enthalpy results in an increase in the amount of crystalline SiC and Si. TGA under argon atmospheres yielded counterintuitive results, ultimately showing a mass increase above 400 °C. Similar results were obtained from a second facility using a different TGA instrument.

Additionally, BET results indicated that the deposited powders have mesoporous structures. Heat treatment of the particles gave sharper transitions between the SiC layer and the resin under SEM investigation, as well as a marked increase in oxygen content, indicative of silicon oxidation within the layer. There was also a decrease in chlorine, likely due to the evaporation/reactions of the organosilicons.

CHAPTER VII:
MODELLING & SIMULATION

7 Modelling & Simulation

7.1 Introduction

Among the many CVD techniques, MW-PECVD has proven suitable for SiC synthesis and deposition [20-22, 24, 53, 139, 148, 149]. The main components of such a reactor are the waveguide and the quartz tube hosting the plasma zone. As discussed in previous chapters, high quality SiC layers demand that specific deposition conditions be maintained throughout the deposition process, emphasising the importance of process stability. Microwave plasmas, however, are known for their operational instabilities [150] manifesting as a propensity to extinguish or rapidly decrease in density. Additionally, the main criteria determining reactor performance in MW-PECVD are the shape and position of the plasma [151]. This emphasises the importance of a thorough understanding of the synthesis mechanism, along with the underlying physical processes. Various models have been investigated with the goal of diamond synthesis [152-154], cavity reactors [151, 155] and hot-wall reactors [156].

This chapter summarises simulation results on plasma densities and SiC growth rates in the experimental setup described in Chapter 5. The combination of heat, momentum -and mass transfer modelling, along with process simulation, allows the estimation of gas temperatures and growth rates, and the results will be discussed in the light of experimental results. It will also be demonstrated that the deposition of SiC on the quartz tube walls has a detrimental effect on the plasma density (i.e. SiC growth rates). A 2-dimensional (2D) MW-PECVD model is presented, which was created using finite element-based modelling software. The geometry, mesh sizes and parameters are reported in Section 7.2.A brief description of the model is given in Section 7.3, which expands upon the governing equations used in the simulation. The modelling software is briefly described in Section 7.4. The model couples various physical processes and the results include plasma chemistry (Section 7.5.1), flow dynamics and heat transfer (Section 7.5.2), chemical vapour

deposition of SiC (Section 7.5.3) and particle tracing (Section 7.5.4). The results are compared with observations from the experimental setup previously reported [157].

7.2   Geometry & Key Parameters

The experimental setup consists of a quartz tube, with inside diameter 20 mm and length 300 mm, placed perpendicular through a metallic wave guide. The quartz tube serves as the reaction zone and is transparent to microwaves which allows for seamless penetration into the gas while effectively containing the plasma region within the tube dimensions. A nozzle at the bottom of the tube, with a conical angle of 45° and an inlet diameter of 1.5 mm, facilitates the spouting action of alumina particles through the plasma, and a metallic grid at the outlet prevents the particles from exiting the reaction zone.

Two related but distinct models were developed for the simulation, as described in Section 7.3.1. Their respective geometries and mesh sizes are shown in Figure 7.1, along with the domain numbers and inlet boundaries. The model geometries were restricted to 2 dimensions, limited by available processing power. This drastically reduces the simulation times, while still revealing basic characteristics of the discharge but at the cost of lower accuracy. The mesh shapes and sizes were predefined as free triangular with a maximum element size of 7.77 mm and a minimum element size of 0.222 mm. Boundary layers were defined along the tube walls, with a smooth transition towards the interior mesh, following 8 iterations.
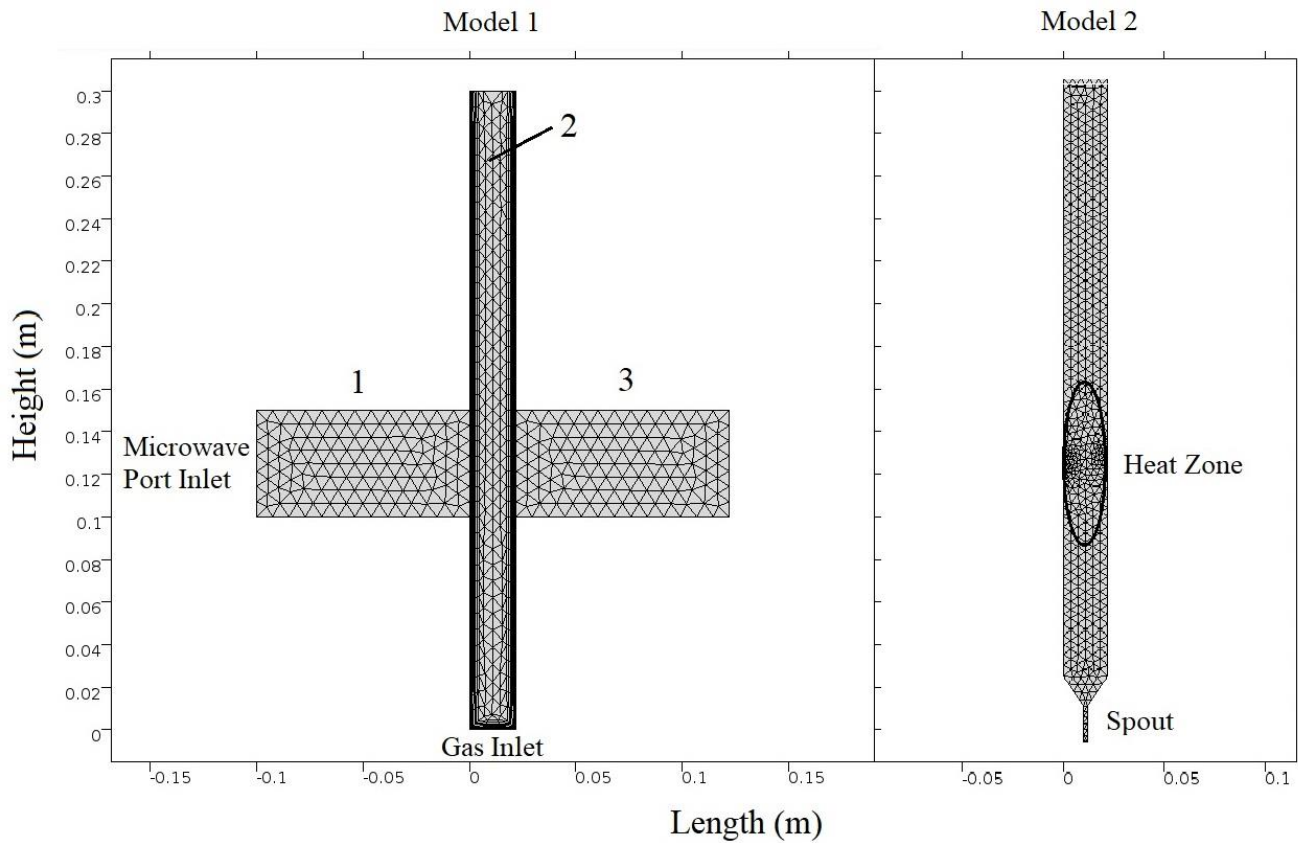
Figure 7.1: Mesh and geometry of the model with domain numbers and inlet boundaries.

The gas composition and operating parameters are defined in Table 7.1.

Table 7.1: Operating parameters.

Forwarded Power (W)	Absolute Pressure (kPa)	Mole fraction, H_2	Mole fraction, MTS	Spout Velocity (m/s)
1000	15	1×10^{-4}	1×10^{-5}	12

7.3 Simulation Model

7.3.1 General Approach

Two related but distinct models were developed for the simulation. The first comprises a fully-coupled set of partial differential equations (PDEs) describing mass-, energy-, and momentum transfer, as well as the electric and magnetic field behaviours. Speciation in the gas phase was computed from a system of ordinary differential equations (ODEs) used to describe their kinetics. It is a time-dependant model simulating the development of the plasma over a period of 10 milliseconds, with the physical properties of the gas phase calculated from the developing plasma composition. The second model was developed to predict the movement of an alumina particle inside the reactor. Plasma chemistry was omitted, and heating of the gas was instead facilitated by a "general" heating zone to reduce computing time. A spout was added at the reactor inlet to more accurately model the velocity profile inside the quartz tube. This model is also time-dependent, simulating the movement of the particle inside the reactor over a period of 5 seconds.

The general approach is illustrated in Figure 7.2, and represents three distinct phases of the modelling process.

7.3.2 Electromagnetic Fields

The solution of the Maxwell equations enables the calculation of the electromagnetic fields travelling through the waveguide, as well as the current flowing -and induced in the plasma:
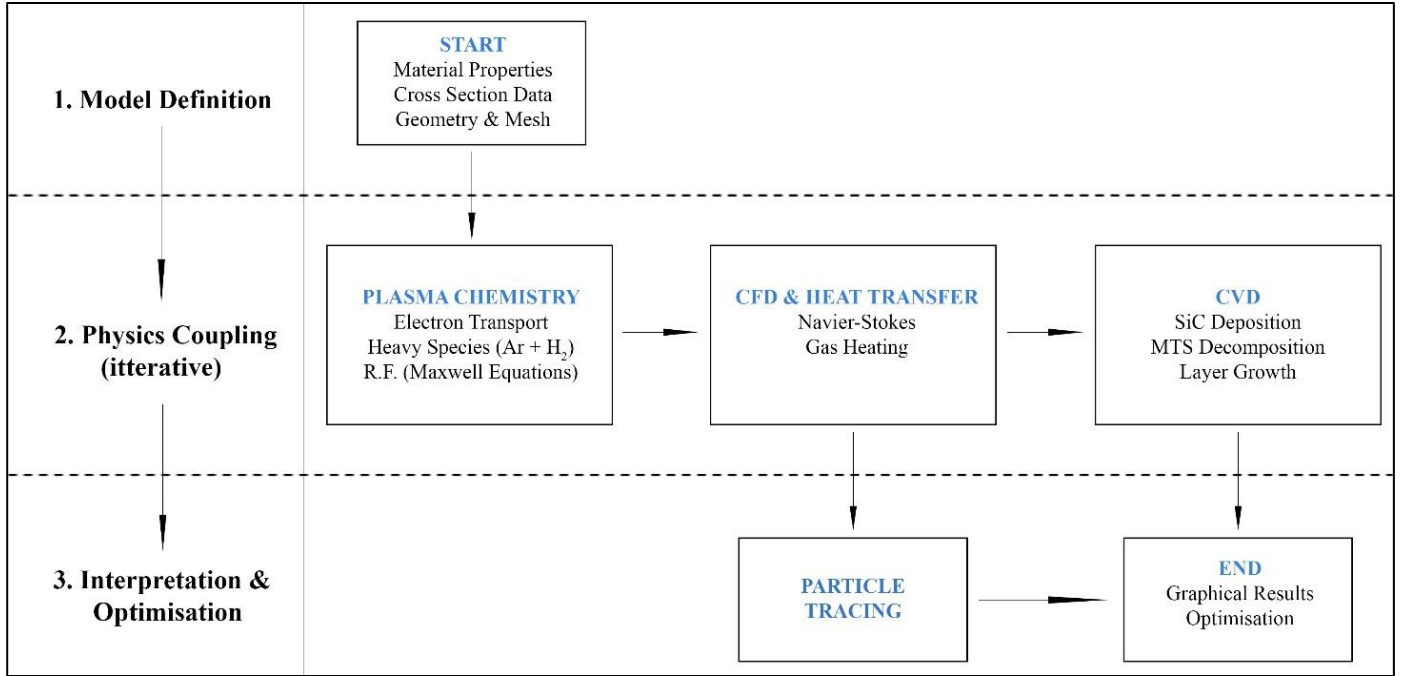
Figure 7.2: Plasma-CVD model approach.

$$\nabla \cdot \mathbf{B} = 0 \tag{7.1}$$

$$\nabla \cdot \mathbf{E} = \frac{\rho_c}{\epsilon_0} \tag{7.2}$$

$$\nabla \times \mathbf{B} = \mu_0 \mathbf{j} + \frac{1}{c_0^2} \frac{\partial \mathbf{E}}{\partial t} \tag{7.3}$$

$$\nabla \times \mathbf{E} = -\frac{\partial \mathbf{B}}{\partial t} \tag{7.4}$$

The electric field is solved based on the time-harmonic wave equation for linear media, given by:

$$\nabla \times (\mu_r^{-1} \nabla \times \mathbf{E}) - k_0^2 \varepsilon_r \mathbf{E} = 0 \qquad (7.5)$$

The relationship between the plasma current density and the electric field is described by:

$$\sigma^{-1} \cdot \mathbf{J} = \mathbf{E} \qquad (7.6)$$

Here, σ is the plasma conductivity tensor, and is a function of the electron density, collision frequency, and magnetic flux density. Heating of the gas is described by:

$$Q_h = \bar{\mathbf{J}} \cdot \bar{\mathbf{E}} \qquad (7.7)$$

The electrostatic field in dielectric materials is described by [158]:

$$-\nabla\left(\varepsilon_0 \nabla V_p - \mathbf{P}\right) = \rho_c \qquad (7.8)$$

For a wave heated discharge, a system of coupled PDEs is solved. The high frequency electric field is computed using [158, 159]:

$$\nabla \times (\mu_r^{-1} \nabla \times \mathbf{E}) - k_0^2 \left(\epsilon_r - \frac{j\sigma_c}{\omega\epsilon_0}\right) \mathbf{E} = 0 \qquad (7.9)$$

Additional information on microwave coupling and engineering can be found in Ref. [41, 160].

7.3.3 Species Modelling

After calculating the electromagnetic field distribution, the electron density is calculated. Electrons are generated by inelastic collisions between electrons and neutrals (Table 7.2),

129

and are lost by recombination at the reactor walls (Table 7.3), volume recombination and electron capture. Assuming M reactions contributing towards change in the electron density, and P inelastic collisions between electrons and neutral species, the electron source term, R_e, and the electron energy loss, R_ε, are calculated using Equations (7.10) and (7.11):

$$R_e = \sum_{j=1}^{M} x_j \, k_j N_n n_e \tag{7.10}$$

$$R_\varepsilon = \sum_{j=1}^{P} x_j k_j N_n n_e \Delta \varepsilon_j \tag{7.11}$$

Here, k_j is the rate coefficient for reaction j, given by Equation (7.12) and incorporates the collision cross-section data, $\sigma_j(\varepsilon)$.

$$k_j = \sqrt{\frac{2q}{m_e}} \int_0^\infty \varepsilon \sigma_j(\varepsilon) f(\varepsilon) d\varepsilon \tag{7.12}$$

More in-depth information on electron transport (drift diffusion) can be found in Appendix C (Electron Transport Theory & Plasma Reactor Theory).

The equations reported in Table 7.2 are used to model the plasma chemistry, using cross-section data [161, 162] and approximating the reaction constants.

Table 7.2: Model reactions and energies.

Argon Reactions	Type	$\Delta\varepsilon$ (eV)
$e + Ar \rightarrow e + Ar$	Elastic	0
$e + Ar \rightarrow e + Ar^*$	Excitation	11.5
$e + Ar^* \rightarrow e + Ar$	Super elastic	-11.5
$e + Ar \rightarrow 2e + Ar^+$	Ionisation	15.8
$e + Ar^* \rightarrow 2e + Ar^+$	Ionisation	4.24
$Ar^* + Ar^* \rightarrow e + Ar^+ + Ar^+$	Penning ionisation	-
$Ar^* + Ar \rightarrow Ar + Ar$	Quenching	-

Hydrogen Reactions	Type	$\Delta\varepsilon$ (eV)
$e + H_2 \rightarrow e + H_2$	Elastic	0
$e + H_2 \rightarrow e + H_2^*$	Excitation	10.45
$e + H_2 \rightarrow 2e + H_2^+$	Ionisation	15.43
$H_2^+ + H_2 \rightarrow H_3^+ + H$	Ionisation	-
$e + H_3^+ \rightarrow H_2 + H$	Recombination	0

The surface reactions, given in Table 7.3, are dependent on a probability coefficient, γ, set to unity.

Table 7.3: Surface reactions and sticking coefficients.

Surface Reactions	γ
$Ar^* \rightarrow Ar$	1
$Ar^+ \rightarrow Ar$	1
$H_2^+ \rightarrow H_2$	1
$H_2^* \rightarrow H_2$	1
$H_3^+ \rightarrow H_2 + H$	1

The deposition of SiC was modelled using Equation (7.13) given as:

$$CH_3SiCl_3(l) \rightarrow SiC(s) + 3HCl(g) \tag{7.13}$$
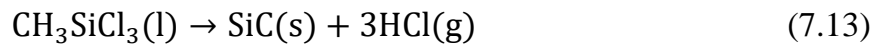
SiC is specified as the bulk species. Numerous studies have indicated that Equation (7.13) is not the main reaction path, but instead consists of various sub reactions, many of which are dependent on hydrogen concentration [163]. In this study, the deposition rate is modelled using a sticking coefficient, γ, as a function of temperature only. The hydrogen dependence is to be investigated in future modelling work. Deposition rates are modelled on the quartz tube walls as well as on the surface of a stationary particle placed within the plasma zone. The sticking coefficient and temperature is adjusted to coincide with deposition rates and temperatures observed during experimental runs [157].

7.3.4 Transfer Equations

General derivations of the equations describing conservation of momentum, energy and individual species, can be found in the literature [164-167]. The gas flow is assumed to be subsonic and laminar which reduces to the continuity equation given by Equation (7.14), representing the conservation of mass, and Equation (7.15), representing the conservation of momentum:

$$\frac{\partial \rho}{\partial t} + \nabla \cdot (\rho \mathbf{u}) = 0 \tag{7.14}$$

$$\rho \frac{\partial \mathbf{u}}{\partial t} + \rho (\mathbf{u} \cdot \nabla)\mathbf{u} = \nabla \cdot [-p\mathbf{I} + \tau] + \mathbf{F} \tag{7.15}$$

Here, $\mathbf{F}$ is the volume force vector representing the hydrostatic force within the bulk of the fluid. These equations are coupled to the energy balance:

$$\rho C_p \frac{dT}{dt} + \rho C_p \mathbf{u} \cdot \nabla T = \nabla \cdot (k_T \nabla T) + Q \tag{7.16}$$

Here, Q is defined as additional heat sources, other than viscous heating. For a reacting flow with k species and N reactions, the equation for the first $k - 1$ species is given by:

$$\rho \frac{\partial}{\partial t}(\omega_k) + \rho (\boldsymbol{u} \cdot \nabla)\omega_k = \nabla \cdot \mathbf{j}_k + R_k \tag{7.17}$$

where $\mathbf{j}_k$ is the diffusive flux of species k. The description is completed by the ideal gas law:

$$\frac{1}{M} = \sum_{k=1}^{Q} \frac{\omega_k}{M_k} \tag{7.18}$$

$$\rho = \frac{pM}{RT} \tag{7.19}$$

Transport properties (e.g. dynamic viscosities and diffusion coefficients) are described by the kinetic theory of gases, shown in Appendix C (Heavy Species Transport Theory).

7.3.5 Particle Tracing

To predict the movement of an alumina particle inside the reactor, a second model is developed. The gas velocity profile inside the reactor is first solved, and each time step solution is then applied to the particle's previous position and velocity conditions. The particle momentum is solved using Newton's second law, given as [168, 169]:

$$\frac{d}{dt}\left(m_p \mathbf{v_p}\right) = \mathbf{F}_D + \mathbf{F}_g + \mathbf{F}_{ext} \tag{7.20}$$

Here, $\mathbf{F}_D$, $\mathbf{F}_g$ and $\mathbf{F}_{ext}$ are the drag force, gravitational force, and external forces, respectively. Heating of the gas is facilitated by a heating zone to reduce computing time. The particle temperature is calculated through:

$$m_p C_p \frac{dT_p}{dt} = h_p A_p \left(T - T_p\right) \tag{7.21}$$

It is important to note that these differential equations only attempt to estimate the true system behaviour.

7.4   Modelling Software

The model was designed and solved using the finite element analysis software platform, COMSOL Multiphysics®, which incorporates coupled systems of partial differential equations (PDEs). The discretisation uses linear elements, which is computationally cheaper than higher-order elements, and less prone to spurious oscillations, effectively improving numerical robustness. The system is solved in the frequency-transient domain (2.45 GHz), using a backward differentiation formula (BDF) time stepping method, with an absolute tolerance of 5×10^{-4}. The COMSOL Multiphysics® module interaction is described in Figure 7.3. The computational hardware consisted of an Intel® Core™ i7 CPU @ 2.50 GHz, with 16 GB memory and 64-bit Windows 10 operating system. Graphical processing was performed using a GeForce GTX 860M display card.

7.5   Results and Discussions

7.5.1   Plasma Chemistry

Representative results of the electric field, electron/species number densities and electron temperatures in the reaction zone are shown in Figure 7.4. The electron number density (c) and temperatures (b) correspond to expected values [37, 170], reaching maximum values of 5.93×10^{19} m^{-3} and 1.22 eV, respectively. The critical electron density (a), indicated by a white outline, is indicative of the plasma zone where number densities exceed 7.6×10^{16} m^{-3}. The shape and position of the plasma, indicated in Figure 7.4, is in agreement with the experimental work that the model is based on [157], with the plasma height varying between 10 cm and 15 cm, depending on operating conditions.

135
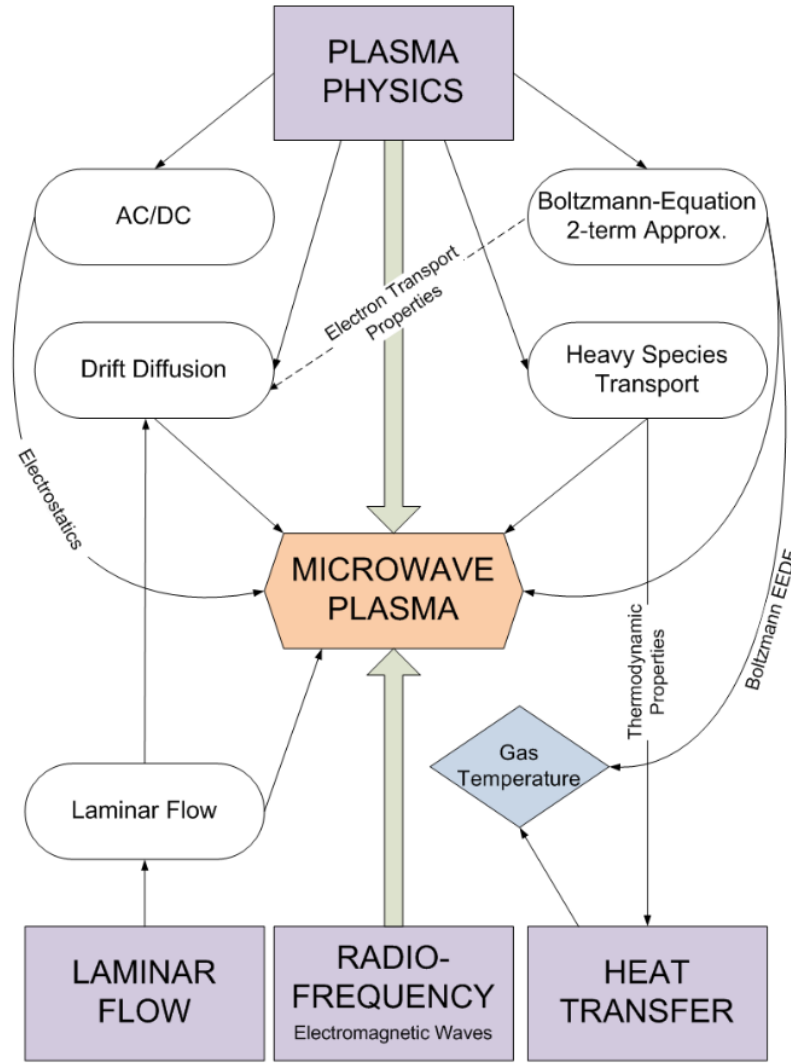
Figure 7.3: Microwave plasma model description.

The electric field is shown in Figure 7.4(a) and hints at the importance of positioning the quartz tube at the optimal position in relation to the wave amplitude, as geometric design plays a key role in resonance and plasma coupling [41]. Figure 7.4(d) and Figure 7.4(e) represent the ion number densities of Ar^+ and H_2^+, respectively, with maximum values reaching $\sim 10^{18}$ m^{-3} and $\sim 10^{15}$ m^{-3} compared to the much lower background values hovering at $\sim 10^9$ m^{-3}.
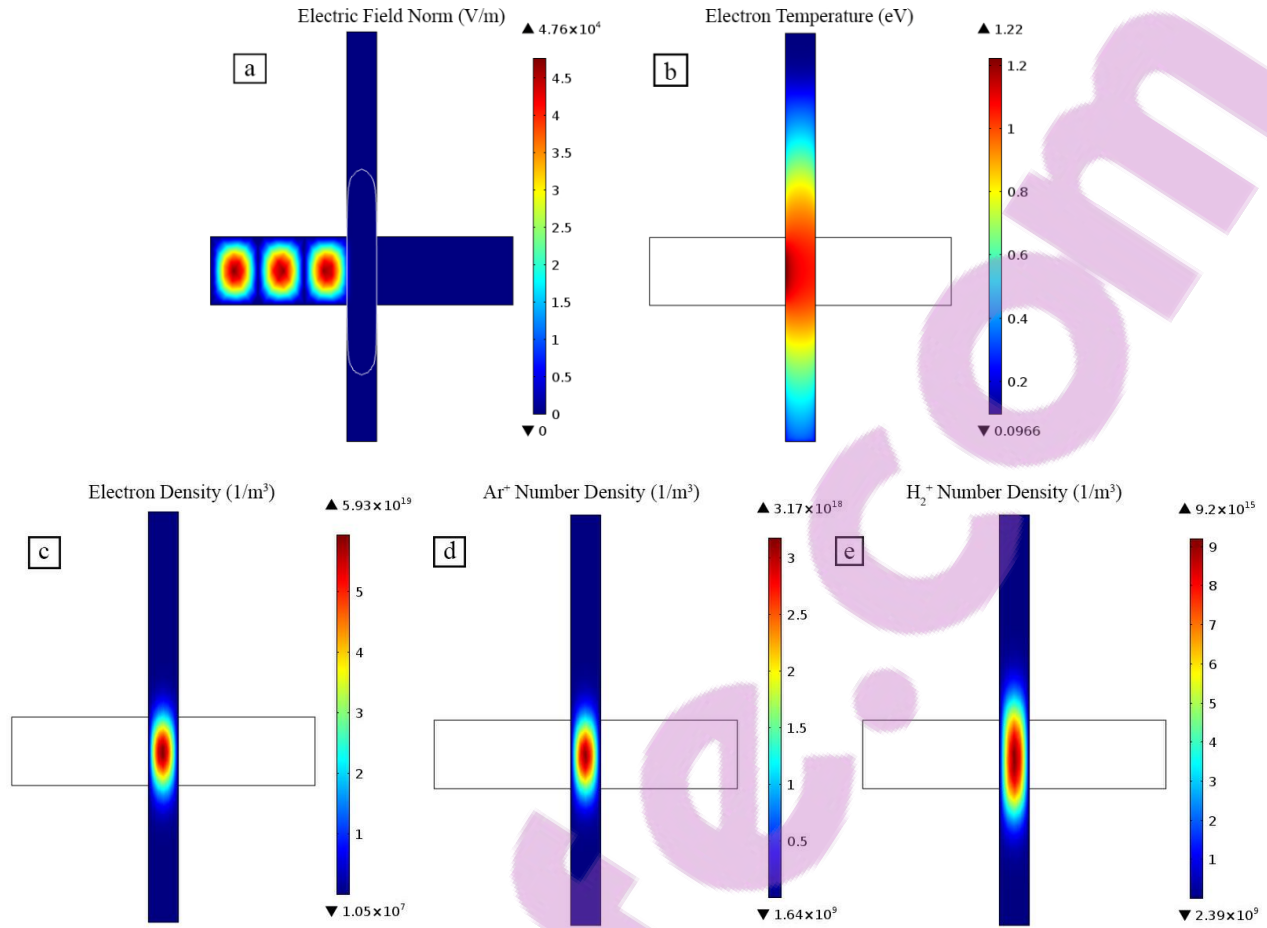
Figure 7.4: Plasma chemistry results.

7.5.2 Gas Heating and Density

Gas temperatures and densities are given in Figure 7.5. In-plane heat losses were specified on the quartz tube walls, with an emissivity, $\varepsilon_d = 0.6$, and ambient temperature, $T_{amb} = 298.15$ K. The resulting temperature profiles agree with experimentally observed temperature regimes (estimated at approximately 1 000 °C), and have been shown to vary with microwave power, hydrogen concentration and operating pressure [6, 67, 136]. The gas temperature is highest within the plasma zone, and accordingly the gas velocity increases within this area, and the density decreases. These large perturbances yield a

137

chaotic flow, increasing modelling complexity. The flow dynamics are further investigated under Section 7.6.4.
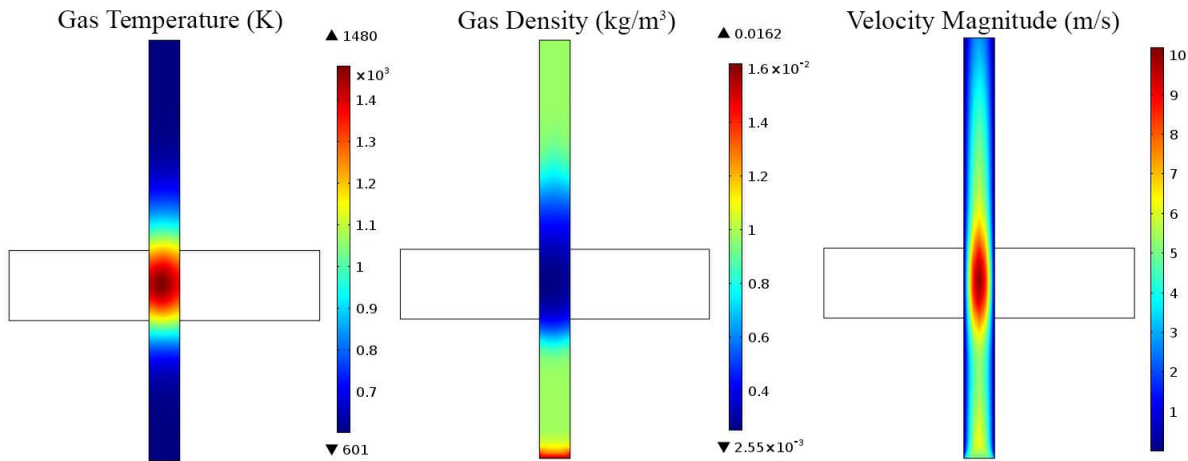
Figure 7.5: Gas temperature, density and velocity magnitude.

7.5.3 Chemical Vapour Deposition

The diffusion velocity from the quartz walls and the spherical particles (+/- x-direction), due to MTS decomposition, is represented in Figure 7.6. These represent the formation and diffusion of HCl from the reactor walls towards the centre of the reactor. The diffusion velocities are slightly asymmetric, with a higher velocity in the positive x-direction. These slight variations are due to the temperature gradient throughout the plasma zone, and accordingly result in varied deposition rates. Similar diffusion velocities are seen from the particle surface. These diffusion velocities appear more symmetric, although they are very sensitive to the position of the particle within the reactor.
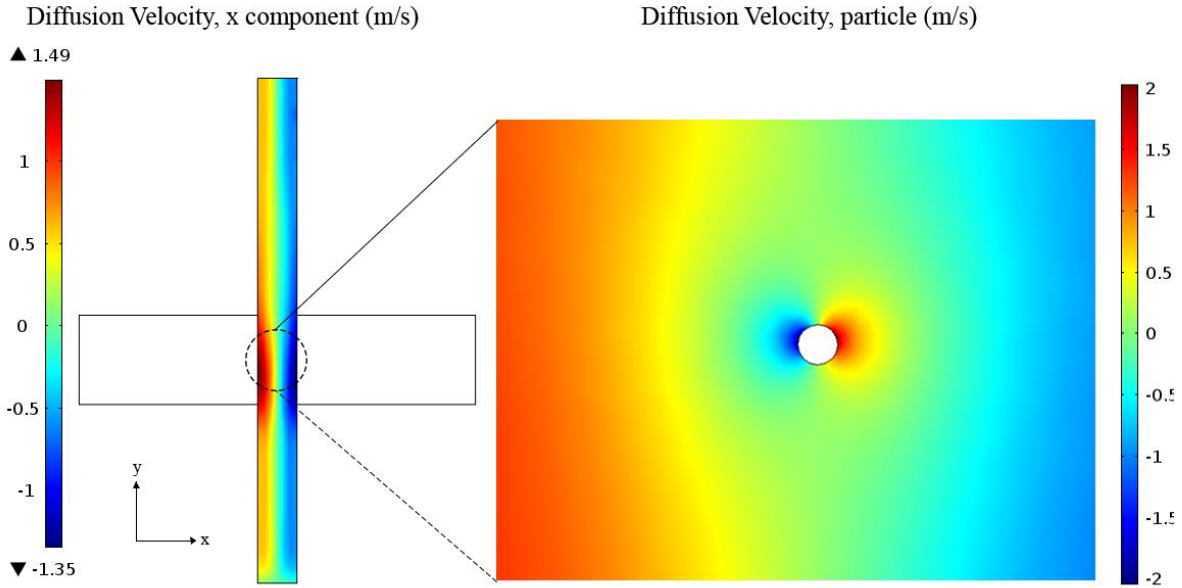
Figure 7.6: Diffusion velocities from the quartz walls (left) and particle surface (right, central zone around the sphere).

Additionally, the deposition of SiC on the quartz walls hinders the penetration of microwaves into the plasma zone, and this effect worsens with run time. It is expected that this additional growing layer consequently perturbs the mass deposition rate on the particles' surface [134, 135]. The effect is therefore investigated in this model by specifying a boundary layer on the quartz wall, with the parameters specified in Table 7.4.

Table 7.4: Boundary layer parameters, simulating a growing SiC layer.

Relative Permeability	Relative Permittivity	Electrical Conductivity (S/m)
9.7	1	10

The boundary thickness is correlated with the SiC layer thickness during the length of the run, and the resulting layer growth rates are shown in Figure 7.7.
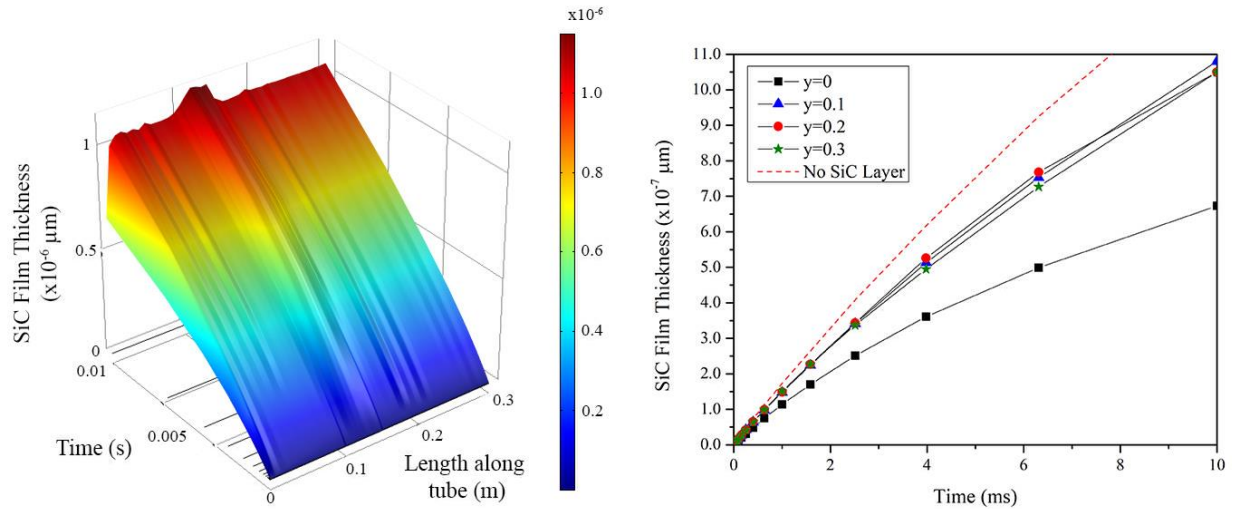
Figure 7.7: Height of SiC layer with run time.

Figure 7.7 (left) presents the layer thickness along the length of the tube, where $y = 0$ is situated at the inlet, and $y = 0.3$ is situated at the outlet. The figure indicates a slightly higher growth rate near the plasma zone ($y \approx 0.13$) as a result of the higher temperature gradient within this area. The growth rate is approximately $0.36 \, \mu m/h$, orders of magnitude lower than observed experimentally [157]. This considerable deviation is attributed to the lack of a complete MTS decomposition reaction scheme, as well as inaccurate sticking coefficient approximations. Adjusting these values, however, results in unstable numerical complications and is to be the focus of future work.

The effect of the boundary layer, however, is evident from Figure 7.7, as seen by the gradual decrease in the slope of the curve with run time. The layer thickness is shown in Figure 7.7 (right) at various points along the reactor length, as well as the predicted layer growth rate assuming it had no effect on the plasma chemistry. This effect was observed experimentally, and the results in Figure 7.7 help support the speculation that the increasing

SiC layer thickness on the quartz walls inhibits the plasma coupling, and consequently the deposition rates.

7.5.4 Spout Velocity and Particle Tracing

The effect of the spout geometry was also incorporated in an attempt to more accurately predict the movement of a particle through the plasma zone. Due to the high computational cost of the plasma chemistry, this was modelled by mimicking the plasma zone using a general heat source within the quartz tube ($P = 1\ 000$ W). The velocity streamlines are shown in Figure 7.8 and indicate the change in temperature as the gas flows upwards through the plasma zone.
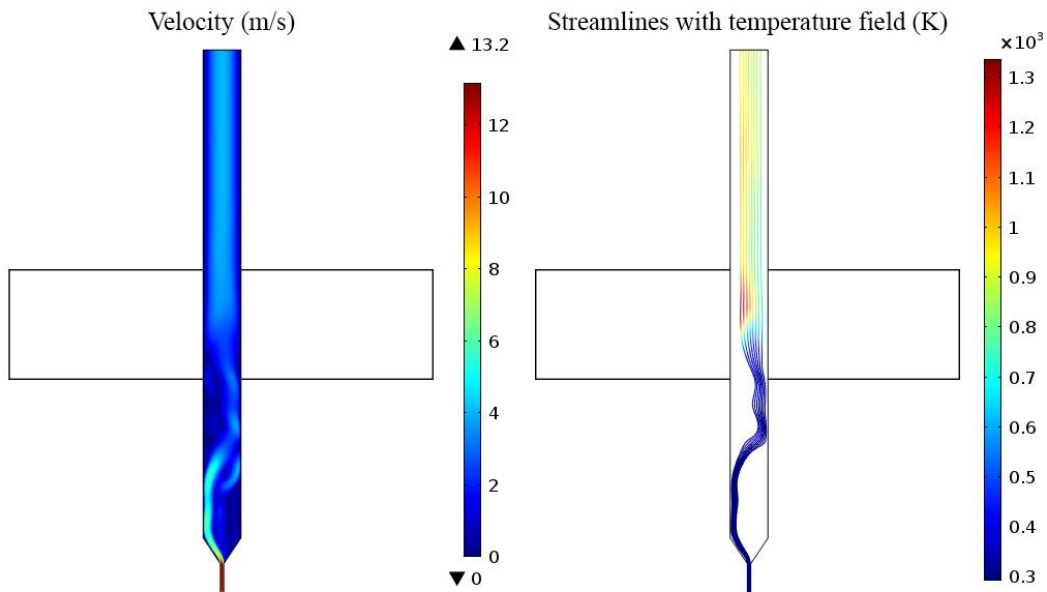
Figure 7.8: Effect of spout geometry on velocity profile.

The streamlines are indicated on the right, and appear to push up against the quartz tube in the section before the plasma heat source, creating "dead zones" in the lower part of the tube. This was observed experimentally, with alumina particles often stagnating in the

141

lower sections of the tube and nozzle. The streamlines become more diffuse with increasing temperature, moving upwards along straight flow lines. The alumina particle properties are defined in Table 7.5.

Table 7.5: Particle properties.

Density (kg/m^3)	Particle diameter (mm)	Specific Heat (J/(kg·K))	Latent Heat (kJ/kg)
3950	1.5	880	1360

The movement (specifically the variation in height) of a single particle is traced through the plasma, and is represented in terms of the change in y-coordinate in Figure 7.9 (black line, left axis). The plasma zone is represented between the horizontal lines at $y = 0.10$ and $y = 0.20$.

Integration of the curve between $y = 0.10$ and $y = 0.20$ yields the total travel time within the plasma zone. The particle resides approximately 40 % of its travel time within the plasma zone, i.e. approximately 8 minutes during a 20-minute run. Deposition onto the particle surface, however, is not limited to the time travelling through the plasma. The particle surface (substrate) temperature contributes greatly towards SiC deposition [6, 65], and the particle temperature stabilizes relatively quickly with the continuous exposure to the plasma. This is also indicated on Figure 7.9 (blue line, right axis) which shows the average particle temperature stabilizing after 1 second (approximately 11 passes through the plasma zone).
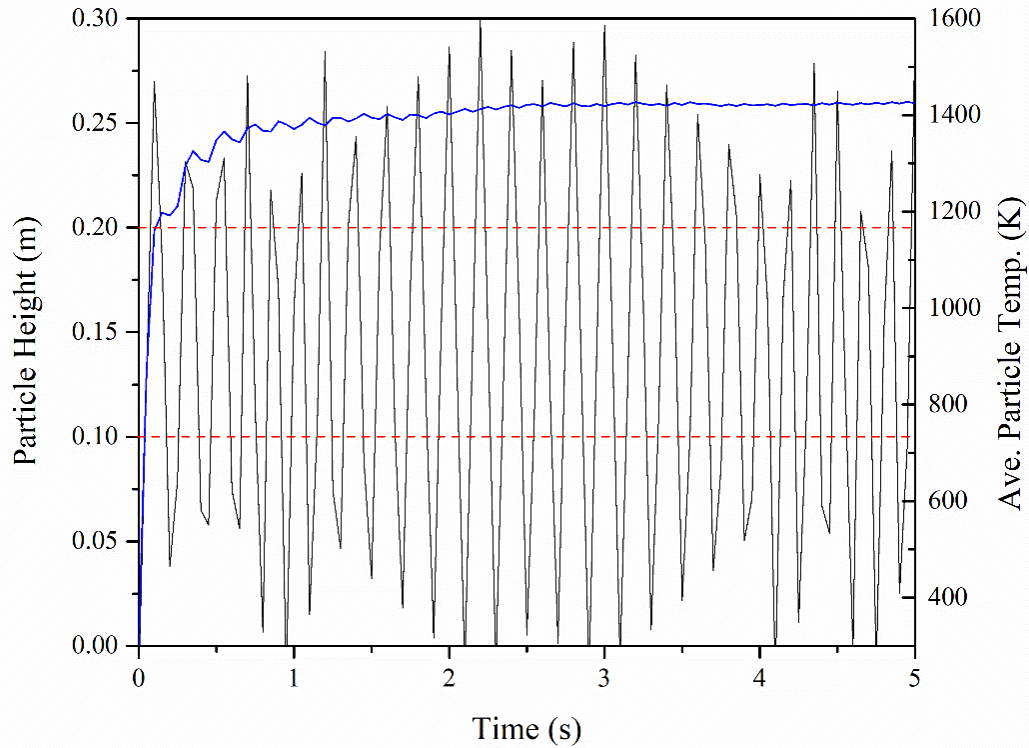
Figure 7.9: Particle position (y-coordinate) and temperature in the reactor with run time.

The presence of the particle also affects the plasma chemistry, as the particle surface acts as a wall boundary condition, where argon ions and excited argon atoms revert to neutral argon atoms. This effect is shown in Figure 7.10, indicating a drop in the electron density within the immediate volume surrounding the particle. The figure presents the movement of a particle upwards through the plasma.

This effect is short-lived for a single particle traveling through the plasma, however for the more realistic situation containing 50 to 100 particles, this effect is likely intensified with detrimental results such as decreased temperatures and deposition rates.

143
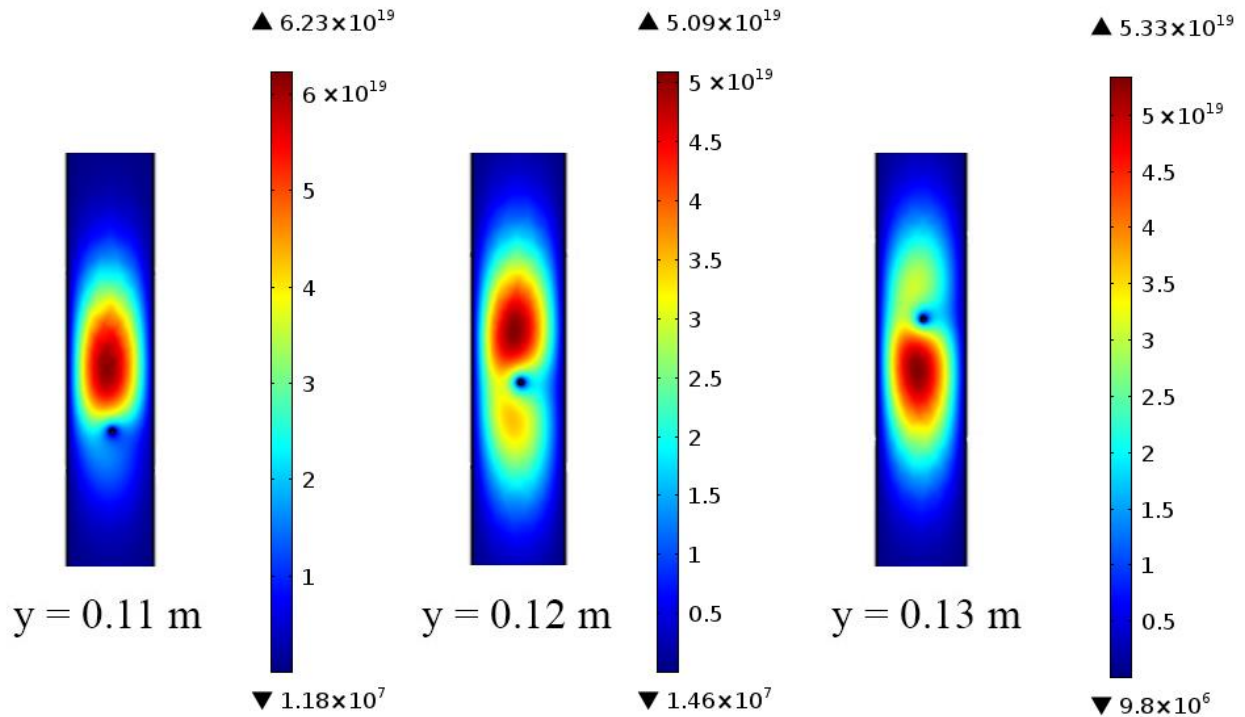
Figure 7.10: Effect of particle on electron density.

7.6 Summary

A 2D model has been developed, simulating a MW-PECVD process, based on the experimental work reported in Chapter 6. Modelled results include gas-phase species, electromagnetic phenomena, flow dynamics, heat transfer and particle behaviour. Results comparable with literature values include the electron densities (~ 5.93×10^{19} m^{-3}) and energies (~ 1.22 eV). Experimentally comparable results included the shape and position of the plasma, gas temperatures (~ 1 000 °C) and velocities, as well as the detrimental effect of a growing SiC layer on the quartz tube walls. It was also demonstrated that, in this 2D MW-PECVD model, the deposition rates of SiC were not within acceptable agreement with experimental results, likely due to the strong MW-particle interaction at relatively

large particle loading that tends to quench the plasma, decreasing the electron density and the plasma temperatures.

CHAPTER VIII:
CONCLUSIONS & RECOMMENDATIONS

147

8 Conclusions & Recommendations

8.1 Summary

SiC has gained increasing attention as a nuclear ceramic due to its advantageous thermal and mechanical properties, and stability under irradiated conditions. Many different synthesis methods for the deposition of SiC layers have been reported in the literature, however, a gap still exists in the literature focusing on the possible advantages of particle coating in a microwave plasma spouted bed reactor, specifically with regards to SiC deposition.

In this study, the synthesis and deposition of SiC layers in a MW-PECVD spouted bed reactor is reported, using MTS as precursor in an argon/hydrogen environment. The experimental work was performed using a microwave generator operating at 2.45 GHz, a 1 500 W power supply, and a waveguide with stub tuners and a sliding short. The plasma environment was initiated and maintained in a quartz tube. The DoE followed that of a 3D central composite design, and the parameters studied were absolute pressure (20 kPaa to 60 kPaa), H_2:MTS molar ratio (0 mol/mol to 10 mol/mol) and the total enthalpy (2.7 MJ/kg to 4.9 MJ/kg). Characterisation techniques used to investigate the SiC layer quality/composition included SEM, TEM, XRD, TGA, XPS and BET.

To better understand the system's various physical interactions, a 2D model was also produced, simulating the conditions of an experimental run. The model was produced using the finite elements software package COMSOL Multiphysics®, and couples various PDEs used to describe physical phenomena such as laminar flow, heat transfer, electron and heavy species transport, as well as microwave propagation and particle tracing.

8.2 Conclusions

Alumina particles were successfully coated with SiC layers in a microwave plasma-assisted spouted bed reactor. Growth rates varied from 50 μm/h to 140 μm/h, coinciding with mass deposition rates of 0.012 g/h to 0.208 g/h. The SiC layers were characterised using SEM, TEM, XRD, XPS, EDX and FTIR techniques, which assisted in developing a colour chart as well as a similar morphological chart used to indicate the change in morphology of the layers throughout the design space. High enthalpy and pressure values tended to produce darker coloured layers, often accompanied by carbon-rich deposits. XPS characterisation also indicated the presence of organosilicons, likely indicative of unreacted or partially reacted MTS compounds embedded in the layers. It is evident that within the design space, the optimal region for SiC deposition requires high enthalpy- (~ 5 MJ/kg) and pressure (> -60 kPag) conditions, with reasonable hydrogen-to-MTS ratios (~ 5:1). The quality (i.e. crystallinity, particle size, Si/C ratios) of the layers appears to improve at these conditions, at the expense of decreased deposition rates.

Heat treatment of the particles (1 000 °C in air) resulted in an increased O_2 content, likely due to the oxidation of the Si and organosilicons in the SiC layer. In contrast, the chlorine content decreased, indicative of the organosilicon reactions forming volatile HCl. SEM images showed that the layer boundaries became sharper and more defined after heat treatment. TGA results indicated an increase in mass of the SiC powders above 400 °C in an argon atmosphere. The result was confirmed using the same sample at a different facility using a different instrument. It is currently assumed that experimental error is the cause of this phenomenon.

The 2D model successfully couples various physical processes, such as laminar flow, heat treatment and plasma chemistry. Some results that coincide with experimental observations include:

- The shape and position of the plasma;

- gas temperatures (~ 1 000 °C);

- gas velocities (~ 2 m/s to 12 m/s); and

- the effect of a growing SiC layer on the reactor walls.

The deposition rates were not in agreement with experimental results, likely due to a simplified MTS decomposition mechanism, as well as the use of a temperature dependent sticking coefficient.

8.3 Recommendations

The conclusions demonstrate that use of the MW-PECVD technique, with the assistance of a spouted bed reactor, shows potential for the large-scale, low-cost coating of particles with SiC. Continued research towards optimal deposition parameters should include different substrate materials, varying plasma gasses, and mechanical testing of the layers (e.g. hardness tests). Additional heat treatment of the coated particles under inert conditions could contribute towards improvement of the layer quality for nuclear applications. Leach testing and irradiation tests are recommended before considering application for TRISO particles.

Further improvement of the 2D model is also recommended. This would entail expanding to a 3D model, and adjusting the operating parameters of the model up to atmospheric conditions, and higher MTS and hydrogen molar concentrations. The decomposition schema of MTS to form SiC should also be reconsidered.

REFERENCE LIST

9 Reference List

1. Harris, G., (1995), *Properties of Silicon Carbide*. London: INSPEC.

2. Saddow, S.E. and A. Agarwal, (2004), *Advances in Silicon Carbide Processing and Applications*. United States of America: ARTECH HOUSE, INC.

3. Katoh, Y., L. Snead, I. Szlufarska, and W. Weber, (2012), Radiation effects in SiC for nuclear structural applications. *Current Opinion in Solid State and Materials Science*. **16**(2012): p. 143-152.

4. Donald, I.W., B.L. Metcalfe and R.N.J. Taylor, (1997), The immobilization of high level radioactive wastes using ceramics and glasses. *Journal of Materials Science*. **32**(22): p. 5851-5887.

5. Rohbeck, N. and P. Xiao, (2016), Evaluation of the mechanical performance of silicon carbide in TRISO fuel at high temperatures. *Nuclear Engineering and Design*. **306**: p. 52-58.

6. Papasouliotis, G.D. and S.V. Sotirchos, (1999), Experimental study of atmospheric pressure chemical vapor deposition of silicon carbide from methyltrichlorosilane. *Journal of Materials Research*. **14**(8): p. 3397-3409.

7. Wang, X., K. Su, J. Deng, Y. Liu, Y. Wang, Q. Zeng, L. Cheng, and L. Zhang, (2011), Initial decomposition of methyltrichlorosilane in the chemical vapor deposition of silicon-carbide. *Computational and Theoretical Chemistry*. **967**(2–3): p. 265-272.

8. Sone, H., T. Kaneko and N. Miyakawa, (2000), In situ measurements and growth kinetics of silicon carbide chemical vapor deposition from methyltrichlorosilane. *Journal of Crystal Growth*. **219**(3): p. 245-252.

9. Dhage, S., H.C. Lee, M.S. Hassan, M.S. Akhtar, C.Y. Kim, J.M. Sohn, K.J. Kim, H.S. Shin, and O.B. Yang, (2009), Formation of SiC nanowhiskers by carbothermic reduction of silica with activated carbon. *Materials Letters*. **63**(2): p. 174-176.

10. Kelly, R., A. Miotello, D. Chrisey, and G. Hubler, (1994), Pulsed Laser Deposition of Thin Films. *by DB Chrisey and GK Hubler (Wiley, New York, 1994) p*. **55**.

11. Reitano, R. and P. Baeri, (1998), Pulsed laser deposition of crystalline silicon carbide films. *EPL (Europhysics Letters)*. **43**(5): p. 565.

12. Li, J., J. Tian and L. Dong, (2000), Synthesis of SiC precursors by a two-step sol–gel process and their conversion to SiC powders. *Journal of the European Ceramic Society*. **20**(11): p. 1853-1857.

13. Satapathy, L.N., P.D. Ramesh, D. Agrawal, and R. Roy, (2005), Microwave synthesis of phase-pure, fine silicon carbide powder. *Materials Research Bulletin*. **40**(10): p. 1871-1882.

14. Moshtaghioun, B.M., R. Poyato, F.L. Cumbrera, S. de Bernardi-Martin, A. Monshi, M.H. Abbasi, F. Karimzadeh, and A. Dominguez-Rodriguez, (2012), Rapid carbothermic synthesis of silicon carbide nano powders by using microwave heating. *Journal of the European Ceramic Society*. **32**(8): p. 1787-1794.

15. Huran, J., P. Boháček, V.N. Shvetsov, A.P. Kobzev, A. Kleinová, V. Sasinková, N.I. Balalykin, M. Sekáčová, and J. Arbet, Amorphous silicon carbide thin films deposited by plasma enhanced chemical vapor deposition at different temperature for hard environment applications, in *21st International Symposium on Plasma Chemistry*, A. von Keudell, *et al*., 2013: Queensland, Australia.

16. Károly, Z., I. Mohai, S. Klébert, A. Keszler, I.E. Sajó, and J. Szépvölgyi, (2011), Synthesis of SiC powder by RF plasma technique. *Powder Technology*. **214**(3): p. 300-305.

17. Sachdev, H. and P. Scheid, (2001), Formation of silicon carbide and silicon carbonitride by RF-plasma CVD. *Diamond and Related Materials*. **10**(3–7): p. 1160-1164.

18. Ko, S.M., S.M. Koo, W.S. Cho, K.T. Hwnag, and J.H. Kim, (2012), Synthesis of SiC nano-powder from organic precursors using RF inductively coupled thermal plasma. *Ceramics International*. **38**(3): p. 1959-1963.

19. Kim, B. and B.T. Lee, (2003), Effect of Plasma and Control Parameters on SiC Etching in a C2F6 Plasma. *Plasma Chemistry and Plasma Processing*. **23**(3): p. 489-499.

20. Lin, H., J.A. Gerbec, M. Sushchikh, and E.W. McFarland, (2008), Synthesis of amorphous silicon carbide nanoparticles in a low temperature low pressure plasma reactor. *Nanotechnology*. **19**(32): p. 325601.

21. Honda, S., Y. Baek, T. Ikuno, H. Kohara, M. Katayama, K. Oura, and T. Hirao, (2003), SiC nanofibers grown by high power microwave plasma chemical vapor deposition. *Applied Surface Science*. **212–213**: p. 378-382.

22. Tang, C., L. Fu, A.J.S. Fernandes, M.J. Soares, G. Cabral, A.J. Neves, and J. Grácio, (2008), Simultaneous formation of silicon carbide and diamond on Si substrates by microwave plasma assisted chemical vapor deposition. *New Carbon Materials*. **23**(3): p. 250-258.

23. van Laar, J.H., J.F.M. Slabber, J.P. Meyer, I.J. van der Walt, G.J. Puts, and P.L. Crouse, (2015), Microwave-plasma synthesis of nano-sized silicon carbide at atmospheric pressure. *Ceramics International*. **41**(3, Part B): p. 4326-4333.

24. Vennekamp, M., I. Bauer, M. Groh, E. Sperling, S. Ueberlein, M. Myndyk, G. Mäder, and S. Kaskel, (2011), Formation of SiC nanoparticles in an atmospheric microwave plasma. *Beilstein Journal of Nanotechnology*. **2**: p. 665-673.

25. Kaiser, M., K.M. Baumgärtner and A. Mattheus, (2012), Microwave Plasma Sources -Applications in Industry. *Contributions to Plasma Physics*. **52**(7): p. 629-635.

26. Knipping, J., H. Wiggers, B. Rellinghaus, P. Roth, D. Konjhodzic, and C. Meier, (2004), Synthesis of high purity silicon nanoparticles in a low pressure microwave reactor. *J Nanosci Nanotechnol*. **4**(8): p. 1039-44.

27. Vollath, D. and D.V. Szabó, (1998), Synthesis of nanocrystalline MoS_2 and WS_2 in a microwave plasma. *Materials Letters*. **35**(3): p. 236-244.

28. Hattori, Y., S. Nomura, S. Mukasa, H. Toyota, T. Inoue, and T. Kasahara, (2013), Synthesis of tungsten trioxide nanoparticles by microwave plasma in liquid and analysis of physical properties. *Journal of Alloys and Compounds*. **560**: p. 105-110.

29. Irzh, A., I. Genish, L. Klein, L.A. Solovyov, and A. Gedanken, (2010), Synthesis of ZnO and Zn Nanoparticles in Microwave Plasma and Their Deposition on Glass Slides. *Langmuir*. **26**(8): p. 5976-5984.

30. Karches, M., C. Bayer and P. Rudolf von Rohr, (1999), A circulating fluidised bed for plasma-enhanced chemical vapor deposition on powders at low temperatures. *Surface and Coatings Technology*. **116–119**: p. 879-885.

31. Shin, H.S. and D.G. Goodwin, (1994), Deposition of diamond coatings on particles in a microwave plasma-enhanced fluidized bed reactor. *Materials Letters*. **19**(3): p. 119-122.

32. Sathiyamoorthy, D., (2010), Plasma spouted/fluidized bed for materials processing. *Journal of Physics: Conference Series*. **208**(1): p. 120.

33. High Temperature Gas Cooled Reactor Fuels and Materials, in *IAEA TECDOC Series*. 2010, International Atomic Energy Agency: Vienna.

34. Chen, F.F., (2006), *Introduction to Plasma Physics and Controlled Fusion*. Springer.

35. Fridman, A., (2008), *Plasma Chemistry*. Cambridge University Press.

36. PPLATO. *PHYS 7.5: Kinetic theory - an example of microscopic modelling*. (1996) [21/09/2015]; Available from: http://www.met.reading.ac.uk/pplato2/index.html.

37. Tendero, C., C. Tixier, P. Tristant, J. Desmaison, and P. Leprince, (2006), Atmospheric pressure plasmas: A review. *Spectrochimica Acta Part B: Atomic Spectroscopy*. **61**(1): p. 2-30.

38. Francis, G., (1956), The glow discharge at low pressure. *Handbuch der physik*. **22**: p. 53-208.

39. Conrads, H. and M. Schmidt, (2000), Plasma generation and plasma sources. *Plasma Sources Science and Technology*. **9**(4): p. 441-454.

40. Fridman, A. and L.A. Kennedy, (2004), *Plasma Physics and Engineering*. Taylor & Francis.

41. Balanis, C.A., (2012), *Advanced Engineering Electromagnetics*. Wiley.

42. Marcuvitz, N., (1951), *Waveguide Handbook*. P. Peregrinus.

43. Vanderlinde, J., (2006), *Classical Electromagnetic Theory*. Springer Netherlands.

44. Orfanidis, S.J., (2008), *Electromagnetic Waves and Antennas*. Rutger: Rutgers University.

45. Whites, K.W. *EE 481/581 - Microwave Engineering, Fall 2015*. 2015 [15/04/2016]; Available from: http://whites.sdsmt.edu/.

46.   Golio, M., (2000), *The RF and Microwave Handbook*. CRC Press.

47.   Pozar, D.M., (1997), *Microwave Engineering*. Wiley.

48.   Zalach, J. and S. Franke, (2013), Iterative Boltzmann plot method for temperature and pressure determination in a xenon high pressure discharge lamp. *Journal of Applied Physics*. **113**(4): p. 043303.

49.   Merk, S., A. Demidov, D. Shelby, I. Gornushkin, I. Oanne, B. Smith, and N. Omenetto, (2013), Diagnostic of Laser-Induced Plasma Using Abel Inversion and Radiation Modeling. *Applied Spectroscopy*. **67**(8): p. 851-859.

50.   Ovsyannikov, A.A. and M.F. Zhukov, (2000), *Plasma Diagnostics*. Cambridge International Science Pub.

51.   Merlino, R.L., (2007), Understanding Langmuir probe current-voltage characteristics. *American Journal of Physics*. **75**(12): p. 1078-1085.

52.   Can, A., Densification, Microstructure and Properties of Liquid-phase Sintered Silicon Carbide Materials, in *Faculty of Science*. 2004, University of the Witwatersrand.

53.   van Laar, J.H., Microwave plasma synthesis of nano-sized silicon carbide at atmospheric pressure, in *Chemical Engineering*. 2015, University of Pretoria.

54.   Voice, E., The formation and structure of silicion carbide pyrolytically deposited in a fluidised bed of microspheres. 1971, Bath University of Technology.

55.   Baumann, H.N., (1952), The Relationship of Alpha and Beta Silicon Carbide. *Journal of The Electrochemical Society*. **99**(3): p. 109-114.

56.   Hull, D. and D.J. Bacon, (2011), *Introduction to Dislocations*. Vol. 1.

57.   Smith, Z., The fabrication of silicon carbide heating elements, in *Dept. of Civil Engineering* 1992, University of Cape Town.

58.   Bandyopadhyay, D., (2004), The Ti-Si-C system (Titanium-Silicon-Carbon). *Journal of Phase Equilibria and Diffusion*. **25**(5): p. 415-420.

59.   Patnaik, P., (2003), *Handbook of Inorganic Chemicals*. McGraw-Hill.

60.   Yaws, C.L., (2008), *Thermophysical Properties of Chemicals and Hydrocarbons*. Elsevier Science.

61.   Zinkle, S. and L. Snead, Thermophysical and mechanical properties of SiC/SiC composites. 1998, Oak Ridge National Lab., TN (United States).

62.   Andrievski, R.A., (2009), Nano-sized silicon carbide: synthesis, structure and properties. *Russian Chemical Reviews*. **78**(9): p. 821-831.

63.   Bechstedt, F., P. Käckell, A. Zywietz, K. Karch, B. Adolph, K. Tenelsen, and J. Furthmüller, (1997), Polytypism and Properties of Silicon Carbide. *Physica status solidi (b)*. **202**(1): p. 35-62.

64.   Izhevskyi, V.A., L.A. Genova, J.C. Bressiani, and A.H.A. Bressiani, (2000), Review article: silicon carbide. Structure, properties and processing. *Cerâmica*. **46**: p. 4-13.

65.   Chin, J., P.K. Gantzel and R.G. Hudson, (1977), The structure of chemical vapor deposited silicon carbide. *Thin Solid Films*. **40**(Supplement C): p. 57-72.

66.   Reznik, B., D. Gerthsen, W. Zhang, and K.J. Hüttinger, (2003), Microstructure of SiC deposited from methyltrichlorosilane. *Journal of the European Ceramic Society*. **23**(9): p. 1499-1508.

67.   Zhang, W.G. and K.J. Hüttinger, (2001), CVD of SiC from Methyltrichlorosilane. Part II: Composition of the Gas Phase and the Deposit. *Chemical Vapor Deposition*. **7**(4): p. 173-181.

68.   Neuhäuser, J., H. Plänitz and W. Wagner, (1994), Structural investigations of silicon-rich CVD-SiC. *Fresenius' Journal of Analytical Chemistry*. **349**(1): p. 162-163.

69.   Gupta, C.K. and D. Sathiyamoorthy, (1998), *Fluid Bed Technology in Materials Processing*. CRC Press.

70.   Deng, J., K. Su, X. Wang, Q. Zeng, L. Cheng, Y. Xu, and L. Zhang, (2009), Thermodynamics of the gas-phase reactions in chemical vapor deposition of silicon carbide with methyltrichlorosilane precursor. *Theoretical Chemistry Accounts*. **122**(1-2): p. 1-22.

71.   Ohshita, Y., A. Ishitani and T. Takada, (1991), Surface reaction mechanism of $SiCl_2$ with carrier gas H_2 in silicon vapor phase epitaxial growth. *Journal of Crystal Growth*. **108**(3): p. 499-507.

72.   Papasouliotis, G.D. and S.V. Sotirchos, *Gas-Phase and Surface Chemistry in Electronic Materials Processing. Materials Research Society Symposium Proceedings Held in Pittsburgh, PA*, T. Mountziaris, et al., Editors. 1994, Materials Research Society.

73.   Zhang, W.G. and K.J. Hüttinger, (2001), CVD of SiC from Methyltrichlorosilane. Part I: Deposition Rates. *Chemical Vapor Deposition*. **7**(4): p. 167-172.

74.   Loumagne, F., F. Langlais and R. Naslain, (1993), Kinetic laws of the chemical process in the CVD of SiC ceramics from CH_3SiCl_3-H_2 precursor. *J. Phys. IV France*. **03**(C3): p. C3-527-C3-533.

75.   Mousavipour, S.H., V. Saheb and S. Ramezani, (2004), Kinetics and Mechanism of Pyrolysis of Methyltrichlorosilane. *The Journal of Physical Chemistry A*. **108**(11): p. 1946-1952.

76.   Selvakumar, J. and D. Sathiyamoorthy, (2012), Prospects of chemical vapor grown silicon carbide thin films using halogen-free single sources in nuclear reactor applications: A review. *Journal of Materials Research*. **28**(1): p. 136-149.

77.   Federer, J., (1977), Parametric study of silicon carbide coatings deposited in a fluidized bed. *Thin Solid Films*. **40**: p. 89-96.

78. Kavecký, Š., B. Janeková, J. Madejová, and P. Šajgalík, (2000), Silicon carbide powder synthesis by chemical vapour deposition from silane/acetylene reaction system. *Journal of the European Ceramic Society*. **20**(12): p. 1939-1946.

79. Li, B., C. Zhang, H. Hu, and G. Qi, (2007), Preparation of nanosized silicon carbide powders by chemical vapor deposition at low temperatures. *Frontiers of Materials Science in China*. **1**(3): p. 309-311.

80. Graham, L., E. Voice and H. Brinkmann, Pyrolytic deposition process for applying a multi-layer coating to a nuclear fuel kernel, U.S.P. Office, Editor. 1973: Great Britain.

81. Nicholls, D.R., (2001), The Pebble Bed Modular Reactor : presentation and paper. *Transactions of the Royal Society of South Africa*. **56**(2): p. 125-130.

82. Fauchais, P., (2004), Understanding plasma spraying. *Journal of Physics D: Applied Physics*. **37**(9): p. R86-R108.

83. Tong, L. and R.G. Reddy, (2006), Thermal plasma synthesis of SiC nano-powders/nano-fibers. *Materials Research Bulletin*. **41**(12): p. 2303-2310.

84. Ishizaki, K., T. Egashira, K. Tanaka, and P.B. Celis, (1989), Direct production of ultra-fine nitrides (Si$_3$N$_4$ and AlN) and carbides (SiC, WC and TiC) powders by the arc plasma method. *Journal of Materials Science*. **24**(10): p. 3553-3559.

85. Inoue, Y., Y. Nariki and K. Tanaka, (1989), Mechanism of production of ultra-fine silicon carbide powder by arc plasma irradiation of silicon bulk in methane-based atmospheres. *Journal of Materials Science*. **24**(11): p. 3819-3823.

86. Taylor, P.R. and S.A. Pirzada, (1992), An investigation of silicon carbide synthesis in a nontransferred arc thermal plasma reactor. *Metallurgical Transactions B*. **23**(4): p. 443-451.

87. Hollabaugh, C.M., D.E. Hull, L.R. Newkirk, and J.J. Petrovic, (1983), R.F.-plasma system for the production of ultrafine, ultrapure silicon carbide powder. *Journal of Materials Science*. **18**(11): p. 3190-3194.

88. Guo, J.Y., F. Gitzhofer and M.I. Boulos, (1997), Effects of process parameters on ultrafine SiC synthesis using induction plasmas. *Plasma Chemistry and Plasma Processing*. **17**(2): p. 219-249.

89. Leconte, Y., M. Leparoux, X. Portier, and N. Herlin-Boime, (2008), Controlled Synthesis of β-SiC Nanopowders with Variable Stoichiometry Using Inductively Coupled Plasma. *Plasma Chemistry and Plasma Processing*. **28**(2): p. 233-248.

90. Zhu, C.W., G.Y. Zhao, V. Revankar, and V. Hlavacek, (1993), Synthesis of ultra-fine SiC powders in a d.c. plasma reactor. *Journal of Materials Science*. **28**(3): p. 659-668.

91. Oh, S., M. Cappelli and D. Park, (2002), Preparation of nano-sized silicon carbide powder using thermal plasma. *Korean Journal of Chemical Engineering*. **19**(5): p. 903-907.

92. Lee, W.E., M. Gilbert, S.T. Murphy, and R.W. Grimes, (2013), Opportunities for Advanced Ceramics and Composites in the Nuclear Sector. *Journal of the American Ceramic Society*. **96**(7): p. 2005-2030.

93. Wiss, T.A.G., J.P. Hiernaut, P.M.G. Damen, S. Lutique, R. Fromknecht, and W.J. Weber, (2006), Helium behaviour in waste conditioning matrices during thermal annealing. *Journal of Nuclear Materials*. **352**(1): p. 202-208.

94. Unites States Department of Energy. *A technology roadmap for generation IV nuclear energy systems* in *The US DOE Nuclear Energy Research Advisory Committee and the Generation IV International Forum*. 2002.

95. Jones, R.H., L. Giancarli, A. Hasegawa, Y. Katoh, A. Kohyama, B. Riccardi, L.L. Snead, and W.J. Weber, (2002), Promise and challenges of SiCf/SiC composites for fusion energy applications. *Journal of Nuclear Materials*. **307-311**: p. 1057-1072.

96. Kondo, S., M. Lee, T. Hinoki, Y. Hyodo, and F. Kano, (2015), Effect of irradiation damage on hydrothermal corrosion of SiC. *Journal of Nuclear Materials*. **464**: p. 36-42.

97. Van Rooyen, I., J. Neethling, A. Henry, and E. Janzen. *Influence of phosphorous and high temperature annealing on the nanostructures of 3C-SiC*. in *Fith International Topical Meeting on High Temperature Reactor Technology*. 2010. Prague, Czech Republic.

98. Swaminathan, N., P.J. Kamenski, D. Morgan, and I. Szlufarska, (2010), Effects of grain size and grain boundaries on defect production in nanocrystalline 3C–SiC. *Acta Materialia*. **58**(8): p. 2843-2853.

99. Shen, T.D., S. Feng, M. Tang, J.A. Valdez, Y. Wang, and K.E. Sickafus, (2007), Enhanced radiation tolerance in nanocrystalline $MgGa_2O_4$. *Applied Physics Letters*. **90**(26): p. 263115.

100. Vaßen, R. and D. Stöver, (2001), Processing and properties of nanophase non-oxide ceramics. *Materials Science and Engineering: A*. **301**(1): p. 59-68.

101. Mathur, K. and N. Epstein, (2012), *Spouted Beds*. Elsevier Science.

102. Mathur, K.B. and P.E. Gishler, (1955), A technique for contacting gases with coarse solid particles. *AIChE Journal*. **1**(2): p. 157-164.

103. Elperin, I., S. Zabrodsky, V. Yefremtsev, and V. Mikhailik, (1967), On the best construction of sets for spouting beds. *Collected Papers on "Intensification on Transfer of Heat and Mass in Drying and Thermal Processes", Nauka I Tekhnika BSSR, Minsk*. **323**.

104. Romankov, P. and N. Rashkovskaya, (1968), Drying in a suspended state. *Chem. Publ. House, Leningrad Branch*.

105. Manurung, F., Studies in the spouted bed technique with particular reference to its application to low temperature coal carbonization. 1964, University of New South Wales.

106. Ghosh, B., (1965), A study on the spouted bed, Part I. A theoretical analysis. *Indian Chem. Eng*. **1**: p. 16-19.

107. Smith, J. and K. Reddy, (1964), Spouting of mixed particle-size beds. *The Canadian Journal of Chemical Engineering*. **42**(5): p. 206-210.

108. Cowan, C., W. Peterson and G. Osberg, (1958), Spouting of large particles. *Eng. J*. **41**(5): p. 60-64.

109. Mathur, K.B. and P.E. Gishler, (1955), A study of the application of the spouted bed technique to wheat drying. *Journal of Applied Chemistry*. **5**(11): p. 624-636.

110. Berghel, J. and R. Renström, (2014), Superheated steam drying of sawdust in continuous feed spouted beds – A design perspective. *Biomass and Bioenergy*. **71**(Supplement C): p. 228-234.

111. Dotto, G.L., V.C. Souza and L.A.A. Pinto, (2011), Drying of chitosan in a spouted bed: The influences of temperature and equipment geometry in powder quality. *LWT - Food Science and Technology*. **44**(8): p. 1786-1792.

112. Pavarini, P.J. and J.R. Coury, (1987), Granulation of an insoluble powder in a spouted bed. *Powder Technology*. **53**(2): p. 97-103.

113. Eichner, E., V. Salikov, M. Dosta, S. Heinrich, and G.A. Schneider, (2016), Use of Spouted-Bed Spray Granulation Process for Fabrication of Metal/Ceramic-Polymer Composites. *Chemie Ingenieur Technik*. **88**(9): p. 1351-1351.

114. San José, M.J., S. Alvarez, I. García, and F.J. Peñas, (2014), Conical spouted bed combustor for clean valorization of sludge wastes from paper industry to generate energy. *Chemical Engineering Research and Design*. **92**(4): p. 672-678.

115. Kucharski, J. and A. Kmieć, (1989), Kinetics of granulation process during coating of tablets in a spouted bed. *Chemical Engineering Science*. **44**(8): p. 1627-1636.

116. Paulo Filho, M., S.C.S. Rocha and A.C.L. Lisboa, (2006), Modeling and experimental analysis of polydispersed particles coating in spouted bed. *Chemical Engineering and Processing: Process Intensification*. **45**(11): p. 965-972.

117. Saidutta, M.B. and D.V.R. Murthy, (2000), Mixing behaviour of solids in multiple spouted beds. *The Canadian Journal of Chemical Engineering*. **78**(2): p. 382-385.

118. Marshall, D.W., (2017), Spouted bed design considerations for coated nuclear fuel particles. *Powder Technology*. **316**(Supplement C): p. 421-425.

119. Kim, W.J., J.H. Park, J.Y. Park, Y.W. Lee, and J.H. Chang. *Effect of fluidized bed CVD condition on the microstructure of buffer layer in the TRISO coated particles*. in *Proceedings of the KNS spring meeting*. 2005. Korea, Republic of: KNS.

120. Beatty, R.L., F.A. Carlsen and J.L. Cook, (1965), Pyrolytic-Carbon Coatings on Ceramic Fuel Particles. *Nuclear Applications*. **1**(6): p. 560-566.

121. Bokros, J.C., (1965), The structure of pyrolytic carbon deposited in a fluidized bed. *Carbon*. **3**(1): p. 17-29.

122. Minato, K. and K. Fukuda, (1987), Chemical vapor deposition of silicon carbide for coated fuel particles. *Journal of Nuclear Materials*. **149**(2): p. 233-246.

123. López-Honorato, E., J. Tan, P.J. Meadows, G. Marsh, and P. Xiao, (2009), TRISO coated fuel particles with enhanced SiC properties. *Journal of Nuclear Materials*. **392**(2): p. 219-224.

124. Flamant, G., Plasma fluidized and spouted bed reactors: An overview, in *Pure and Applied Chemistry*. 1994. p. 1231.

125. Rykalin, N.N., *Plasma Engineering in Metallurgy and Inorganic Materials Technology A2 - Bell, A.T*, in *Plasma Chemistry–2: Plasma Chemistry and Transport Phenomena in Thermal Plasmas*, C. Bonet, Editor. 1976, Pergamon. p. 179-194.

126. Tsukada, M., K. Goto, R.H. Yamamoto, and M. Horio, (1995), Metal powder granulation in a plasma-spouted/fluidized bed. *Powder Technology*. **82**(3): p. 347-353.

127. Borer, B. and R. von Rohr, (2005), Growth structure of SiOx films deposited on various substrate particles by PECVD in a circulating fluidized bed reactor. *Surface and Coatings Technology*. **200**(1): p. 377-381.

128. Tap, R. and M. Willert-Porada, (2004), Dual PE-CVD circulating fluidized bed reactor. *IEEE Transactions on Plasma Science*. **32**(5): p. 2085-2092.

129. Matsukata, M., K. Suzuki, K. Ueyama, and T. Kojima, (1994), Development of a microwave plasma-fluidized bed reactor for novel particle processing. *International Journal of Multiphase Flow*. **20**(4): p. 763-773.

130. Bayer, C., M. Karches, A. Matthews, and P.R. von Rohr, (1998), Plasma Enhanced Chemical Vapor Deposition on Powders in a Low Temperature Plasma Fluidized Bed. *Chemical Engineering & Technology*. **21**(5): p. 427-430.

131. Chung, J., S. Kodama and H. Sekiguchi. *Preparation of Ni/γ-Al$_2$O$_3$ Catalyst Using Microwave Plasma Jet Combined with Spouted Bed*. in *23rd International Symposium on Plasma Chemistry*. 2017. Montréal, Canada: McGill.

132. Box, G.E.P., J.S. Hunter and W.G. Hunter, (2005), *Statistics for experimenters: design, innovation, and discovery*. Wiley-Interscience.

133. van Laar, J.H., H. Bissett, J.C. Barry, I.J. van der Walt, and P.L. Crouse, (2018), Deposition of SiC/Si coatings in a microwave plasma-assisted spouted bed reactor. *Journal of the European Ceramic Society*. **38**(4): p. 1197-1209.

134. Sugawara, H., K. Kashimura, M. Hayashi, S. Ishihara, T. Mitani, and N. Shinohara, (2014), Behavior of microwave-heated silicon carbide particles at frequencies of 2.0 - 13.5 GHz. *Applied Physics Letters*. **105**(3).

135. Isfort, P., T. Penzkofer, E. Pfaff, P. Bruners, R.W. Gunther, T. Schmitz-Rode, and A.H. Mahnken, (2011), Silicon carbide as a heat-enhancing agent in microwave ablation: in vitro experiments. *Cardiovasc Intervent Radiol*. **34**(4): p. 833-8.

136. Rusakov, G.V., L.A. Ivashchenko, V.I. Ivashchenko, and O.K. Porada, (2001), Peculiarities of preparing a-SiC:H films from methyltrichlorosilane. *Applied Surface Science*. **184**(1): p. 128-134.

137. Giesen, B., H. Wiggers, A. Kowalik, and P. Roth*, (2005), Formation of Si-nanoparticles in a microwave reactor: Comparison between experiments and modelling. *Journal of Nanoparticle Research*. **7**(1): p. 29-41.

138. Janzen, C., H. Wiggers, J. Knipping, and P. Roth, (2001), Formation and in situ sizing of gamma-Fe_2O_3 nanoparticles in a microwave flow reactor. *J Nanosci Nanotechnol*. **1**(2): p. 221-225.

139. Szabó, D., *Microwave Plasma Synthesis of Nanoparticles: From Theoretical Background and Experimental Realization to Nanoparticles with Special Properties*, in *Microwaves in Nanoparticle Synthesis*. 2013, Wiley-VCH Verlag GmbH & Co. KGaA. p. 271-309.

140. Fu, L., D.L. Johnson, J.G. Zheng, and V.P. Dravid, (2003), Microwave Plasma Synthesis of Nanostructured γ-Al_2O_3 Powders. *Journal of the American Ceramic Society*. **86**(9): p. 1635-1637.

141. Moulder, J.F. and J. Chastain, (1995), *Handbook of X-ray Photoelectron Spectroscopy: A Reference Book of Standard Spectra for Identification and Interpretation of XPS Data*. Minnesota USA: Physical Electronics.

142. Johansson, L.I., F. Owman and P. Mårtensson, (1996), High-resolution core-level study of 6H-SiC(0001). *Physical Review B*. **53**(20): p. 13793-13802.

143. Arezzo, F., E. Severini and N. Zacchetti, (1994), An XPS study of diamond films grown on differently pretreated silicon substrates. *Surface and Interface Analysis*. **22**(1-12): p. 218-223.

144. Chin, J., P.K. Gantzel and R.G. Hudson, (1977), The structure of chemical vapor deposited silicon carbide. *Thin Solid Films*. **40**: p. 57-72.

145. Bullot, J. and M.P. Schmidt, (1987), Physics of Amorphous Silicon–Carbon Alloys. *Physica status solidi (b)*. **143**(2): p. 345-418.

146. Demichelis, F., C.F. Pirri and E. Tresso, (1992), Influence of doping on the structural and optoelectronic properties of amorphous and microcrystalline silicon carbide. *Journal of Applied Physics*. **72**(4): p. 1327-1333.

147. Thommes, M., K. Kaneko, V. Neimark Alexander, P. Olivier James, F. Rodriguez-Reinoso, J. Rouquerol, and S.W. Sing Kenneth, Physisorption of gases, with special reference to the evaluation of surface area and pore size distribution (IUPAC Technical Report), in *Pure and Applied Chemistry*. 2015. p. 1051.

148. Rizk, S., M.B. Assouar, C. Gatel, M. Belmahi, J. Lambert, and J. Bougdira, (2008), Synthesis of carbon coated β-SiC nanofibers by microwave plasma assisted chemical vapour deposition in CH_4/H_2 gas mixture. *Diamond and Related Materials*. **17**(7–10): p. 1660-1665.

149.   Wrobel, A.M., A. Walkiewicz-Pietrzykowska and P. Uznanski, (2014), Remote hydrogen microwave plasma chemical vapor deposition from methylsilane precursors. 1. Growth mechanism and chemical structure of deposited a-SiC:H films. *Thin Solid Films*. **564**(0): p. 222-231.

150.   Rummel, P. and T.A. Grotjohn, (2002), Methods for modeling microwave plasma system stability. *Journal of Vacuum Science & Technology A: Vacuum, Surfaces, and Films*. **20**(2): p. 536-543.

151.   Füner, M., C. Wild and P. Koidl, (1999), Simulation and development of optimized microwave plasma reactors for diamond deposition. *Surface and Coatings Technology*. **116-119**(Supplement C): p. 853-862.

152.   Nad, S., Y. Gu and J. Asmussen, (2015), Determining the microwave coupling and operational efficiencies of a microwave plasma assisted chemical vapor deposition reactor under high pressure diamond synthesis operating conditions. *Review of Scientific Instruments*. **86**(7).

153.   Silva, F., K. Hassouni, X. Bonnin, and A. Gicquel, (2009), Microwave engineering of plasma-assisted CVD reactors for diamond deposition. *Journal of Physics: Condensed Matter*. **21**(36).

154.   Gorbachev, A.M., V.A. Koldanov and A.L. Vikharev, (2001), Numerical modeling of a microwave plasma CVD reactor. *Diamond and Related Materials*. **10**(3): p. 342-346.

155.   Yasaka, Y., N. Tobita and A. Tsuji, (2013), Control of plasma profile in microwave discharges via inverse-problem approach. *AIP Advances*. **3**(12).

156.   Meziere, J., M. Ucar, E. Blanquet, M. Pons, P. Ferret, and L. Di Cioccio, (2004), Modeling and simulation of SiC CVD in the horizontal hot-wall reactor concept. *Journal of Crystal Growth*. **267**(3): p. 436-451.

157.   van Laar, J.H., H. Bissett, J.C. Barry, I.J. van der Walt, and P.L. Crouse, (2017), Deposition of SiC/Si coatings in a microwave plasma-assisted spouted bed reactor. *Journal of the European Ceramic Society*.

158.   COMSOL Inc., Plasma Module User's Guide, v4.1. (2010).

159.   COMSOL Inc., R.F. Module User's Guide, v4.3. (2012).

160.   Collin, R.E., (1992), *Foundations for Microwave Engineering*. McGraw-Hill.

161.   COMSOL Inc., In-plane Microwave Plasma, v5.1.

162.   Yoon, J., M. Song, J. Han, S.H. Hwang, W. Chang, B. Lee, and Y. Itikawa, (2008), Cross Sections for Electron Collisions with Hydrogen Molecules. *Journal of Physical and Chemical Reference Data*. **37**(2): p. 913-931.

163.   Heinrich, J., S. Hemeltjen and G. Marx, (2000), Analytics of CVD Processes in the Deposition of SiC by Methyltrichlorosilane. *Microchimica Acta*. **133**(1): p. 209-214.

164.   Welty, J., C.E. Wicks, G.L. Rorrer, and R.E. Wilson, (2007), *Fundamentals of Momentum, Heat and Mass Transfer*. Wiley.

165.   Cengel, Y. and A. Ghajar, (2010), *Heat and Mass Transfer: Fundamentals and Applications*. McGraw-Hill Education.

166.   COMSOL Inc., (2013), COMSOL Multiphysics Reference Manual, v4.4.

167.   Tritton, D.J., (2012), *Physical Fluid Dynamics*. Springer Netherlands.

168.   COMSOL Inc., (2012), Particle Tracing Module User's Guide, v4.3.

169.   Coulson, J.M., J.F. Richardson, J.R. Backhurst, and J.H. Harker, (1996), *Coulson & Richardson's Chemical Engineering: Particle technology and separation processes. 5th ed*. Butterworth-Heinemann.

170.   Brown, P.G., T.J. Brotherton, J.M. Workman, and J.A. Caruso, (1987), Electron Number Density Studies in Moderate-Power Argon and Helium Microwave-Induced Plasmas. *Applied Spectroscopy*. **41**(5): p. 774-779.

171.   Bellan, P.M., (2008), *Fundamentals of Plasma Physics*. Cambridge University Press.

172.   Shkarofsky, I.P., T.W. Johnston and M.P. Bachynski, (1966), *The Particle Kinetics of Plasmas*. Addison-Wesley Pub. Co.

173.   Kee, R.J., M.E. Coltrin, P. Glarborg, and H. Zhu, (2017), *Chemically Reacting Flow: Theory, Modeling, and Simulation*. Wiley.

174.   Bird, R.B., W.E. Stewart and E.N. Lightfoot, (2007), *Transport Phenomena*. Wiley.

-

APPENDICES

Appendices

Appendix A: Classification of Ionisation and Dissociation Processes

The process of ionisation occurs when the energy transferred, $\Delta\epsilon$, to the valence electron of an atom or molecule exceeds the ionisation potential, I. Ionisation processes are subdivided into five different groups, each described briefly below, followed by a brief description of other relevant electron-ion reactions.

1. Direct Ionisation

Direct ionisation processes occur via impact with an electron whose energy is high enough to initiate ionisation in a single collision. It is the most important mechanism in cold or non-thermal plasmas where the electric fields and electron temperatures are quite high. The differential cross-section, σ_i, of incident electrons is described by the Rutherford formula [35]:

$$d\sigma_i = \frac{1}{(4\pi\epsilon_0)^2} \frac{\pi e^4}{\epsilon(\Delta\epsilon)^2} \, d(\Delta\epsilon) \tag{A.1}$$

Here, ϵ_0 is the permittivity of a vacuum, e is the electron charge, and ϵ is the energy of the incident electron. When $\Delta\epsilon \geq I$ direct ionisation will take place. Integration of Equation (A.1) gives the Thomson formula:

$$\sigma_i = \frac{1}{(4\pi\epsilon_0)^2} \frac{\pi e^4}{\epsilon} \left(\frac{1}{I} - \frac{1}{\epsilon} \right) \tag{A.2}$$

and when taking into account the kinetic energy of the valence electron, ϵ_v

$$\sigma_i = \frac{1}{(4\pi\epsilon_0)^2} \frac{\pi e^4}{\epsilon} \left(\frac{1}{\epsilon} - \frac{1}{I} + \frac{2\epsilon_v}{3} \left(\frac{1}{I^2} - \frac{1}{\epsilon^2} \right) \right) \tag{A.3}$$

The ionisation rate coefficient, k_i, is calculated by integration of σ_i over the EEDF and given by:

$$k_i = \sqrt{\frac{8T_e}{\pi m}} \sigma_0 \exp\left(-\frac{I}{T_e} \right) \tag{A.4}$$

Here, σ_0 is the geometric atomic cross-section given by:

$$\sigma_0 = \frac{Z_v \pi e^4}{I^2 (4\pi\epsilon_0)} \tag{A.5}$$

Here, Z_v is the number of valence electrons in the atom. For nitrogen and argon, $\sigma_0 \sim 10^{-6} \text{cm}^2$, and $3 \times 10^{-16} \text{cm}^2$ respectively [35].

Non-dissociative ionisation of molecules by electron impact occurs via Equation (A.6).

$$e + AB \rightarrow AB^+ + e + e \tag{A.6}$$

This process takes place when the electron energy does not greatly exceed that of the ionisation potential. The fastest internal motion of atoms inside molecules is that of vibration with typical time periods of $10^{-14} - 10^{-13}$ s. This is much longer than the typical interaction times between electrons and molecules ($10^{-16} - 10^{-15}$ s). Therefore atoms inside the molecule are considered to be frozen during this process of electronic transition. This is known as the Frank-Condon principle [35].

167

Non-dissociative ionisation of molecules requires a little more energy than the corresponding atomic ionisation. However, when $T_e \gg I$, **dissociative ionisation** can take place.

$$e + AB \rightarrow A + B^+ + e + e \tag{A.7}$$

This corresponds to electronic excitation into a repulsive state of the ion (AB+)* followed by its decay into an atom and ion [35].

2. Stepwise Ionisation

Stepwise ionisation also occurs via electron impact but entails the ionisation of previously excited neutral species. It is most important in thermal plasmas where the degree of ionisation and the concentration of excited neutrals are high.

The energy for ionisation can be provided in two different ways, namely:

- Plasma electrons
- Energy of excited neutrals which is converted for ionisation

The latter process being the main mechanism during stepwise ionisation [35]. This process can be much faster than direct ionisation when $T_e \ll I$. Several steps are involved before the ionisation event. Some of these steps include:

- Electron-neutral collisions which prepare excited species.
- The final collision with a relatively low-energy electron which leads to ionisation.

The stepwise ionisation rate coefficient, k_i^s, is found by summation of the partial rate coefficients corresponding to all states of excitation, n.

$$k_i^s = \sum_n k_i^{s,n} N_n(\epsilon_n)/N_0 \tag{A.8}$$

Here

- N_n is the number density of the excited species;
- N_0 is the number density of the gas; and
- n is the principal quantum number.

The ratio of rate coefficients for competing ionisation processes is then given by:

$$\frac{k_i^s}{k_i} \approx \left(\frac{I}{T_e}\right)^{\frac{7}{2}} \tag{A.9}$$

For typical plasmas with $I/T_e \sim 10$, stepwise ionisation can be $10^3 - 10^4$ times faster than direct ionisation [35].

3. Ionisation by heavy particle collision

Ionisation through collisions with heavy particles mostly involves ion-molecule or ion-atom collisions, as well as collisions of excited species. Even when heavy particles have enough kinetic energy for ionisation, they are unable to transfer this energy for ionisation due to their low velocities when compared to those of electrons in atoms. This slow motion is termed adiabatic. The kinetic energy of the colliding heavy particle has to be $10 - 100$ keV, which is much higher than the ionisation potential [35].

If the electronic excitation energy of the atom exceeds the ionisation potential of another atom, their collision can lead to ionisation, known as Penning Ionisation. Typical energy

169

values at which Penning ionisation may occur for neon and argon atoms are 16.6 and 15.8 eV [35].

4. Photo-ionisation

Collisions of neutrals with photons could result in an electron-ion pair. This process is important in thermal plasmas. The process of photo-ionisation is described by:

$$h\omega + A \rightarrow A^+ + e \qquad (A.10)$$
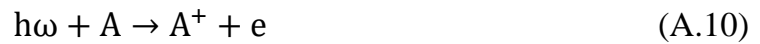
The photon wavelength is usually less than 1 000 Å (in the ultraviolet spectrum). Some photo ionisation cross sections for certain atoms and molecules are shown in Table A.1 [35].

Table A.1: Photo-ionisation cross sections [35].

Atoms or molecules	Wavelength λ, Å	Cross sections, cm^2	Atoms or molecules	Wavelength λ, Å	Cross sections, cm^2
Ar	787	$3.5 \cdot 10^{-17}$	Ne	575	$0.4 \cdot 10^{-17}$
N_2	798	$2.6 \cdot 10^{-17}$	O	910	$0.3 \cdot 10^{-17}$
N	482	$0.9 \cdot 10^{-17}$	O_2	1020	$0.1 \cdot 10^{-17}$
He	504	$0.7 \cdot 10^{-17}$	Cs	3185	$2.2 \cdot 10^{-19}$
H_2	805	$0.7 \cdot 10^{-17}$	Na	2412	$1.2 \cdot 10^{-19}$
H	912	$0.6 \cdot 10^{-17}$	K	2860	$1.2 \cdot 10^{-20}$

The most important role of this process is supplying the seed electrons for subsequent ionisation processes.

5. Surface ionisation (electron emission)

Surface ionisation occurs via electron, ion and photon collisions with different surfaces or simply by surface heating. Surface-related ionisation processes are important in electric current support, cathode layers and aerosol-based plasma systems. The most important surface ionisation process is that of thermionic emission, which is the emission of an electron from high-temperature metal surfaces due to the high thermal energy of the electrons [35]. Emitted electrons can stay in the vicinity of the surface and create negative space charge which will prevent further electron emission. The electric field in the cathode vicinity is sufficient to remove the negative space and reach the saturation current density, j, given by the Sommerfeld formula:

$$j = \frac{4\pi m e}{(2\pi h)^3} T^2 (1 - R) \exp\left(-\frac{W}{T}\right) \qquad (A.11)$$

Here the work function, W, is the minimum energy needed to extract an electron from the metal surface. R is a quantum mechanical coefficient describing the reflection of electrons from the potential barrier at the metal surface, and h is the Planck constant. Some values are given for the work function in Table A.2.

Table A.2: W values for different materials [35].

Material	C	Cu	Al	Mo
Work function	4.7 eV	4.4 eV	4.25 eV	4.3 eV
Material	W	Pt	Ni	W/ThO$_2$
Work function	4.54 eV	5.32 eV	4.5 eV	2.5 eV

Electron emission from solids due to the surface bombardment by different particles is called secondary electron emission. Secondary electron-electron emission, therefore, is

electron emission from a surface due to electron impact. Electron emission is usually characterized by a multiplication coefficient, γ_e, which is an indication of the number of emitted electrons produced by the initial electron. γ_e is dependent on the incident electron energy, shown in Figure A.1 [35].
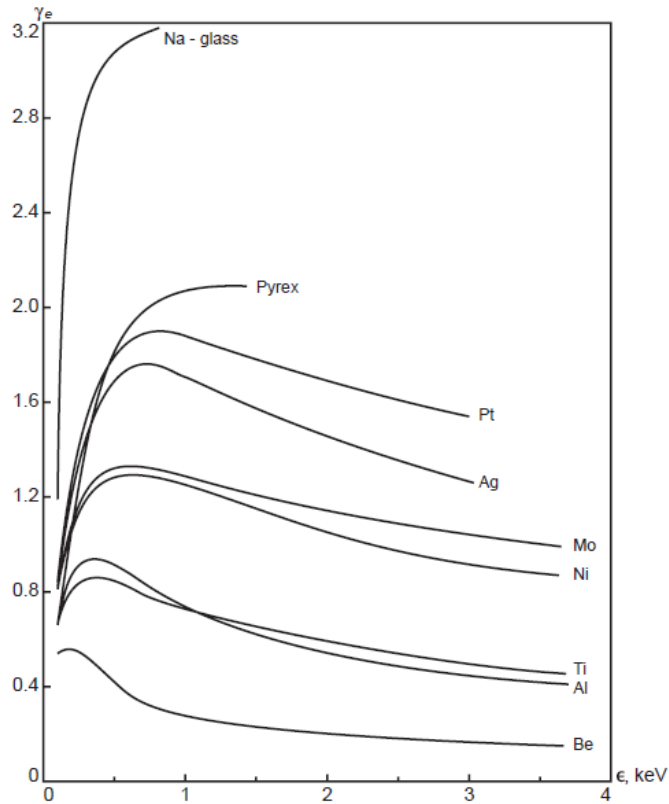
Figure A.1: Secondary electron emission for materials [35].

6. Plasma-Chemical Reactions of Positive Ions

Positive ion interactions have a major influence on plasma-chemical processes. This is because their reactions with neutrals are exothermic and usually require no activation energy, the positive ions can have significant kinetic energy, and electron-ion recombination is also a highly exothermic reaction. The latter process can occur through three different mechanisms resulting in recombination [35].

7. Dissociative Electron-Ion Recombination

The fastest electron neutralization mechanism. Presented as:

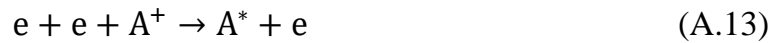$$e + AB^+ \rightarrow (AB)^* \rightarrow A + B^* \qquad (A.12)$$

This process is most common in molecular gases, but also important for atomic gases.

8. Three-body Electron-ion Recombination

This is the main recombination mechanism in atomic gases in the absence of molecular gases.

$$e + e + A^+ \rightarrow A^* + e \qquad (A.13)$$

9. Radiative Electron-ion Recombination

Recombination energy is converted into radiation in the following process:

$$e + A^+ \rightarrow A^* \rightarrow A + h\omega \qquad (A.14)$$

The cross section of this process is low, but can compete with three-body recombination when the plasma density is low.

10. Negative Ion Reactions

It is important to note that molecular gases with high electron affinities can form negative ions as such:

$$e + AB \rightarrow (AB^-)^* \rightarrow A + B^- \qquad (A.15)$$
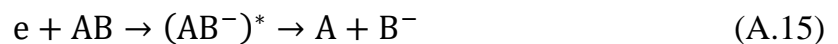
This can have a significant influence on plasma-chemical reactions. Loss of charged particles in electronegative gases is mostly due to ion-ion recombination which is the neutralization of positive and negative ions in binary or three-body collisions. Ion-ion recombination, however, occurs through different mechanisms, which are determined by different pressure ranges. These are usually characterised by very high rate coefficients [35].

11. Dissociation of Molecules by Electron Impact

Electron impact is able to initiate the dissociation of molecules by vibrational and electronic excitation. This dissociation process can proceed through numerous different mechanisms [35], some of which are described below and illustrated in Figure A.2.

11.1 Mechanism A

This mechanism starts with direct electronic excitation from the ground state to a repulsive one, and results in dissociation. The associated electron energy can greatly exceed dissociation energy. This process generates hot neutral fragments which can affect surface chemistry in low-pressure non-thermal plasmas.

11.2 Mechanism B

This second mechanism is initiated through direct electronic excitation from the ground state to an attractive state (discussed by Fridman [35]), with associated energies exceeding the dissociation threshold, and results in dissociation. The energies of the fragments are lower than those of mechanism A.

11.3 Mechanism C

The third mechanism occurs through direct electronic excitation from the ground state to an attractive state. Further excitation of this state leads to a radiative transition to a low-energy repulsive state. The energies of fragments are similar to those of mechanism A.

11.4 Mechanism D

This also starts with direct electronic excitation from the ground state to an attractive state. Further excitation of this state results in radiationless transfer to a highly repulsive state. Subsequently, dissociation results into electronically excited fragments, usually referred to as pre-dissociation.

11.5 Mechanism E

The fifth mechanism discussed here again starts with direct electronic dissociation from the ground state to a repulsive state, and then dissociates into electronically excited fragments. This mechanism requires the highest values of electron energies to occur.
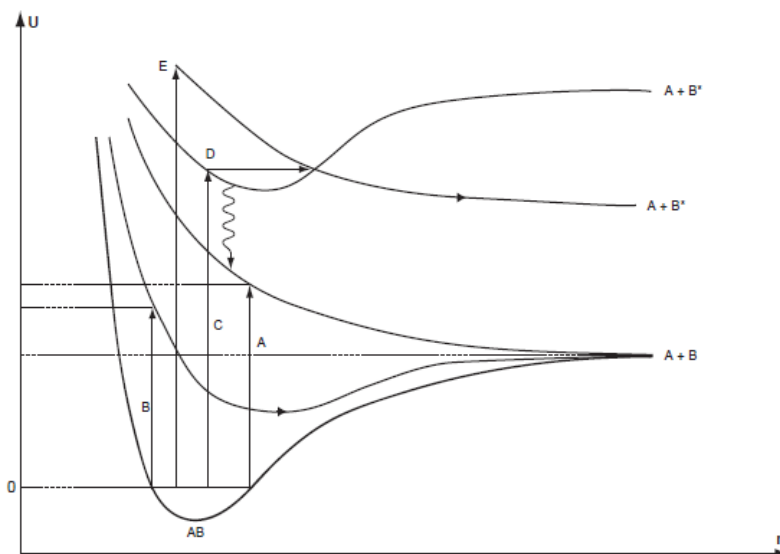

Figure A.2: Mechanisms of dissociation of molecules [35].

Appendix B: Elastic/Inelastic Collision Parameters

The elastic and inelastic processes can be described by six collision parameters [35]:

1. **Cross section, σ**

   This parameter can be described by an imaginary circle moving with its collision partners. If the centre crosses the circle of another collision partner, a reaction takes place, illustrated in Figure B.1.
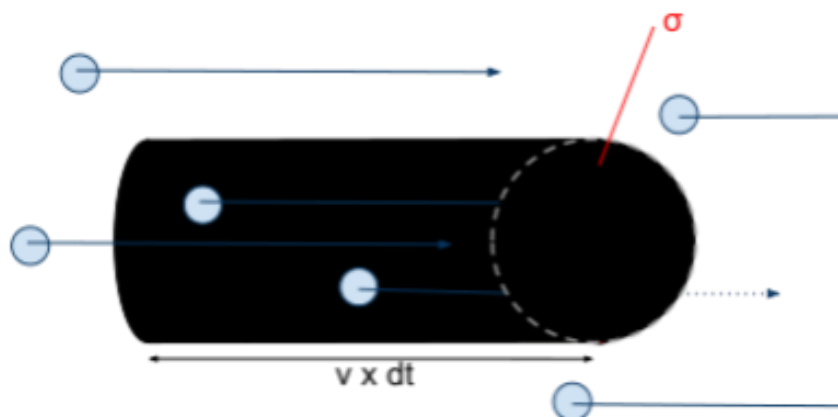

Figure B.1: Visualization of the cross section.

2. **Probability**

   Defined as the ratio of inelastic to elastic cross sections under the same conditions.

3. **Mean free path, λ_{mfp}**

   For a reaction, $A + B \rightarrow AB$, the mean free path of A is calculated by:

$$\lambda_A = 1/n_B \sigma_A \qquad (B.1)$$

   This concept is illustrated in Figure B.2.
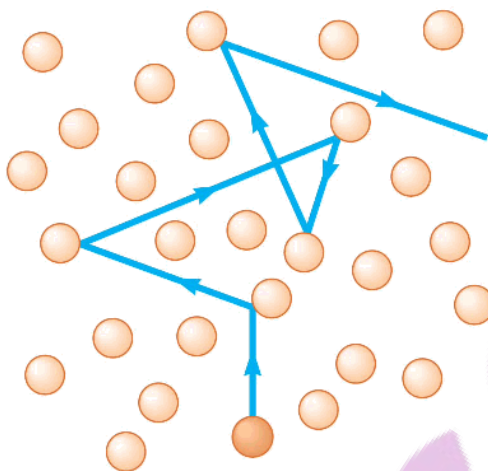
Figure B.2: Concept of mean free path.

4. Interaction/collision frequency, υ

Defined as the ratio of the relative velocities, v, of A and B, to the mean free path.

$$\upsilon_A = n_B \sigma_A v \tag{B.2}$$

5. Reaction rate

Number of processes, w, taking place per unit volume per unit time.

$$w_{A+B} = \upsilon_A n_A = \langle \sigma \upsilon \rangle n_A n_B \tag{B.3}$$

6. Reaction rate coefficient

The factor $\langle \sigma \upsilon \rangle$ is called the reaction rate coefficient. It is an integral factor, includes information on energy distribution functions and depends on the temperatures or mean energies of the collision partners.

Appendix C: Domain Equations used in Microwave Plasma Modelling

1. Electron Transport Theory

Electron transport is described by approximating the Boltzmann equation using two fluid equations, which then describe the electron number density and the mean electron energy as functions of geometry and time. The derivation and form of the relevant equations are as set out in Ref. [158]. The electron number density and electron energy density are calculated using Equations (C.1) and (C.2).

$$\frac{\partial}{\partial t}(n_e) + \nabla \cdot \Gamma_e = R_e - (\mathbf{u} \cdot \nabla)n_e \qquad \text{(C.1)}$$

$$\frac{\partial}{\partial t}(n_\varepsilon) + \nabla \cdot \Gamma_\varepsilon + \mathbf{E} \cdot \Gamma_e = R_\varepsilon - (\mathbf{u} \cdot \nabla)n_\varepsilon \qquad \text{(C.2)}$$

where $\Gamma_e = -(\mu_e \cdot \mathbf{E})n_e - \mathbf{D}_e \cdot \nabla n_e$ and $\Gamma_\varepsilon = -(\mu_\varepsilon \cdot \mathbf{E})n_\varepsilon - \mathbf{D}_\varepsilon \cdot \nabla n_\varepsilon$

Here, the subscripts e and ε denotes *electron number* and electron *energy*, respectively. Additionally, n is the number density, μ is the mobility, $\mathbf{E}$ is the electric field, $\mathbf{D}$ is the diffusivity, and $\mathbf{u}$ is the neutral gas velocity vector, however this term is usually negligible. Due to the instability of the electron number density in the plasma sheath region, the logarithms of Equations (C.1) and (C.2) are solved for, which allows for a more stable numerical solution.

The mean electron energy, $\bar{\varepsilon}$ and electron temperature, T_e, are computed using Equations (C.3) and (C.4).

$$\bar{\varepsilon} = \frac{n_\varepsilon}{n_e} \qquad \text{(C.3)}$$

$$T_e = \frac{2}{3}\bar{\varepsilon} \tag{C.4}$$

Additional information on electron transport theory can be found in Ref. [171, 172].

2. Heavy Species Transport Theory

A plasma's behaviour is dominated by the chemical kinetics rather than diffusive transport [158, 173]. This allows the use of a less rigorous formulation of the Maxwell-Stefan equations. For a reacting flow with Q species and N reactions, the equation for the first $Q - 1$ species is given by:

$$\rho \frac{\partial}{\partial t}(\omega_k) + \rho(\boldsymbol{u} \cdot \nabla)\omega_k = \nabla \cdot \mathbf{j}_k + R_k \tag{C.5}$$

where $\mathbf{j}_k$ is the diffusive flux of species k and is a function of the Maxwell-Stefan diffusivities. R_k is the rate expression, ρ is the density of the mixture and ω_k is the mass fraction. Some other useful quantities used for heavy species transport are summarised in Table C.1.

Table C.1: Summary of useful quantities used in heavy species transport.

Quantity	Symbol	Equation	
Mole average molecular weight	M	$\dfrac{1}{M} = \displaystyle\sum_{k=1}^{Q} \dfrac{\omega_k}{M_k}$	(C.6)
Mole fraction of species k	y_k	$\dfrac{\omega_k}{M_k} M$	(C.7)
Number density of species k	n_k	$\left(\dfrac{p}{kT}\right) y_k$	(C.8)
Mixture density	ρ_{mix}	$\dfrac{pM}{RT}$	(C.9)

For chemical vapour deposition, where large thermal gradients are present, the thermal drift velocity is another useful quantity, and is given by:

$$\mathbf{v}^T = \frac{D_k^T}{\rho \omega_k} \nabla \ln T \qquad\qquad (\text{C.10})$$

Here, D_k^T is the thermal diffusion coefficient. For a chemical reaction j, and species k, the rate expression is determined by the stoichiometry:

$$R_k = M_k \sum_{j=1}^{N} \nu_{kj} r_j \qquad\qquad (\text{C.11})$$

Here, v_{kj} is the stoichiometric matrix and r_j is the reaction rate corresponding to reaction j, given by:

$$r_j = k_{f,j} \prod_{k=1}^{Q} c_k^{v_{kj}^f} - k_{r,j} \prod_{k=1}^{Q} c_k^{v_{kj}^r} \qquad \text{(C.12)}$$

Here, c_k is the molar concentration of species k, $k_{f,j}$ is the rate coefficient for the forward reaction, $k_{r,j}$ is the rate coefficient for the reverse reaction, and v_{kj}^f and v_{kj}^r are the corresponding stoichiometric matrices. The rate coefficients depend exponentially on the gas temperature through an Arrhenius expression, given by:

$$k_j = A_j T^{\beta_j} \exp\left(-\frac{E_j}{RT}\right) \qquad \text{(C.13)}$$

Here, A_j is the frequency factor for reaction j, β is the temperature exponent and E_j is the corresponding activation energy.

The species' thermodynamic properties are calculated using the polynomial equations summarised in Table C.2.

Table C.2: Summary of thermodynamic properties.

Property	Symbol	Polynomial/Expression	
Heat capacity	$C_{p,i}$	$R(a_1 + a_2 T + a_3 T^2 + a_4 T^3 + a_5 T^4)$	(C.14)
Molar enthalpy	h_i	$R\left(a_1 T + \dfrac{a_2}{2}T^2 + \dfrac{a_3}{3}T^3 + \dfrac{a_4}{4}T^4 + \dfrac{a_5}{5}T^5 + a_6\right)$	(C.15)
Molar entropy	s_i	$R\left(a_1 \ln T + a_2 \ln T + \dfrac{a_3}{2}T^2 + \dfrac{a_4}{3}T^3 + \dfrac{a_5}{4}T^4 + a_7\right)$	(C.16)
Enthalpy of reaction	H_j	$\displaystyle\sum_i \nu_{ij} h_i$	(C.17)
Entropy of reaction	S_j	$\displaystyle\sum_i \nu_{ij} s_i$	(C.18)
Heat source of reaction	Q_j	$-H_j r_j$	(C.19)
Total heat source	Q	$\displaystyle\sum_j Q_j$	(C.20)

The binary diffusion coefficients of species A in species B are calculated by:

$$D_{AB} = 2.66 \times 10^{-2} \frac{\sqrt{T^3(M_A + M_B)/(2 \times 10^3 M_A M_B)}}{p\sigma_A\sigma_B\Omega} \tag{C.21}$$

Here, σ is the characteristic length of the Lennard-Jones / Stockmayer potential, and Ω is the appropriate collision integral. Dynamic viscosity is determined using kinetic gas theory as:

$$\mu_i = 2.669 \times 10^{-6} \frac{\sqrt{T(M_i \times 10^3)}}{\sigma_i^2\Omega} \tag{C.22}$$

where μ_i is the dynamic viscosity of species i. The thermal conductivity, k_T, is determined from the Stiel-Thodos equation, given as:

$$k_T = \frac{\eta}{M}\left(1.15C_p + 0.88R\right) \tag{C.23}$$

Mixture properties are calculated using the following equations:

$$c_{p_{mix}} = \frac{\sum_i y_i C_{p,i}}{\sum_i y_i M_i} \tag{C.24}$$

$$k_{mix} = \frac{1}{2}\left[\sum_{i=1} y_i k_i + \left(\sum_{i=1} \frac{y_i}{k_i}\right)^{-1}\right] \tag{C.25}$$

$$\mu_{fluid} = \sum_{i=1} \frac{y_i \mu_i}{\sum_{j=1} y_j \phi_{ij}} \tag{C.26}$$

Here, $c_{p_{mix}}$ is the mass-based heat capacity and ϕ_{ij} is defined as:

$$\phi_{ij} = \frac{\left[1 + \left(\frac{\eta_i}{\eta_j}\right)^{0.5} \left(\frac{M_j}{M_i}\right)^{0.25}\right]^2}{\left[8\left(1 + \frac{M_i}{M_j}\right)\right]^{0.5}} \tag{C.27}$$

If a surface reaction is assumed with I surface reactions and K chemical species, then:

$$\sum_{k=1}^{K} v_{ki}^f c_k \leftrightarrow \sum_{k=1}^{K} v_{ki}^r c_k \tag{C.28}$$

Here, c_k is the concentration of the kth species. The molar production rate for each species is then given by:

$$\dot{s}_k = \sum_{i=1}^{I} v_{ki} q_i \tag{C.29}$$

where

$$v_{ki} = v_{ki}^r - v_{ki}^f \tag{C.30}$$

$$q_i = k_{f,i} \prod_{k=1}^{K} c_k^{v_{ki}^f} - k_{r,i} \prod_{k=1}^{K} c_k^{v_{ki}^r} \tag{C.31}$$

The forward rate constant for the surface reaction is given by:

$$k_{f,i} = \left(\frac{\gamma_i}{1 - \frac{\gamma_i}{2}} \right) \frac{1}{(\Gamma_{tot})^m} \sqrt{\frac{RT}{2\pi M}} \tag{C.32}$$

The sticking coefficient, γ_i, may be defined as a constant or temperature dependant via an Arrhenius expression. Additional information can be found in Ref. [164, 174].

3. Plasma Reactor Theory

Electron density and mean electron energy are computed by solving the drift-diffusion equations discussed earlier [158]. Convection of electrons due to fluid motion is neglected. The electron diffusivity, energy mobility and energy diffusivity are then calculated using:

$$D_e = \mu_e T_e \tag{C.33}$$

$$\mu_\varepsilon = \left(\frac{5}{3} \right) \mu_e \tag{C.34}$$

$$D_\varepsilon = \mu_\varepsilon T_e \tag{C.35}$$

The electron source and inelastic energy loss are then calculated using the equations described in the Electron Transport Theory section (section 1 of this Appendix). The rate coefficients are calculated using cross-section data and EEDF. The mass fractions of the

heavy species are then solved for by the equations described in the Heavy Species Transport Theory section (section 2 of this Appendix). The space charge density is computed based on specified plasma chemistry using Equation (C.36).

$$\rho = q\left(\sum_{k=1}^{N} Z_k n_k - n_e\right) \tag{C.36}$$